

# Onboard Trajectory Generation for the Unpowered Landing of Autonomous Reusable Launch Vehicles

by

André R. Girerd

B.S. Aerospace Engineering  
University of Virginia, 1997

Submitted to the Department of Aeronautics and Astronautics  
in partial fulfillment of the requirements for the degree of

Master of Science in Aeronautics and Astronautics

at the

MASSACHUSETTS INSTITUTE OF TECHNOLOGY

June 2001

© 2001 André R. Girerd. All Rights Reserved

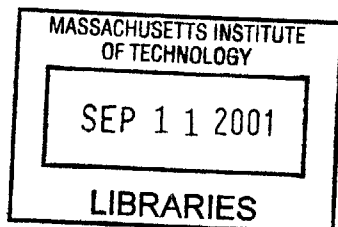
The author hereby grants to MIT permission to reproduce and to distribute publicly paper and electronic copies of this thesis document in whole or in part.

Author .....  
Department of Aeronautics and Astronautics  
May 11, 2001

Approved by .....  
Gregg Barton  
Next Generation Entry Guidance Principal Investigator  
The Charles Stark Draper Laboratory, Inc.  
Technical Supervisor

Certified by .....  
John J. Deyst  
Professor of Aeronautics and Astronautics  
Thesis Supervisor

Accepted by .....  
Wallace E. Vandervelde  
Professor of Aeronautics and Astronautics  
Chairman, Departmental Graduate Committee



**Aero**



# **Onboard Trajectory Generation for the Unpowered Landing of Autonomous Reusable Launch Vehicles**

By

André R. Girerd

Submitted to the Department of Aeronautics and Astronautics on  
May 11, 2001, in partial fulfillment of the requirements for the  
degree of Master of Science in Aeronautics and Astronautics

## **Abstract**

Onboard trajectory generation dispenses with the pre-defined trajectories used in Reusable Launch Vehicle (RLV) guidance since the early days of the Shuttle era. This shift, enabled by a new breed of algorithms harnessing modern computer power, offers improvements in performance, robustness, operational cost, and safety.

This thesis develops a set of algorithms providing onboard trajectory generation for low lift-over-drag gliding RLVs in subsonic flight below 40,000 ft. The NASA/Orbital Sciences X-34 is used as a representative model for which feasible trajectories are designed over a range of initial conditions without human intervention.

In addition to being autonomous, the guidance output of the onboard trajectory generator differs from current Shuttle-based approaches, providing a realistic “future history” in a propagated plan, rather than output commands reacting to perceived instantaneous vehicle needs. Hence, this approach serves an enabling role in a larger research effort to develop a next generation guidance system using an integrated control function.

To assess feasibility, the onboard trajectory generator is benchmarked against traditional X-34 guidance for a drop test scenario. The results match in basic form, with differences showcasing the autonomous algorithms’ preference for maximum robustness. The true strength of the onboard trajectory generator lies in its ability to handle off-nominal conditions. A series of test cases highlight the ability of the algorithms to effectively cope with anomalous initial drop conditions, reach the desired terminal states, and provide maximum late-trajectory robustness. Computation time is sufficiently brief to suggest a real-time application, after straightforward improvements are made.

Thesis Supervisor: John J. Deyst  
Title: Professor of Aeronautics and Astronautics

Technical Supervisor: Gregg H. Barton  
Title: Principal Member Technical Staff, C.S. Draper Laboratory, Inc.



## **Acknowledgments**

I would like to thank the Charles Stark Draper Laboratory for offering me the opportunity to pursue my graduate education at MIT with technical and financial support. I am extraordinarily appreciative of the time, advice, and patience given by my technical advisor, Gregg Barton, whose knowledge, vision, and demeanor have propelled the quality of his mentorship to an admirable level. I am also grateful for the assistance provided by my interim technical advisor, Dr. Steve Tragesser.

I would like to recognize the staff and professors in the MIT Aeronautics and Astronautics Department. Particular thanks go to my thesis advisor, Professor John Deyst for his support.

Utmost gratitudes I bestow upon my friends at MIT and Draper, who have exuded plentiful shimmerings of knowledge and paved my environs with worthy happenstance and goodly divertissement. Three cheers for my roommates dwelling in the hypogeal Harvard nerd cavern, the MITOC enthusiasts in their outdoor splendor, and my Sloan Crew buddies whose efforts enlivened the early morning. Chisholm and Pat were excellent guides for navigating the Draper environment, and I especially am appreciative of the time Chisholm spent divulging the nuances of his related research. Thanks I bestow upon all the other Draper fellows who made this voyage memorable: Andrew, Erik, George, Jeremy, John, Paul, and Raja.

Finally, I wish to state my sincere appreciation for the supportive role performed by my family. My parents and sister have offered me healthy succor, of both the encouraging and diversionary varietals. Such backing I highly cherish.

## Acknowledgement

May 11, 2001

This thesis was prepared at the Charles Stark Draper Laboratory, Inc. under Independent Research and Development #13033.

Publication of this thesis does not constitute approval by the Draper or the sponsoring agency of the findings or conclusions contained herein. It is published for the exchange and stimulation of ideas.



---

André R. Girerd

# Table of Contents

<b>1</b>	Introduction .....	23
1.1	Next Generation Entry Guidance and Control.....	23
1.2	Background.....	24
1.3	Thesis Objective.....	27
1.4	Thesis Overview .....	27
<b>2</b>	Vehicle Description .....	29
2.1	Overview.....	29
2.2	Mission Profile and Physical Description.....	30
2.3	Aerodynamic Properties.....	31
2.4	Reference Coordinate Frames.....	33
2.5	Nonlinear Equations of Motion .....	37
<b>3</b>	Entry Guidance Overview .....	41
3.1	Overview.....	41
3.2	Traditional Energy Management .....	41
3.2.1	Baseline Shuttle Approach.....	42
3.2.1.1	Shuttle Concept.....	42
3.2.1.2	Shuttle Entry Phases .....	43
3.2.2	X-34 Modifications .....	46
3.3	X-34 Guidance and Control Interaction.....	47
<b>4</b>	Methodology for Onboard Design.....	51
4.1	Overview.....	51
4.2	Challenges of Autonomous Algorithms.....	51
4.3	Fundamental Design Choices .....	52
4.3.1	Onboard Considerations.....	52
4.3.2	Integrated Guidance and Control Framework.....	54
4.3.3	General Algorithm Scope and Format Decisions.....	57
4.3.4	Optimization Issues.....	58
4.4	Design Heritage .....	59

<b>5</b>	<b>Onboard Trajectory Generation Technology Components .....</b>	<b>61</b>
5.1	Introduction and Overview .....	61
5.2	Two Point Boundary Value Problem.....	62
5.2.1	Rationale and Overview .....	62
5.2.2	Longitudinal Formulation .....	63
5.2.2.1	Longitudinal Basics .....	63
5.2.2.2	Compound vs. Non-Compound Curves.....	64
5.2.2.3	Longitudinal Geometry .....	68
5.2.3	Lateral Formulation.....	74
5.2.3.1	Lateral Basics.....	74
5.2.3.2	Shuttle vs. Next Generation .....	75
5.2.3.3	Detailed Lateral Geometry.....	77
5.3	Constrained Trajectory Propagation .....	81
5.3.1	Rationale and Overview .....	81
5.3.2	Change of States.....	82
5.3.3	Change of Independent Variable.....	84
5.3.4	Geometric Variables.....	85
5.3.4.1	Longitudinal Derivation.....	85
5.3.4.2	Lateral Derivation .....	86
5.3.5	Propagation Algorithm.....	88
5.4	Fast Tradespace Scanning.....	91
5.4.1	Rationale and Overview .....	91
5.4.2	Tradespace Generation.....	91
5.4.2.1	Longitudinal Tradespace Constraints .....	91
5.4.2.1.1	Geometric Limits .....	93
5.4.2.1.2	Max Dive and Max Glide Limits.....	95
5.4.2.1.3	NZ Limits.....	96
5.4.2.2	Lateral Tradespace Constraints.....	105
5.4.2.2.1	Geometric Limits .....	106
5.4.2.2.2	Acceleration Limits.....	106
5.4.3	Desirability Criterion.....	108



5.4.4	NZ Tradespace for Specific Gamma .....	109
5.5	Adaptive Center-of-Capability Reference .....	112
5.5.1	Rationale and Overview .....	112
5.5.2	Control Parameter Survey .....	112
5.5.2.1	NZ Control .....	113
5.5.2.2	Outer Glideslope Control .....	114
5.5.2.3	Speedbrake Control .....	117
5.5.3	Center of Capability .....	119
5.5.4	Adaptive Center of Capability Reference .....	120
5.6	Section 5.6 Optimized Trajectory Computation .....	125
<b>6</b>	<b>Onboard Trajectory Generation Component Integration.....</b>	<b>127</b>
6.1	Overview .....	127
6.2	Nature of Longitudinal/Lateral Coupling .....	127
6.3	Master Algorithm Data Flow .....	130
6.4	Significance of the Adaptive Reference in Program Output Context.....	134
<b>7</b>	<b>Results .....</b>	<b>137</b>
7.1	Overview .....	137
7.2	Comparison with Existing Guidance .....	137
7.3	Algorithm Performance for Off-Nominal Conditions .....	142
<b>8</b>	<b>Conclusions and Recommendations for Further Research.....</b>	<b>149</b>
8.1	Conclusions.....	149
8.2	Recommendations for Further Research.....	152
<b>Appendix A</b>	<b>Examples Highlighting Different AI Capability Levels.....</b>	<b>155</b>
<b>Appendix B</b>	<b>Method for Calculating Maximum <math>R_{AC}</math>.....</b>	<b>157</b>
<b>Appendix C</b>	<b>Example of Effect of Bank Angle on Maximum and Minimum <math>dq/dt</math>.....</b>	<b>159</b>
<b>Appendix D</b>	<b>Additional Onboard Results From DRM4 Drop Scenario .....</b>	<b>161</b>
<b>References</b>	<b>.....</b>	<b>167</b>



## List of Figures

<b>Figure 1.1:</b> Artificial Intelligence Gradations .....	26
<b>Figure 2.1:</b> X-34 Configuration [9].....	30
<b>Figure 2.2:</b> Trimmed L/D vs. Angle of Attack.....	32
<b>Figure 2.3:</b> Coefficient of Lift vs. Angle of Attack.....	32
<b>Figure 2.4:</b> Coefficient of Drag vs. Angle of Attack.....	33
<b>Figure 2.5:</b> Inertial, Horizon, and Body Reference Frames .....	34
<b>Figure 2.6:</b> Heading/Flight Path Rotation .....	35
<b>Figure 2.7:</b> Angle of Attack/Side Slip Rotation .....	36
<b>Figure 3.1:</b> Space Shuttle Guidance Concept.....	42
<b>Figure 3.2:</b> TAEM Subphases [9] .....	44
<b>Figure 3.3:</b> Flight Path Along the HAC [9] .....	45
<b>Figure 3.4:</b> X-34 Guidance Concept .....	47
<b>Figure 3.5:</b> Guidance and Control for Longitudinal Loop .....	48
<b>Figure 3.6:</b> Guidance and Control for Lateral Loop .....	48
<b>Figure 3.7:</b> Speedbrake Control .....	49
<b>Figure 4.1:</b> General Approaches to Onboard Trajectory Generation.....	53
<b>Figure 4.2:</b> Integrated Guidance and Control Concept .....	55
<b>Figure 4.3:</b> Effect of Decreasing $X_{ZERO}$ .....	60
<b>Figure 5.1:</b> Basic Longitudinal Geometry.....	63
<b>Figure 5.2:</b> Compound Curve Trajectories (3-4 Segments).....	65
<b>Figure 5.3:</b> Compound Curve Trajectory (5 Segments).....	66
<b>Figure 5.4:</b> Non-Compound Curve Trajectory.....	68
<b>Figure 5.5:</b> Flare Trajectory Particulars .....	69
<b>Figure 5.6:</b> Locus Line for Flare Case .....	70
<b>Figure 5.7:</b> Anti-Flare Particulars .....	71
<b>Figure 5.8:</b> Locus Line for Anti-Flare Case.....	72
<b>Figure 5.9:</b> Elements of the Lateral Framework .....	75
<b>Figure 5.10:</b> Incompatibility of Shuttle and Next-Generation Lateral Guidance.....	76
<b>Figure 5.11:</b> Lateral Geometry.....	78
<b>Figure 5.12:</b> Straight-in and Overhead HAC Positions.....	79

<b>Figure 5.13:</b> Center-Point Differencing Numerical Technique.....	88
<b>Figure 5.14:</b> Propagation Algorithm [11] .....	90
<b>Figure 5.15:</b> Longitudinal Tradespace .....	92
<b>Figure 5.16:</b> Geometric Limits for Anti-Flare Case.....	94
<b>Figure 5.17:</b> Geometric Limits for Flare Case .....	94
<b>Figure 5.18:</b> Immediate Arc Options .....	97
<b>Figure 5.19:</b> Locus of Circular Flare Centers for Immediate Arcs .....	98
<b>Figure 5.20:</b> $H_{\text{travel}}$ in Context .....	100
<b>Figure 5.21:</b> Geometric Arc Options vs. Outer Glideslope.....	102
<b>Figure 5.22:</b> Allowable NZ Region vs. Outer Glideslope.....	104
<b>Figure 5.23:</b> Lateral Tradespace.....	105
<b>Figure 5.24:</b> NZ Tradespace for Max Glide.....	110
<b>Figure 5.25:</b> NZ Tradespace for Max Dive.....	111
<b>Figure 5.26:</b> Geometric Effect of NZ Variations .....	113
<b>Figure 5.27:</b> Dynamic Pressure Effect of NZ Variations.....	114
<b>Figure 5.28:</b> Geometric Effect of Outer Glideslope Variations .....	115
<b>Figure 5.29:</b> Dynamic Pressure Effect of Outer Glideslope Variation .....	116
<b>Figure 5.30:</b> Detail of Dynamic Pressure Effect of Outer Glideslope Variations.....	116
<b>Figure 5.31:</b> Geometric Effect of Speedbrake Variations .....	117
<b>Figure 5.32:</b> Dynamic Pressure Effect of Speedbrake Variation .....	118
<b>Figure 5.33:</b> Center-of-Capability as Measure of Robustness .....	119
<b>Figure 5.34:</b> Adaptive C-o-c Reference (wings level) for Flare and Anti-Flare Cases..	122
<b>Figure 5.35:</b> Sensitivity of C-o-c to Constant Bank Angle .....	123
<b>Figure 5.36:</b> Effect on C-o-c Reference Due to Lateral Component .....	124
<b>Figure 5.37:</b> Lateral Geometry for Figure 5.36.....	124
<b>Figure 5.38:</b> Energy Matching Procedure .....	126
<b>Figure 6.1:</b> Scheme for Lateral and Longitudinal Tradespace Coupling .....	129
<b>Figure 6.2:</b> Simplified Master Algorithm Data Flow.....	130
<b>Figure 6.3:</b> Detailed Master Algorithm Data Flow .....	132
<b>Figure 6.4:</b> Comparative Impact of the Adaptive Reference on Trajectory Output.....	135
<b>Figure 7.1:</b> Comparison of Onboard and Traditional Guidance for DRM4 Drop .....	138

<b>Figure 7.2:</b> Program Output for DRM4 Drop Case.....	140
<b>Figure 7.3:</b> Three Dimensional Representation of DRM4 Drop Trajectory .....	141
<b>Figure 7.4:</b> Program output for Sample off-Nominal Case #1.....	143
<b>Figure 7.5:</b> Three Dimensional Representation of Sample Off-Nominal Case #1 .....	144
<b>Figure 7.6:</b> Program Output for Sample Off-Nominal Case #2.....	145
<b>Figure 7.7:</b> Three Dimensional Representation of Sample Off-Nominal Case #2 .....	145
<b>Figure 7.8:</b> Program Output for Sample Off-Nominal Case #3.....	146
<b>Figure 7.9:</b> Three Dimensional Representation of Sample Off-Nominal Case #3 .....	147
<b>Figure 7.10:</b> Recoverable Heading Angle Options for DRM4 Drop Zone .....	148
<b>Figure B.1:</b> Simplified Procedure to Calculate Lateral Geometric Limit .....	157
<b>Figure B.2:</b> Geometric Limit (Max $R_{AC}$ ) Result for Example Case.....	158
<b>Figure C.1:</b> Effect of Bank Angle on Maximum and Minimum $dq/dt$ .....	159
<b>Figure C.2:</b> Bank Angle Profile for Figure C.1 .....	160
<b>Figure C.3:</b> Lateral Geometry for Figure C.1 .....	160
<b>Figure D.1:</b> Gamma, Altitude Rate and Altitude vs. Downrange .....	161
<b>Figure D.2:</b> $Q_{bar}$ and $Dq_{bar}/dh$ vs Downrange .....	162
<b>Figure D.3:</b> Elevon and Alpha Positions vs Downrange.....	162
<b>Figure D.4:</b> Mach Number and Theta vs. Downrange .....	163
<b>Figure D.5:</b> $L/D$ , $C_D$ , and $C_L$ vs. Downrange.....	163
<b>Figure D.6:</b> Equivalent Airspeed and True Airspeed vs. Downrange.....	164
<b>Figure D.7:</b> $V_{dot}$ , $\Gamma_{dot}$ , and $\alpha_{dot}$ vs. Downrange.....	164
<b>Figure D.8:</b> $\theta_{dot}$ and $NZ$ vs. Downrange.....	165
<b>Figure D.9:</b> Altitude vs. Time, Vehicle Weight, and Vehicle CG .....	165
<b>Figure D.10:</b> Energy Over Weight and $Deow/dh$ vs. Downrange .....	166



## List of Tables

<b>Table 4.1:</b> Guidance States .....	55
<b>Table 4.2:</b> Trajectory Control Variables.....	56
<b>Table 5.1:</b> States and Conditions for Approach and Landing Profile .....	62
<b>Table 5.2:</b> Geometric Segments .....	64
<b>Table 5.3:</b> Defining Geometric Parameters.....	68
<b>Table 5.4:</b> Generalized Components of Equation. 5.59 .....	103
<b>Table 7.1:</b> Initial Conditions at Guidance Start for DRM4 Drop.....	137
<b>Table 7.2:</b> Delta Initial Conditions for Sample Off-Nominal Case #1.....	142
<b>Table 7.3:</b> Delta Initial Conditions for Sample Off-Nominal Case #2.....	144
<b>Table 7.4:</b> Delta Initial Conditions for Sample Off-Nominal Case #3.....	146
<b>Table A.1:</b> AI Capability Level Examples .....	155





## List of Symbols

$\vec{a}$ .....	acceleration vector
$a_{lat}$ .....	lateral acceleration resultant scalar
$C_D$ .....	aerodynamic drag coefficient
$C_L$ .....	aerodynamic lift coefficient
$d_1$ .....	distance of first straight lateral segment
$d_{AC}$ .....	distance of lateral segment along acquisition turn
$d_{HAC}$ .....	distance of lateral segment on HAC
$d_T$ .....	distance of straight lateral segment after HAC
$D$ .....	aerodynamic drag force
$g$ .....	gravitational acceleration
$h$ .....	vehicle altitude
$h_{circ}$ .....	vehicle altitude along circular flare
$h_{inner}$ .....	vehicle altitude along inner glideslope
$h_{outer}$ .....	vehicle altitude along outer glideslope
$H_{ALI}$ .....	altitude of ALI
$H_{CLOOP}$ .....	altitude of circular arc initiation
$H_{END}$ .....	altitude of arc termination
$HI$ .....	altitude of intercept of inner and outer glideslopes
$HK$ .....	altitude of the center of the circular arc
$H_{REF1}$ .....	initial altitude
$H_{shali}$ .....	altitude of inner glideslope intercept with the initial groundtrack
$H_{travel}$ .....	altitude difference between flare initiation and HI
$L$ .....	aerodynamic lift force
$L_c$ .....	locus line
$m$ .....	vehicle mass
$n_z$ .....	normal acceleration along negative body z-axis command
$NZ$ .....	normal acceleration along negative body z-axis
$P$ .....	body roll rate
$q$ .....	dynamic pressure (also $qbar$ )

$Q$ .....body pitch rate  
 $r_1$ .....HAC spiral constant coefficient  
 $r_2$ .....HAC spiral constant coefficient  
 $r_{AC}$ ..... acquisition turn radius  
 $r_{cir}$ ..... distance between acquisition turn end and HAC center  
 $r_f$ ..... final HAC turn radius  
 $r_{pred}$ ..... predicted ground track distance  
 $r_{tan}$ ..... $d_1$   
 $r_{turn}$ .....HAC turn radius  
 $R$ .....radius of curvature of circular arc, body yaw rate  
 $S$ ..... wing planform area  
 $T_{a \rightarrow b}$ .....transformation matrix from frame a to frame b  
 $V$ ..... inertial speed  
 $\vec{V}$  ..... inertial velocity vector  
 $V_H$ ..... horizontal velocity  
 $W$ ..... vehicle weight  
 $x$ ..... downrange position  
 $x_{AC\_END}$ .....downrange position of acquisition turn end  
 $x_{ALI}$ ..... downrange position of ALI  
 $x_{CIR}$ ..... downrange distance between acquisition turn end and HAC center  
 $x_{HAC}$ .....downrange position of HAC center  
 $x_{INIT}$ ..... initial downrange  
 $X$ .....groundtrack position (ALI-referenced)  
 $X_{ALI}$ ..... groundtrack position of ALI  
 $X_{initial}$ ..... initial groundtrack position  
 $X_{ZERO}$ .....outer glideslope intercept with landing altitude  
 $XI$ ..... groundtrack position of intercept of inner and outer glideslopes  
 $XK$ .....groundtrack distance between  $X_{ALI}$  and the center of the circular arc  
 $y$ ..... crossrange position  
 $y_{AC\_END}$ ..... crossrange position of acquisition turn end  
 $y_{CIR}$ ..... crossrange distance between acquisition turn end and HAC center

$y_{HAC}$ ..... crossrange position of HAC center  
 $y_{INIT}$ ..... initial crossrange  
 $y_{SGN}$ ..... HAC center sign indicator  
 $Y$ ..... aerodynamic side force  
 $\alpha$ ..... angle of attack  
 $\beta$ ..... sideslip angle  
 $\gamma$ ..... flight path angle  
 $\gamma_1$ ..... outer glideslope  
 $\gamma_2$ ..... inner glideslope  
 $\delta_a$ ..... aileron command  
 $\delta_e$ ..... elevon command  
 $\delta_{sb}$ ..... speedbrake command  
 $\theta$ ..... half turn angle of circular arc  
 $\mu$ ..... bank angle about the velocity vector  
 $\rho$ ..... atmospheric density  
 $\sigma$ ..... horizontal reference angle  
 $\Phi$ ..... roll angle  
 $\chi$ ..... heading angle  
 $\Psi_{AC}$ ..... acquisition turn angle  
 $\Psi_C$ ..... heading to center of HAC  
 $\Psi_{HA}$ ..... HAC turn angle  
 $\Psi_T$ ..... heading to HAC tangency



## List of Acronyms and Abbreviations

A/L.....	approach and landing
ALI.....	autoland interface
AI.....	artificial intelligence
ALIP.....	Autoland I-load Program
DRM4.....	design reference mission 4
DOF.....	degree of freedom
C-o-c.....	center of capability
Draper.....	Charles Stark Draper Laboratory
E/W.....	energy over weight
EI.....	entry interface
FADS.....	flush air data system
G&C.....	guidance and control
GPS.....	global positioning system
GRTL.....	gliding return to launch site
HAC.....	heading alignment cone
INS.....	inertial navigation system
IG&C.....	integrated guidance and control
L/D.....	lift over drag
LOX.....	liquid oxygen
LQR.....	linear quadratic regulator
Orbital.....	Orbital Sciences Corporation
POST.....	program to optimize simulated trajectories
RLV.....	reusable launch vehicle
TAEM.....	terminal area energy management
TPBVP.....	two point boundary value problem



# Chapter 1

## Introduction

### 1.1 Next Generation Entry Guidance and Control

The current re-entry guidance methods for winged gliding Reusable Launch Vehicles (RLVs) use technologies originally developed for the Space Shuttle that were restricted by the available computing power of the 1970's. These techniques, being implemented on modern experimental RLV's like the X-33, X-34, X-37, and X-40, carry several important limitations. They rely on prespecified trajectories, defined well before launch, which involve labor-intensive pre-flight design, confine the vehicle to tight flight corridors, and lack robustness for changing flight conditions. Abort contingencies are all pre-planned, utilizing "canned" responses of pre-loaded abort recovery trajectories, which effectively prevent full exploitation of a vehicle's recovery capacity. In addition, each flight requires a standing army of ground support, contributing to supererogatory operational expenditures.

Modern computer capabilities allow a new approach to RLV guidance. Onboard trajectory generation in real time eliminates dependency on pre-defined trajectories. This, in turn, lowers recurring operational costs by substituting a single technology development cost, trading the labor-intensive trajectory design process of each new flight for a one-time algorithm certification effort. The use of actual rather than pre-planned flight states increases flexibility and expands flight corridors. Furthermore, onboard algorithms generate up-to-date profiles for maximum robustness. In the case of an abort, an instantaneous assessment of vehicle flight conditions allows successful recovery trajectories to be produced for unanticipated, off-nominal cases.

The Charles Stark Draper Laboratory (Draper) has plans for a coordinated effort to develop a suite of technologies that introduce the next generation of entry guidance and control. The key components of this strategy are an autonomous abort planner, an onboard trajectory generator, and an integrated guidance and control (G&C) framework.

Understanding the relationship between these components provides a clearer context for each individual technology.

The autonomous abort planner assesses the vehicle state in an abort scenario, and scrutinizes the available energy vs. downrange for a variety of landing options. It suggests a set of runways that theoretically allows a successful recovery, but relies on a guidance system to define the detailed trajectory path.

The onboard trajectory generator creates guidance references, from the vehicle's current state to its desired terminal conditions, in real time and without human intervention. While the use of onboard trajectory generation is most dramatic in an abort scenario, where the initial conditions may be sufficiently anomalous so as to render any pre-defined reference trajectory irrelevant, it also functions for more benign scenarios, where it yields greater robustness, improved performance, and lower operational cost.

To fully capture the improvements of the autonomously generated trajectory, an integrated guidance and control (G&C) framework is needed. Current Shuttle-based techniques separate the G&C functions, disregarding the coupling of their mutual objectives. In this manner, the guidance and control do not always cooperate to achieve the desired trajectory, but react to each other instead. Any changes in vehicle characteristics, stemming from routine pre-flight configuration modifications, irregular shifts in center-of-gravity from excess fuel, or unexpected abort-related damage, require thorough redesign of the needed guidance and control interaction to prevent languorous or oscillatory vehicle response. An integrated guidance and control framework has the potential to overcome these difficulties, simplifying the G&C interaction, allowing real-time implementation, and improving performance over the standard method.

## **1.2 Background**

The ability of an RLV to automatically fly to a successful landing is not new. The Soviet shuttle Buran relied on an autopilot to land after its first orbital voyage in 1988. The U.S. Space Shuttle has had a pilotless entry capability from the beginning, but astronauts



typically prefer manual control when given the choice. Because of the demonstrated success of the Shuttle algorithm, most of the documented theoretical advances in gliding entry guidance since 1981 have incorporated only modest changes to the Shuttle baseline [1,2,3]. The current crop of experimental RLVs continue to use Shuttle-based guidance schemes that rely on pre-loaded reference trajectories.

The bulk of recent theoretical entry guidance improvements have addressed the high-mach, intense heat conditions of the high altitude phase of atmospheric entry. The X-37 project will explore entry risks by pushing the edge of the flight envelope in this region [4]. Ping Lu hints that the reformulation of a reference drag profile, as a function of energy instead of Earth-relative velocity, would be attractive for onboard determination [5]. However, no program official or researcher has made a public claim to be specifically pursuing an onboard trajectory generation capability. In addition, the recent incremental improvements to entry guidance do not extend to the lower altitude regions of flight, where heating considerations are less important, but where energy management issues remain highly critical. This flight regime is called Terminal Area Energy Management (TAEM), and is characterized as gliding-type flight starting at a velocity of 2500 ft/s for the Shuttle [6]. TAEM gives way to the approach and landing (A/L) phase at 10,000 ft altitude.

A Boeing guidance and control team claimed "...in August 1998...the X-40A demonstrated the first ever 'Low Lift over Drag' autonomous landing using differential GPS." [3] It is essential to properly contextualize the usage of the term "autonomous". Figure 1.1 shows the three standard gradations of capability as defined by the Artificial Intelligence (AI) community. The most basic level is "automatic", and is defined as the ability to perform a function without human intervention. The Shuttle's pilotless capability, although never used during landing, falls into the automatic category. The next level is "autonomous", and is defined as the ability to react and adapt to unplanned but reasonably expected conditions. For example, a human pilot acts autonomously when following a procedure learned in training to resolve a sudden anomaly. The last level is "intelligent", and is defined as the ability to handle completely unexpected conditions in

unforeseen ways. This requires a degree of ingenuity, and represents the holy grail of the AI community. Appendix A provides additional examples of the distinction between capability types. To date, entry guidance systems are most properly characterized as automatic, relying on canned references that provide a “script” for vehicle G&C. The strict adoption of the AI definitions by the entry guidance community remains relatively lax, however, and confusion between “automatic” and “autonomous” is commonplace, with the X-40A team’s claim of an autonomous landing being one example. The introduction of onboard trajectory generation would allow a truly autonomous capability.

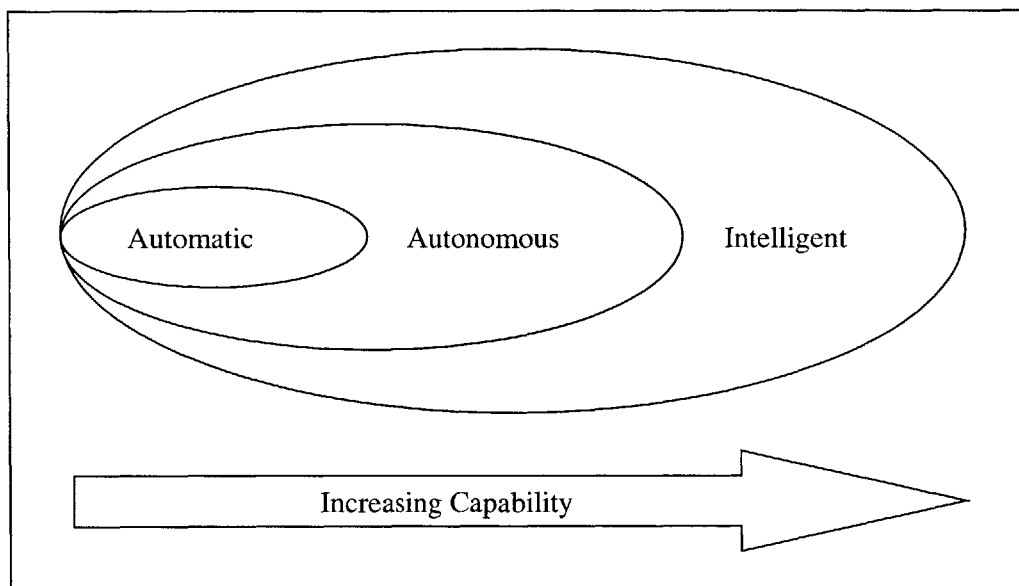


**Figure 1.1:** Artificial Intelligence Gradations

Research into next generation entry guidance started in 1996 by Jeffrey D. Barchers in a MIT Masters thesis [7]. Examining abort scenarios for the X-34 vehicle, he developed a model based framework for entry guidance, which could be used prior to the TAEM interface. Christina T. Chomel initiated research into integrated guidance and control in her 1998 MIT Masters thesis, using Linear Quadratic Regulator (LQR) multivariable control methods to address longitudinal dynamics of the X-34 [8]. Chisholm C. Tracy improved upon her work in his 1999 MIT Masters thesis to incorporate lateral dynamics, but could not fully demonstrate the integrated G&C concept because next-generation guidance references (from an onboard generator) were unavailable at that time [9]. Also in 1999, Steve Tragesser of Draper developed an autonomous intact abort system for the

X-34, but had to use existing, less-than-ideal guidance software to implement it [10]. Gregg Barton, also of Draper, created the Auto Landing I-Load Program (ALIP) for rapid pre-mission design of autoland trajectories for the X-34 [11]. His techniques showed enough promise to serve as a starting point for onboard trajectory generation in the TAEM flight regime.

### **1.3 Thesis Objective**

This thesis seeks to introduce a set of techniques that allow onboard trajectory generation for low lift over drag gliding RLVs in the subsonic flight regime below an altitude of 40,000 ft, using the X-34 as a representative vehicle model. The coupling of longitudinal and lateral dynamics, while imposing constraints, will result in guidance references that are flyable and representative of actual vehicle physics. An analysis of the trajectory design problem will lead to a comprehensive solution methodology conducive to real time implementation. Furthermore, the guidance outputs will show compatibility with an advanced integrated guidance and control framework. The thesis intends to establish a starting point from which further development of its original concepts may proceed.

### **1.4 Thesis Overview**

This thesis demonstrates that autonomous algorithms can successfully design trajectories for RLVs. Chapter 2 provides a brief description of the X-34, the test vehicle used for demonstrating onboard trajectory technologies. This chapter also derives the equations of motion and addresses any mathematical assumptions crucial for understanding the remainder of the text. Chapter 3 highlights traditional entry guidance to serve as a point of departure for the subsequent development of the next generation guidance. Chapter 4 discusses the methodology of the design process, addressing the fundamental challenges of autonomous algorithms, reasons for the general approach chosen, and inheritance from previous efforts. Chapter 5 covers the various enabling guidance techniques in detail, showing their utility and development rationale. Chapter 6 builds on the material of Chapter 5 by describing the system-level interactions between technology components. Chapter 7 assesses the performance of the guidance output from the autonomous

algorithms through a comparison with a standard X-34 reference profile and an inquiry into a series of off-nominal cases. Finally, Chapter 8 offers conclusions and suggests areas for further research.

## Chapter 2

### Vehicle Description

#### 2.1 Overview

NASA's X-34 project intends to demonstrate and evaluate technologies leading to the next generation of low cost reusable launch vehicles. In addition to testing a host of experimental physical components, such as inexpensive propulsion, improved thermal protection systems, and composite airframe structures requiring minimal inspection, the X-34 program plans to exhibit key operational capabilities. These include quick flight turnaround, automatic landing, and safe abort techniques. Since next generation RLV guidance algorithms can theoretically enhance these operational capabilities, a series of flight demonstrations are desirable to showcase the anticipated cost and performance improvements. A successful showcase should transform the status of next generation algorithms from intriguing premise to applied practice, overcoming latent technical traditionalism and clearing the way for broad industry acceptance. The X-34, being designed for such flight experiments, represents an ideal testbed on which to apply the new algorithms.

The choice of the X-34 is further justified by the large amount of relevant technical experience the Draper Laboratory has accumulated with this vehicle. In a partnership with the Orbital Sciences Corporation (Orbital), Draper has developed the entry and autoland guidance algorithms to support the upcoming flight tests. The X-34 project operates a detailed 6 degree of freedom (6-DOF) vehicle simulator, called STEP, to support algorithm and software verification for guidance, navigation, and control. Using valid data from the X-34 project supports the realism of this thesis research and allows comparative evaluation against traditional guidance techniques.

This chapter seeks to introduce the X-34 and the relevant physics that govern its behavior. A mission profile and physical description aims to elucidate the vehicle and its intended use. Next, a discussion of its aerodynamic properties provides perspective on

the difficulty of the guidance problem. Then, a listing of vehicle coordinate frames provides a mathematical reference structure for the relevant physics, setting the stage for a derivation of the nonlinear equations of motion.

## 2.2 Mission Profile and Physical Description

The suborbital X-34 vehicle, being built by Orbital, will be air-launched from the belly of an L-1011 carrier airplane up to 500 miles downrange from the intended landing site. After igniting its liquid-fueled rocket engine, the unpiloted craft will reach a maximum speed of Mach 8 and soar to an altitude of 250,000 ft. It will then perform an automated approach and landing, culminating in the deployment of a drag chute during its runway rollout. A regimen of at least 27 planned flights will allow subsequent analysis of achieved operations efficiency. Unpowered drop trials early in the testing phase will increase confidence in the system before later exploration of the high performance extremes of the vehicle flight envelope.

The vehicle measures 58.3 feet in length with a wingspan of 27.7 feet. It has a planform area of 357.5 ft<sup>2</sup>, a landing mass of roughly 18,000 lbs, and a capacity for 30,000 lbs of LOX/RP-1 fuel [13]. The Fastrac engine is designed to provide 60,000 lbs of thrust. Figure 2.1 shows the general layout of the X-34.

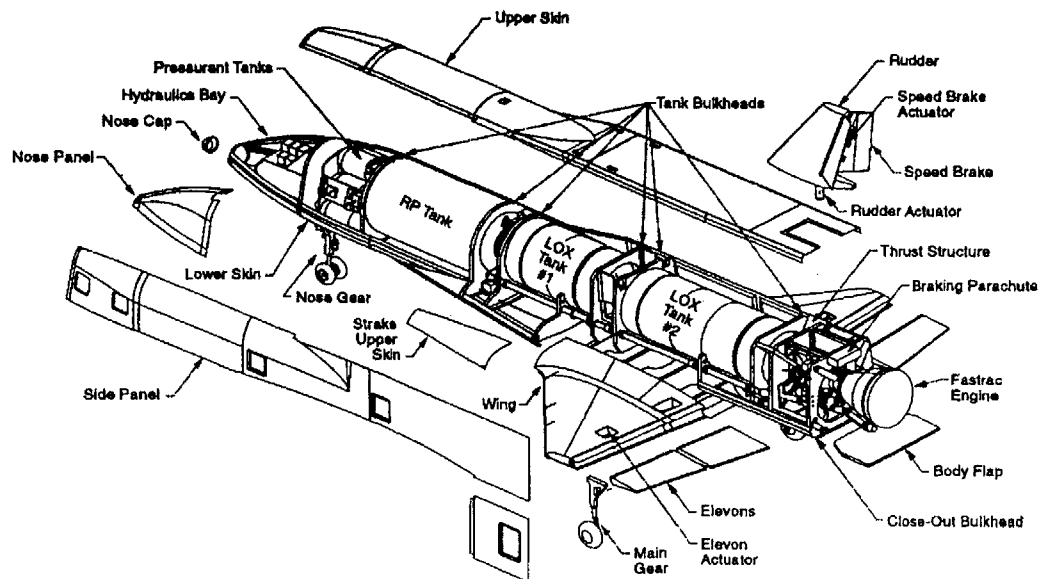


Figure 2.1: X-34 Configuration [9]

The X-34 uses four aerodynamic control surfaces: a rudder, a speedbrake, elevons, and a body flap. The speedbrake ranges from  $0^\circ$  (fully closed) to  $103^\circ$  (fully open), and the elevons deflect from  $-34.2^\circ$  to  $+15.8^\circ$ . The body flap is not used as part of the control system, functioning only as an open-loop trim device with different pre-programmed settings in successive stages of entry.

## 2.3 Aerodynamic Properties

The impact of the X-34's aerodynamic properties on its guidance systems and flight profile warrants some explanation. Unlike airplanes, whose engines provide a net positive energy source allowing a wide range of acceptable flight conditions, unpowered gliding entry vehicles must carefully manage an ever-decreasing amount of available total energy. Low Lift-over-Drag (L/D) RLVs like the Space Shuttle and X-34 face particularly stringent requirements on their flight profiles, having a more limited landing footprint and less margin for trajectory error than higher L/D vehicles. The low L/D impedes efficient gliding performance, and causes runway approaches with high speeds and relatively steep glideslope angles. Such vehicles must fly trajectories that retain sufficient energy to reach the targeted landing point, while also transitioning to suitable horizontal landing conditions by decreasing ground relative velocity and arresting the high sink rate in the final approach to the runway threshold.

Gliding vehicles can control the L/D ratio by flying at different angles of attack. Figure 2.2 shows the trimmed X-34 L/D curves for two different mach numbers using a constant speedbrake position of  $55^\circ$ . In the segment of increasing L/D with an angle of attack less than five degrees, the lift, shown in Figure 2.3, increases linearly while the drag, shown in Figure 2.4, is relatively flat. Beyond five degrees, however, the drag increases dramatically, while the lift remains linear. The resulting L/D curve soon peaks and starts decreasing, dividing the vehicle's aero capability into a front and back side. Keeping the vehicle in the front side of the curve, which is near-linear, is important for controllability.

Note that varying the speedbrake setting to increase or decrease drag will change the L/D ratio and the size of the operating front side region.

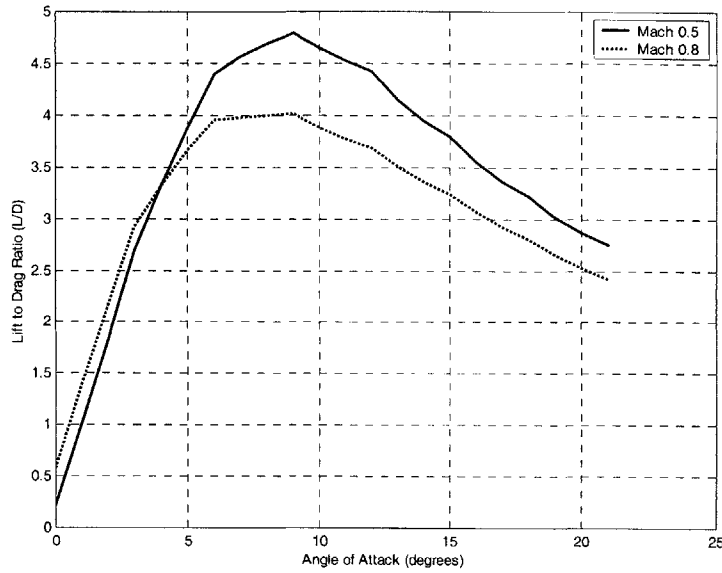


**Figure 2.2:** Trimmed L/D vs. Angle of Attack

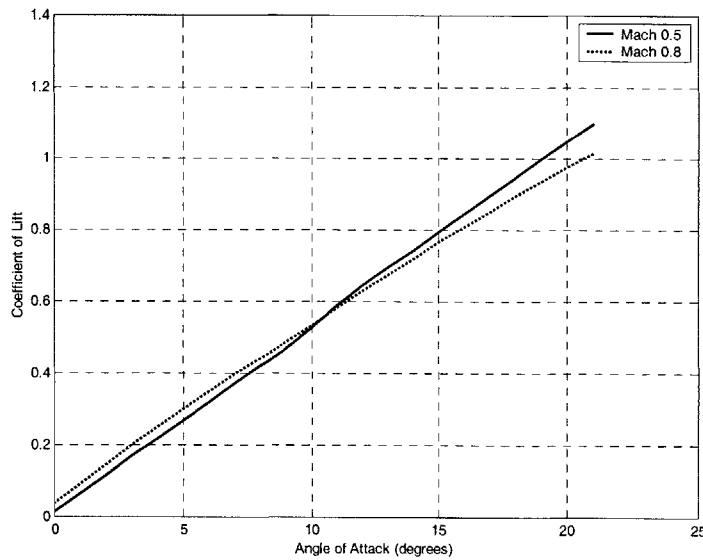


**Figure 2.3:** Coefficient of Lift vs. Angle of Attack



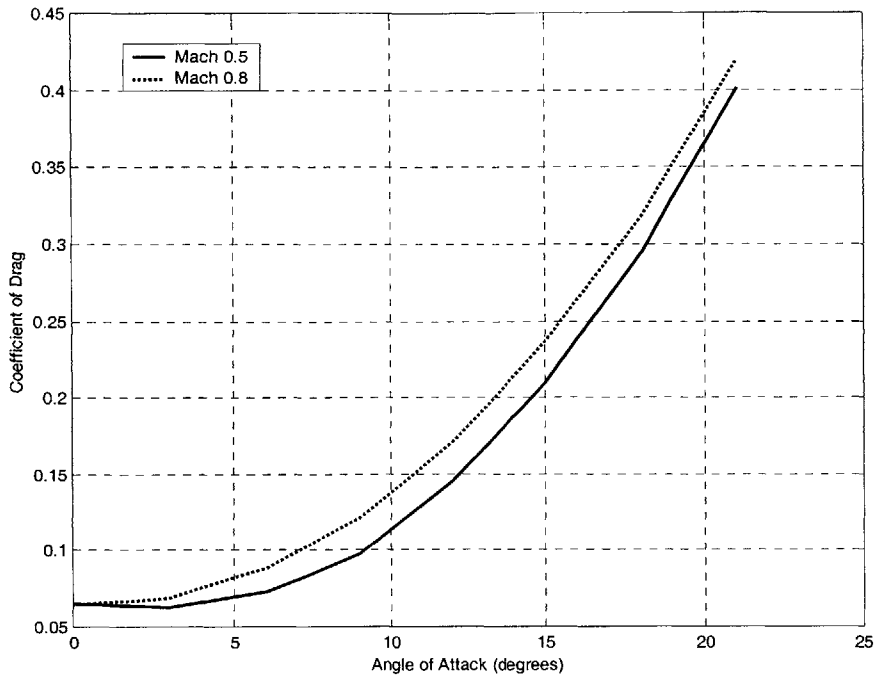


**Figure 2.4:** Coefficient of Drag vs. Angle of Attack

## 2.4 Reference Coordinate Frames

The following reference frames are relevant to the motion of an atmospheric vehicle as considered in this thesis.

**Inertial Reference Frame**  $(\hat{i}_i, \hat{j}_i, \hat{k}_i)$ : A coordinate frame fixed on the earth's surface can be assumed approximately inertial for low altitude atmospheric flight. The origin of the coordinate system is fixed at the initiation of the runway, as depicted in Figure 2.5.

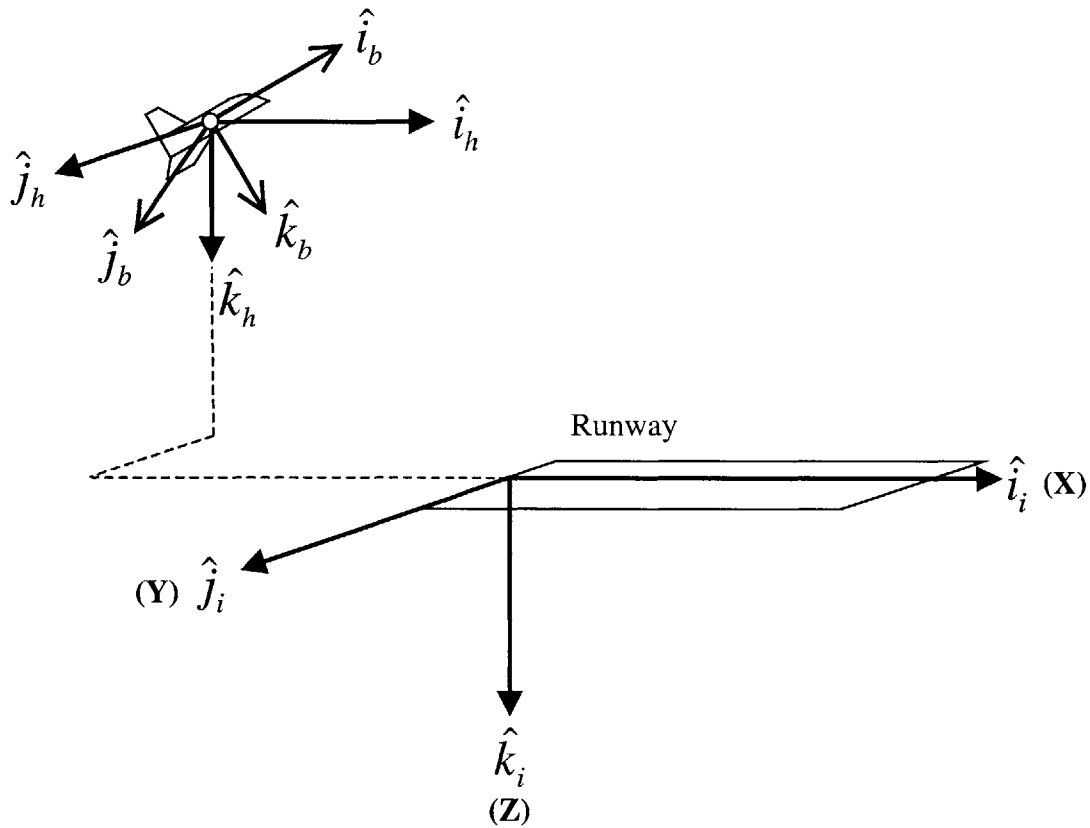


**Figure 2.5:** Inertial, Horizon, and Body Reference Frames

**Local Horizon Reference Frame**  $(\hat{i}_h, \hat{j}_h, \hat{k}_h)$ : The vehicle center of gravity serves as the origin of this frame with axes parallel to the inertial reference frame shown in Figure 2.5.

**Body Reference Frame**  $(\hat{i}_b, \hat{j}_b, \hat{k}_b)$ : The body reference frame is fixed at the vehicle center of gravity with the  $\hat{i}_b$  axis pointing out the nose, the  $\hat{j}_b$  axis pointing out the right wing, and the  $\hat{k}_b$  axis pointing in the vehicle's ventral direction. Figure 2.5 illustrates this.

**Velocity Reference Frame**  $(\hat{i}_v, \hat{j}_v, \hat{k}_v)$ : Fixed at the vehicle center of gravity, the  $\hat{i}_v$  axis points in the direction of the velocity vector. The  $\hat{j}_v$  axis is coincident with the cross product of the gravity vector ( $\hat{k}_h$ ) and  $\hat{i}_v$ .

**Stability Reference Frame** ( $\hat{i}_s, \hat{j}_s, \hat{k}_s$ ): With the origin at the vehicle center of gravity, the  $\hat{i}_s$  axis points along the projection of the velocity vector onto the body  $\hat{i}_b - \hat{k}_b$  plane. The  $\hat{j}_s$  axis follows the body  $\hat{j}_b$  axis along the right wing, with the  $\hat{k}_s$  axis completing a right-handed coordinate system.

**Wind Reference Frame** ( $\hat{i}_w, \hat{j}_w, \hat{k}_w$ ): With the origin at the vehicle center of gravity, the  $\hat{i}_w$  axis points in the direction of the velocity vector. The  $\hat{j}_w$  and  $\hat{k}_w$  axes are rotated about the velocity vector through the bank angle  $\mu$ .

**Rotation between Frames** ( $\chi, \gamma, \alpha, \beta, \mu$ ):

**Heading/Flight Path Rotation:**

An Euler angle rotation of  $\chi$  about the local horizon  $\hat{k}_h$  axis followed by  $\gamma$  about the local horizon  $\hat{j}_h$  axis defines the orientation of the velocity frame with respect to the local horizon frame. Figure 2.6 illustrates this. The angles  $\chi$  and  $\gamma$  are defined as the heading and flight path, respectively.

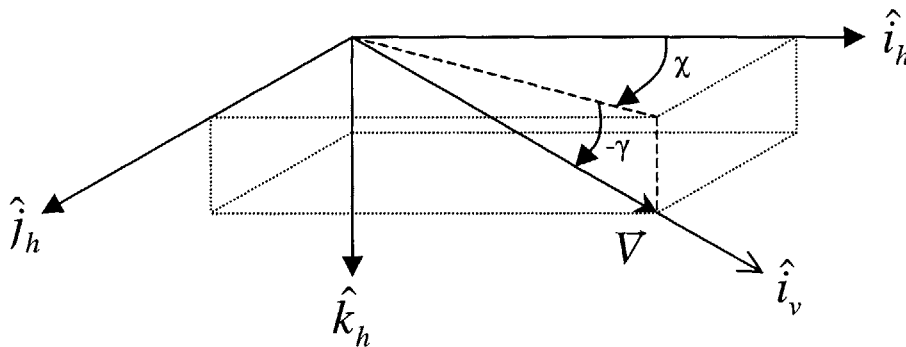


**Figure 2.6:** Heading/Flight Path Rotation

The transformation matrix between the local horizon and velocity frames is given by Equation 2.1.

$$T_{h \rightarrow v} = \begin{bmatrix} \cos \gamma \cos \chi & \cos \gamma \sin \chi & -\sin \gamma \\ -\sin \chi & \cos \chi & 0 \\ \sin \gamma \cos \chi & \sin \gamma \sin \chi & \cos \gamma \end{bmatrix} \quad (2.1)$$

### Angle of Attack/Side Slip Rotation:

An Euler angle rotation of  $\alpha$  about the body  $\hat{j}_b$  axis and  $\beta$  about the body  $\hat{k}_b$  axis defines the orientation of the inertial velocity vector,  $\hat{i}_v$ , and  $\hat{i}_w$  axes with respect to the body frame. Figure 2.7 illustrates this. The angle of attack and the sideslip angle are represented by  $\alpha$  and  $\beta$ , respectively. For the purposes of this thesis,  $\beta$  is assumed to be zero.

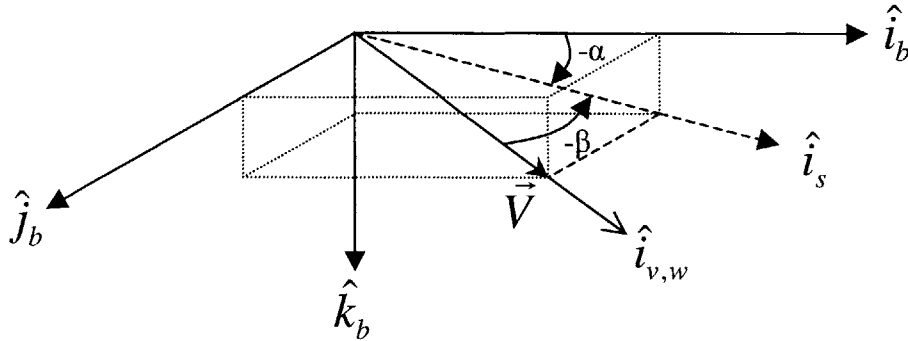


**Figure 2.7:** Angle of Attack/Side Slip Rotation

The transformation matrix between the body and wind frames is given by Equation 2.2.

$$T_{b \rightarrow w} = \begin{bmatrix} \cos \alpha \cos \beta & \sin \beta & \sin \alpha \cos \beta \\ -\cos \alpha \sin \beta & \cos \beta & -\sin \alpha \sin \beta \\ -\sin \alpha & 0 & \cos \alpha \end{bmatrix} \quad (2.2)$$

### Bank Angle Rotation:

The transformation matrix between the velocity and wind frames is described by Equation 2.3.

$$T_{v \rightarrow w} = \begin{bmatrix} 1 & 0 & 0 \\ 0 & \cos \mu & \sin \mu \\ 0 & -\sin \mu & \cos \mu \end{bmatrix} \quad (2.3)$$

## 2.5 Nonlinear Equations of Motion

Familiarity with the equations of motion is essential for a thorough understanding of the trajectory propagation technique used in this thesis research. Importantly, the desire for precision mandated the preservation of nonlinearities in the equations of motion. The onboard trajectory generator requires three translational equations. The additional three rotational equations needed in a 6-DOF system are not utilized by the trajectory propagator and will therefore be omitted from the following discussion.

The derivation begins by describing the position of the vehicle center of gravity with respect to the inertial frame as

$$\vec{r} = x\hat{i}_i + y\hat{j}_i + z\hat{k}_i \quad (2.4)$$

given the assumptions of a non-rotating, flat earth. Since  $T_{i \rightarrow h} = [I]$ , the position vector with respect to the local horizon frame is simply

$$\vec{r} = x\hat{i}_h + y\hat{j}_h + z\hat{k}_h \quad (2.5)$$

The inertial velocity vector  $\vec{V}$  is the time derivative of the position vector when coordinatized in the local horizon frame and is given by

$$\vec{V} = \frac{d}{dt} \vec{r} = \dot{x}\hat{i}_h + \dot{y}\hat{j}_h + \dot{z}\hat{k}_h \quad (2.6)$$

The inertial velocity vector  $\vec{V}$  can also be written as

$$\vec{V} = T_{v \rightarrow h} \begin{bmatrix} V \\ 0 \\ 0 \end{bmatrix}_v = V \cos \gamma \cos \chi \hat{i}_h + V \cos \gamma \sin \chi \hat{j}_h - V \sin \gamma \hat{k}_h \quad (2.7)$$

Equating components leads to

$$\dot{x} = V \cos \gamma \cos \chi \quad (2.8)$$

$$\dot{y} = V \cos \gamma \sin \chi \quad (2.9)$$

$$\dot{h} = -\dot{z} = V \sin \gamma \quad (2.10)$$

Since no thrust exists in gliding flight, the forces acting on the vehicle are

$$\sum \vec{F} = \vec{F}_{Aero} + \vec{F}_{Gravity} = m\vec{a} \quad (2.11)$$

The acceleration vector is given by

$$\vec{a} = \frac{d}{dt} \vec{V} = \frac{d}{dt} (V \hat{i}_v) = \dot{V} \hat{i}_v + V \frac{d}{dt} (\hat{i}_v) \quad (2.12)$$

Using the  $T_{h \rightarrow v}$  transformation matrix,  $\hat{i}_v$  can be defined in terms of the local horizon frame

$$\hat{i}_v = \cos \gamma \cos \chi \hat{i}_h + \cos \gamma \sin \chi \hat{j}_h - \sin \gamma \hat{k}_h \quad (2.13)$$

Taking its time derivative and simplifying yields

$$\dot{\hat{i}}_v = \dot{\chi} \cos \gamma \hat{j}_h - \dot{\gamma} \hat{k}_h \quad (2.14)$$

So the acceleration vector can be rewritten as

$$\vec{a} = \dot{V} \hat{i}_v + V \dot{\chi} \cos \gamma \hat{j}_h - V \dot{\gamma} \hat{k}_h \quad (2.15)$$

The aerodynamic forces of Lift ( $L$ ), Drag ( $D$ ), and Side Force ( $Y$ ) are expressed in the wind frame as

$$\vec{F}_{Aero} = -D \hat{i}_w - Y \hat{j}_w - L \hat{k}_w \quad (2.16)$$

Using the  $T_{v \rightarrow w}$  matrix, the aero forces can be expressed in the velocity frame as

$$\vec{F}_{Aero} = -D \hat{i}_v + (-Y \cos \mu + L \sin \mu) \hat{j}_v - (Y \sin \mu + L \cos \mu) \hat{k}_v \quad (2.17)$$

Since the force due to gravity in the velocity frame is

$$\vec{F}_{Gravity} = -mg \sin \gamma \hat{i}_v + mg \cos \gamma \hat{k}_v \quad (2.18)$$

the total force summation becomes

$$\sum \vec{F} = (-mg \sin \gamma - D) \hat{i}_v + (-Y \cos \mu + L \sin \mu) \hat{j}_v - (Y \sin \mu + L \cos \mu - mg \cos \gamma) \hat{k}_v \quad (2.19)$$

Solving equations 2.15 and 2.19 for  $\dot{V}$ ,  $\dot{\gamma}$ , and  $\dot{\chi}$  yields

$$\dot{V} = \frac{-D}{m} - g \sin \gamma \quad (2.20)$$

$$\dot{\gamma} = \frac{1}{V} \left( \frac{Y \sin \mu}{m} + \frac{L \cos \mu}{m} - g \cos \gamma \right) \quad (2.21)$$

$$\dot{\chi} = \frac{-Y \cos \mu + L \sin \mu}{mV \cos \gamma} \quad (2.22)$$

Since the side force Y will be considered negligible for this thesis, the equations simplify to

$$\dot{V} = \frac{-D}{m} - g \sin \gamma \quad (2.23)$$

$$\dot{\gamma} = \frac{1}{V} \left( \frac{L \cos \mu}{m} - g \cos \gamma \right) \quad (2.24)$$

$$\dot{\chi} = \frac{L \sin \mu}{mV \cos \gamma} \quad (2.25)$$

The drag and lift forces can be expressed as functions of the dynamic pressure q, vehicle planform area S, and dimensionless coefficients of drag  $C_D$ , and lift  $C_L$ .

$$D = qSC_D \quad (2.26)$$

$$L = qSC_L \quad (2.27)$$

The dynamic pressure can be written as a function of atmospheric density  $\rho$ , and air relative velocity V.

$$q = \frac{1}{2} \rho V^2 \quad (2.28)$$





## Chapter 3

### Entry Guidance Overview

#### 3.1 Overview

The objective of entry guidance is to direct a returning space vehicle to a safe landing without violating various constraints such as thermal, maximum dynamic pressure, or vehicle acceleration loading. For low L/D gliding vehicles (X-33, X-34, X-37) targeting a runway landing, the Space Shuttle guidance scheme serves as the traditional technique and point of departure.

Before proceeding further, it is necessary to establish a clear definition of guidance, in order to distinguish it from the concept of control. In the traditional arrangement, guidance handles trajectory and energy control. On the other hand, control (flight control) refers to actuator control based on steering inputs from guidance. An explanation of the concept of *integrated* guidance and control is deferred to Chapter 4.

This chapter seeks to provide an overview of entry guidance, and is divided into two conceptual groupings. The first covers traditional energy management, introducing the Space Shuttle baseline and noting the few modifications specific to the currently-implemented Orbital/Draper X-34 scheme. The second part provides a brief description of the interaction between the X-34's separate guidance and control functions.

#### 3.2 Traditional Energy Management

The current standard methods for the entry energy management of low L/D gliding vehicles were introduced during the development of the Space Shuttle, and have demonstrated themselves as impressively competent over nearly twenty years of service. The X-34 program elected to use the Shuttle technology because the proven techniques were easily transferable to a vehicle of similar aerodynamic configuration, and

developmental time, risk, and cost could be minimized. A few modifications specific to the mission profile of the X-34 were necessary, of course, and are described herein.

### 3.2.1 Baseline Shuttle Approach

#### 3.2.1.1 Shuttle Concept

Figure 3.1 illustrates the basic relationship between the various components of the Space Shuttle entry concept. A nominal trajectory and a series of contingency abort trajectories are designed off-board well before launch, and representative “reference profiles” are entered into the onboard guidance computers as a series of I-loads. During entry, the onboard guidance generates commands that attempt to match the actual vehicle states with the reference states. These guidance commands, typically speedbrake position, ( $\delta_{sb}$ ), roll, ( $\Phi$ ), and acceleration along the vehicle’s negative body Z axis, ( $n_z$ ), are fed to an onboard control system that produces a set of deflection commands for the control surface actuators.

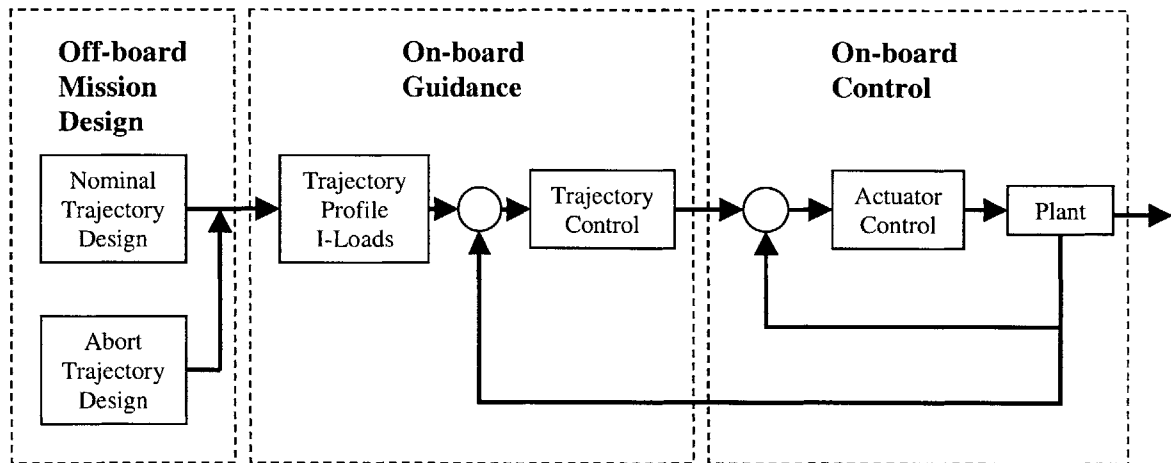


**Figure 3.1:** Space Shuttle Guidance Concept

The “reference profile” refers to a set of vehicle states or control histories arranged with respect to a monotonically changing variable such as time, velocity, or downrange. These profiles are loaded before launch, and represent the efforts of engineers to discover, through iterative design and optimization techniques, a suitable guide for an

entry vehicle's journey to its target. Although designed with nominal conditions in mind, the reference profiles can be quite robust to dispersions. However, sufficiently large revisions to the vehicle's aerodynamic characteristics, changing vehicle configurations, or alterations in expected initial flight conditions will require a complete reexamination and redesign of a reference profile.

### 3.2.1.2 Shuttle Entry Phases

Shuttle entry guidance is divided into three distinct phases: Entry, Terminal Area Energy Management (TAEM), and Approach and Landing (A/L). The different guidance requirements placed upon the vehicle during the three phases are considered sufficiently incompatible as to render a single overarching guidance phase infeasible. This separation stems not from current limitations in guidance technology, but rather from the changing nature of the fundamental flight dynamics over very large altitude ranges.

The first guidance phase, known as Entry, begins at the Entry Interface (EI), at 400,000 ft altitude and a typical downrange of 4300 nautical miles from the runway [6]. High energy, velocity, and heating loads characterize this aerobraking environment. Velocity (thus kinetic energy) is controlled as a function of range-to-go through the use of aerodynamic drag. Loaded reference profiles serve as a guide for the drag modulation. At first, travelling through the rarified upper atmosphere, the Shuttle's Reaction Control System (RCS) maintains vehicle attitude control. As dynamic pressure increases sufficiently, aerodynamic control surfaces begin to share the attitude control function. The regime of aerosurface/RCS blending eventually gives way to complete aerosurface control when the dynamic pressure exceeds 40 psf [6]. At mach 2.5 and about 85,000 ft altitude, the Entry phase ends and the TAEM phase begins.

The second guidance phase, the TAEM phase, uses the vehicle's gliding flight capability to control energy to the runway. The vehicle energy state, represented as Energy over Weight (E/W) is captured by its altitude (related to potential energy) and its dynamic pressure (related to kinetic energy). Unlike the entry phase, which uses a drag profile, the

TAEM phase uses profiles of altitude and dynamic pressure as functions of range-to-go. During its development, engineers decided to split the longitudinal and lateral channels, considering a full integration too complex [14]. Therefore, alpha and bank angle control the vertical and lateral channels, respectively.

There are two components to range, downrange and crossrange. A robust geometric method reduces these to a single ground track range, representing the crucial monotonic parameter upon which the altitude and dynamic pressure profiles are based. To this end, TAEM is split into four distinct subphases that correspond to four well-defined ground track segments. In order of progression, they are the S-turn, acquisition, heading alignment, and prefinal subphases, as illustrated in Figure 3.2.

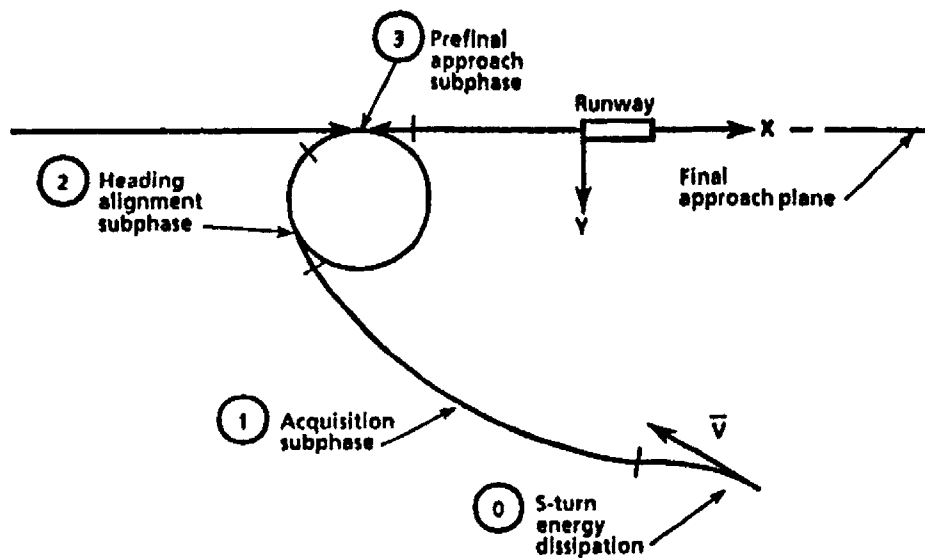


Figure 3.2: TAEM Subphases [9]

The S-turn subphase only occurs if the vehicle's energy state is too high to allow it to reach its targeted condition. By commanding a veer away from the desired heading at the maximum bank angle limit, an S-turn dissipates energy by increasing the ground track distance. No S-turn is commanded when the vehicle remains within its nominal E/W corridor.

The acquisition subphase changes the vehicle's heading to allow a smooth interception with the Heading Alignment Cone (HAC). It commands a constant bank angle that results in an approximately circular turn segment. The inaccuracies of this method for the purpose of ground track estimation are discussed in Chapter 5. After the circular segment produces the desired heading tangent to the HAC surface, a straight segment defines the path to the actual HAC intercept.

The heading alignment subphase transitions the vehicle's velocity vector to be coincident with the runway x-axis, thus zeroing any crossrange position displacements and off-axis heading angles. The flight path, shown in Figure 3.3, follows the surface of the HAC, descending in altitude while decreasing in turn radius. The resulting groundtrack is a spiral. Guidance keeps the vehicle on the HAC surface using radial position and rate errors to generate a bank angle command.

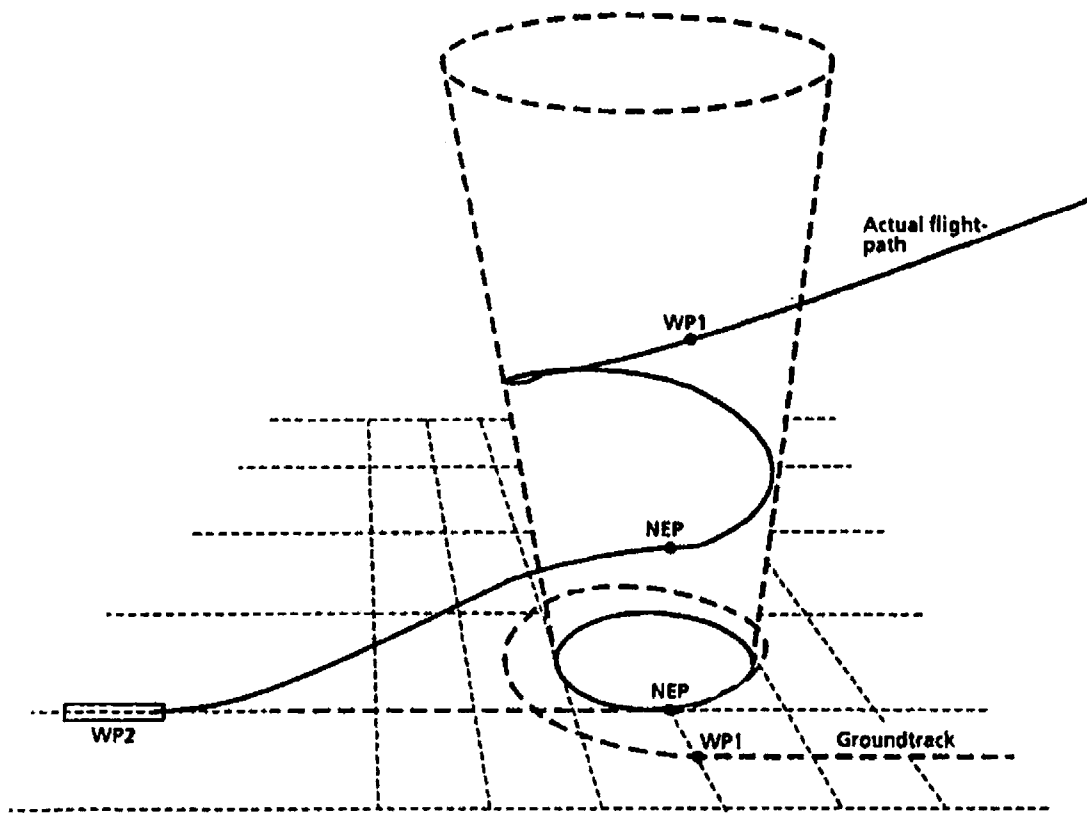


Figure 3.3: Flight Path Along the HAC [9]

The last subphase in TAEM is the prefinal subphase. This exists to provide a brief time to allow any trajectory errors to settle before transitioning out of TAEM. Lateral position and rate errors with respect to the runway centerline drive the guidance bank commands.

The third guidance phase, approach and landing, begins at the Auto Landing Interface (ALI) which is usually placed at 10,000 ft altitude and a specified downrange distance corresponding to the approach geometry. An initial steep glide slope transitions to a circular flare (pre-flare), which exponentially decays to a final shallow glideslope. A final flare ensures a safe touchdown by achieving a vehicle sink rate within constraints and setting a well-behaved pitch angle.

### **3.2.2 X-34 Modifications**

The X-34 never reaches the altitude and speed conditions of the Space Shuttle's EI, since it is designed for only suborbital flight tests. Therefore, instead of using a true Entry phase, the X-34 guidance employs a Gliding Return To Launch Site (GRTLS) phase that executes a similar role. The GRTLS phase ends as the Entry phase does at the TAEM interface.

Figure 3.4 illustrates the basic guidance concept as currently implemented in the X-34. Based on measured vehicle states from sensors such as a Flush Air Data System (FADS) and an integrated Global Positioning System/Inertial Navigation System (GPS/INS), the guidance system formulates a series of commands that are fed to the vehicle's control system. From these guidance commands of speedbrake position, ( $\delta_{sb}$ ), roll angle ( $\Phi$ ), and acceleration along the vehicle's negative body Z axis, ( $n_z$ ), the control system generates a set of deflection commands that are fed to the vehicle's control surface actuators, thus influencing the vehicle dynamics. It should be noted that  $\delta_{sb}$  is not modulated while the vehicle remains supersonic. The guidance system uses a series of geometric curves and angular relationships to determine the lateral  $\Phi$  command (unless performing an S-turn, where it simply commands  $\Phi$  to its limit), but relies on loaded reference profiles to help

determine the  $\delta_{sb}$  and  $n_z$  commands. The format of these reference profiles changes with respect to different entry phases.

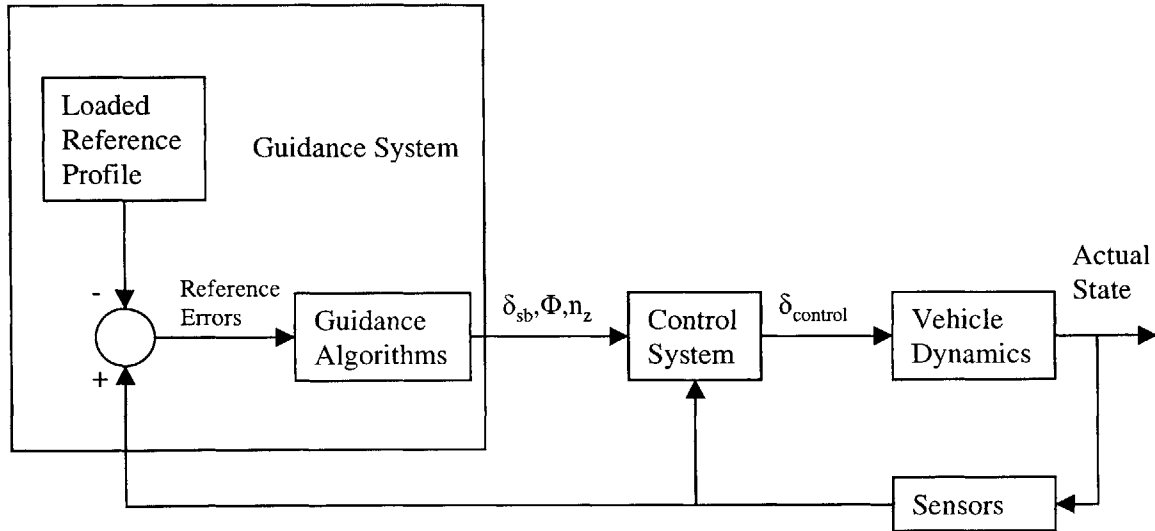
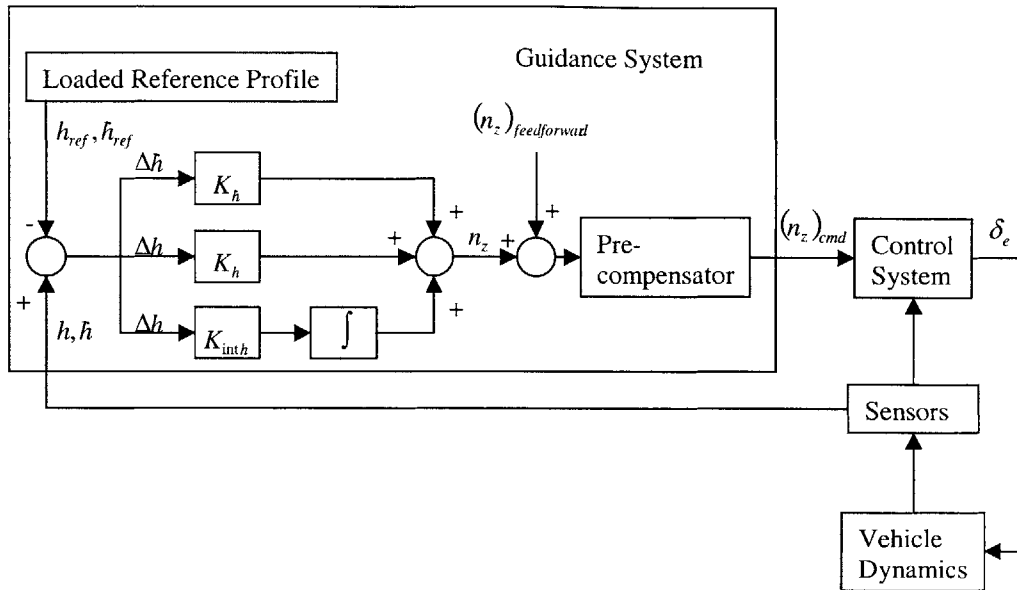


Figure 3.4: X-34 Guidance Concept

### 3.3 X-34 Guidance and Control Interaction

Traditional entry guidance relies on classical control techniques. Four independent loops handle the longitudinal, lateral, speedbrake, and rudder functions. The interaction between the guidance and control for the longitudinal loop is shown in Figure 3.5. Although the guidance changes depending on the current phase, it always provides a  $n_z$  command that the control system converts into an elevon deflection,  $\delta_e$ . In this manner, the guidance and control work together to keep the vehicle on its desired flight path.



**Figure 3.5:** Guidance and Control for Longitudinal Loop

The interaction between the guidance and control for the lateral loop is shown in Figure 3.6. Here the guidance system provides a roll command that is converted by the control system into an aileron deflection,  $\delta_a$ , which is really just a differential positional change between the starboard and port split elevons.

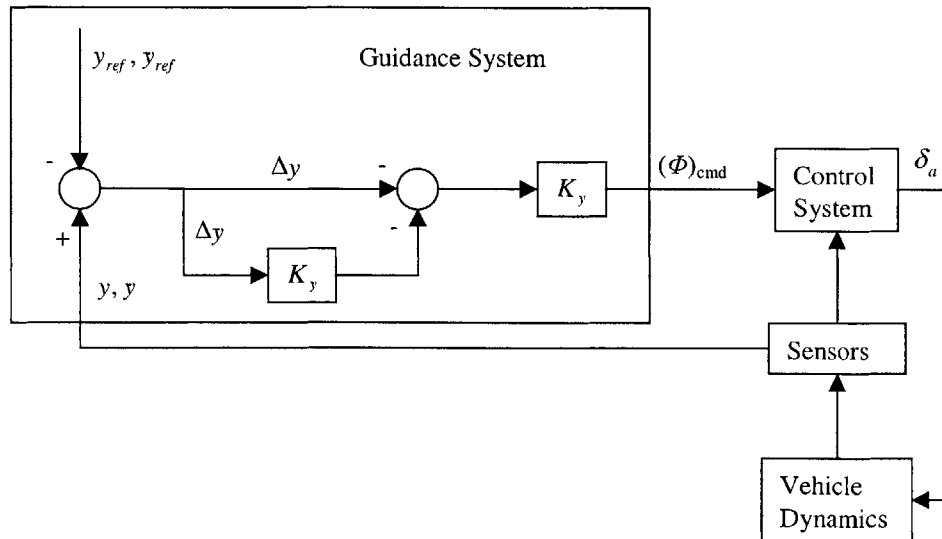


**Figure 3.6:** Guidance and Control for Lateral Loop



The speedbrake control handles energy errors, as shown in Figure 3.7. Only after the vehicle passes below Mach 1 can the speedbrake actively modulate energy errors in a closed loop manner; beforehand it functions open loop. After transition to the approach and landing phase, the speedbrake control reconfigures to manage speed rather than energy.

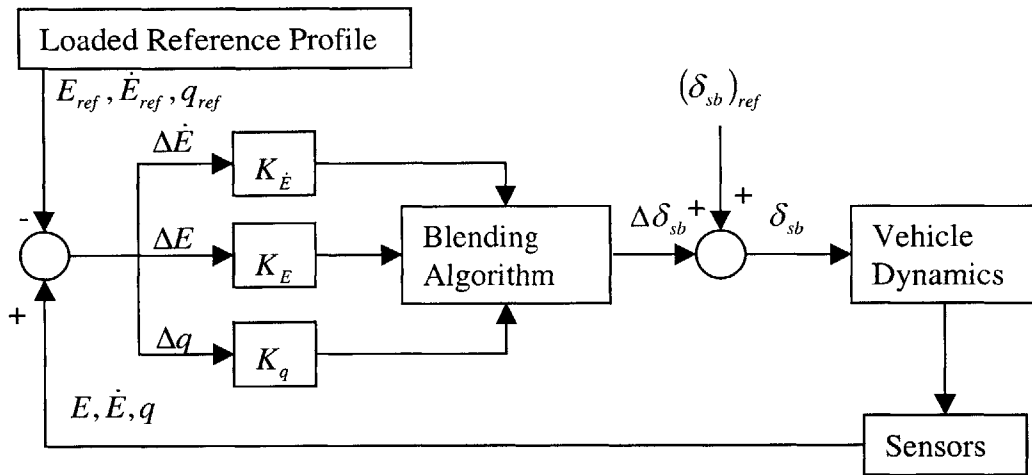


**Figure 3.7:** Speedbrake Control

The rudder control is entirely independent of the guidance system, receiving no guidance commands. It serves to prevent sideslip and minimize the lateral component of the vehicle acceleration during turning maneuvers [9]. The validity of the initial assumption of this thesis, that sideslip is always zero, depends upon tight control of sideslip through this rudder control function.



## Chapter 4

# Methodology for Onboard Design

### 4.1 Overview

The next generation guidance concept offers improvements over traditional entry techniques, but the requirement for onboard trajectory generation merits a shift in capability classification from automatic to autonomous. Extra care must be taken in the formulation of a system with a higher rating of artificial intelligence. This chapter considers the methodology of the algorithm design process, describing how the problem is dissected and contextualized into a coherent framework. First, an investigation of the challenges of autonomous algorithms identifies the primary hurdles to overcome. Next, a discussion of several fundamental design choices justifies the overall approach taken. Finally, the design inheritance from previous efforts is acknowledged and evaluated.

### 4.2 Challenges of Autonomous Algorithms

Autonomous algorithms for RLV guidance must solve the general problem of energy management for low L/D vehicles without violating system constraints. In essence, the critical task is to maintain flight capability in order to reach a specified landing target. Beyond solving the energy management problem, autonomous algorithms have fundamental requirements and desirable characteristics for onboard use.

Autonomous algorithms must satisfy the following fundamental requirements for onboard implementation:

- Guidance outputs must be usable by the flight system of the host vehicle
- The real time nature of the application requires quick solution convergence
- Robust formulation is vital since no human operator provides oversight and sanity checking

The robust formulation of these algorithms contributes to the autonomy (versus automation) by producing a large operating range. This, in turn, necessitates that the algorithms be able to determine their own regime of applicability by having the capacity to clearly define operational boundaries and limits for unspecified situations.

In addition to the fundamental requirements, the following characteristics are desirable for autonomous algorithms:

- Algorithms should be computationally efficient, not having to rely on supercomputing power to achieve their real time demands
- The resident architecture must provide straightforward implementation for future expandability
- Ideally, outputs for the current flight conditions would be optimized rather than merely satisfactory.

### **4.3 Fundamental Design Choices**

Several classes of fundamental design choices influenced the direction of the autonomous algorithm development process. They are categorized as onboard considerations, issues related to the integrated guidance and control framework, general scope and format decisions, and issues pertaining to optimization.

#### **4.3.1 Onboard Considerations**

The requirement for real time profile generation precludes heavy reliance on iterative trajectory shaping, placing a premium on smart decision-making and quick solution convergence. In this thesis, recent advances in computer technology are not used to push a computationally intensive “brute-force” approach wherein suitable trajectories are found through multiple iterations of a simulation tool. Rather, the approach chosen is a real-time design tool, using embedded intelligence and knowledge of key system dynamic tendencies as decision aids. The two approaches are shown in Figure 4.1.

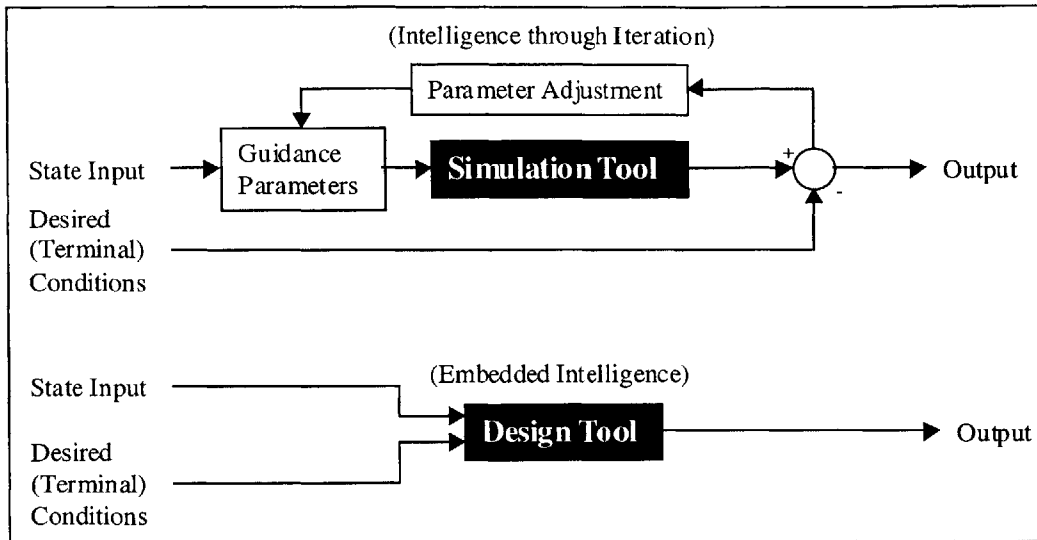


**Figure 4.1:** General Approaches to Onboard Trajectory Generation

The following definitions should clarify the distinction between system models:

**MODEL:** The set, sequence, and connectivity of representative elements used to capture a targeted relationship. In its simplest form, a model could be merely an equation:  $a=b+c$ .

**SIMULATION TOOL:** An algorithmic instrument that, given a set of *DESIGN INPUTS*, uses a *MODEL* to provide a set of *PERFORMANCE OUTPUTS*. One example of a real-time simulation tool is a flight sim. For example, by changing the rudder characteristics one can alter the vehicle dynamics, which, through a model, calculates the performance output of where a turn starts, if velocity decreases, etc.

**DESIGN TOOL:** An analytic instrument that, given a set of *PERFORMANCE* goals as inputs, uses a *MODEL* to provide a set of *DESIGN OUTPUTS*. Because it automatically determines a design, it requires a level of decision-making intelligence (and is more difficult to model than a simulation tool.)

A commonly used trajectory design software package called POST (Program to Optimize Simulated Trajectories), uses a simulation tool over numerous iterative cycles, where key trajectory parameters are varied until a desired trajectory quality is achieved [15]. There

exist numerous optimization approaches, well documented in the academic literature, that can avoid running simulation iterations for every possible input combination, using feedback and other advanced techniques (i.e. Taguchi methods, gradient searches) to smartly downselect to promising input values within the vast design tradespace. Nevertheless, iterations are still needed, and inflict their burden on the total computer time required.

Foreknowledge of key system dynamic tendencies leads to a design tool that concentrates on the most important tradeoffs. Limiting the design effort to the critical parameters concentrates computer resources proficiently, while not wasting time on options offering little, if any, improvement. Proper characterization of the trajectory problem is vital to this process, and is described in more detail in Chapter 5.

### **4.3.2 Integrated Guidance and Control Framework**

Formulating the trajectory design as a tightly coupled problem contributes to the effective and highly efficient design tool approach. In traditional Shuttle guidance, reference longitudinal design is kept distinct from reference lateral design. Energy, controlled by the speedbrake, is usually in a different guidance channel than trajectory, controlled by the elevons. Even the guidance and flight control systems are typically separated. The coupling of trajectory with energy, longitude with lateral, and guidance with flight control improves the robustness of the system design.

The integration of guidance and control, while dispensing with the traditional separation of domains, fundamentally alters the individual role performed by each constituent. This leads to overall improvements in cost, safety, and performance, but places new demands on the guidance system. The traditional guidance system, introduced back in Figure 3.1, keeps the guidance tasks as simple as possible, using loaded reference profiles to help determine three uncoupled commands ( $\delta_{sb}$ ,  $\Phi$ , and  $n_z$ ) that the control system then transforms into aerosurface deflections. This simplification minimizes the required computer power, which was an understandable design driver during the Space Shuttle's development years.

Integrated guidance and control (IG&C), shown in Figure 4.2, dispenses with the three uncoupled guidance “commands” and instead feeds the control function all the guidance references necessary to define an intended trajectory profile. The devised trajectory itself becomes the core of the “guidance” system. Table 4.1 lists a typical set of guidance references and Table 4.2 provides the trajectory control variables. The control function, no longer classical in nature, uses multivariable techniques to minimize the entire set of trajectory state errors, trading errors in one state for corrections in others, as necessary.

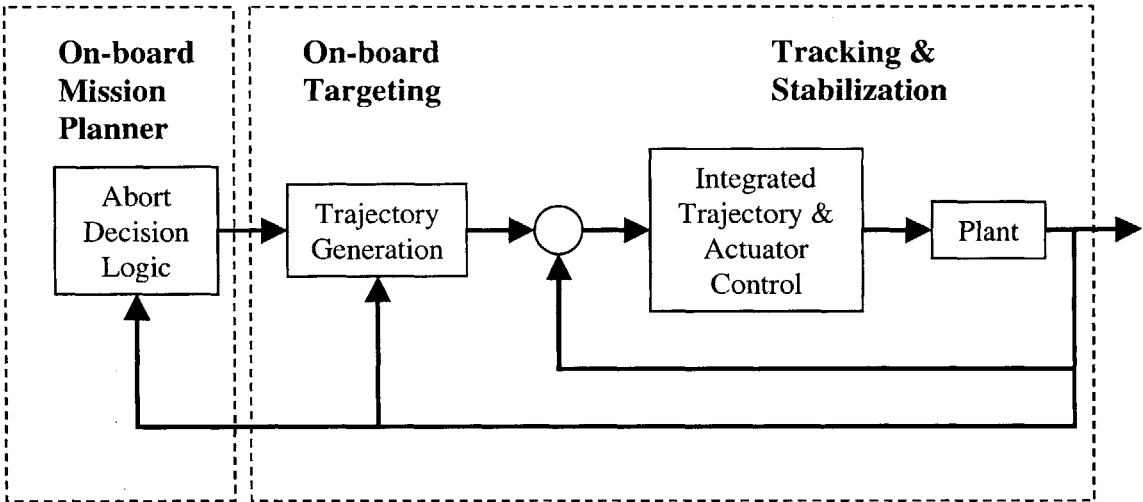


Figure 4.2: Integrated Guidance and Control Concept

Table 4.1: Guidance States

Guidance States	Symbol
Altitude	$h$
Inertial Velocity	$V$
x Position	$x$
y Position (crossrange)	$y$
Flight Path Angle	$\gamma$
Heading Angle	$\chi$

**Table 4.2:** Trajectory Control Variables

<b>Trajectory Control Variables</b>	<b>Symbol</b>
Angle of Attack	$\alpha$
Bank about the Velocity Vector	$\mu$
Sideslip Angle	$\beta$

While the IG&C function calculates the control surface deflections from a larger array of inputs, it does remove a significant amount of overhead in the Shuttle-based trajectory control when the current states are not aligned with the reference. Thus, the onboard-generated trajectory must be physically “flyable”, incorporating the actual conditions of the vehicle into the propagated plan. This represents a formidable design problem, since flyable trajectories, by definition, cannot induce constraint violations or impossible control demands. Historically, complete trajectories are generated offline for mission planning purposes, without regard to time constraints, but these (by definition) cannot incorporate actual vehicle states and are thus doomed to remain as canned references.

An onboard trajectory generator that captures actual vehicle physics and successfully produces a flyable flight plan has the additional advantage of integrating the effect of maneuvers well downstream of the current condition. Unlike traditional guidance, whose output commands react to perceived instantaneous vehicle needs, the integrated guidance provides a realistic “future history” in a propagated plan, which can be analyzed completely for desirability and even optimality. In fact, a single trajectory could be generated onboard starting from the vehicle’s current state that might be sufficiently accurate to remain valid for the duration of flight. Regardless, the option always exists for a near-instantaneous trajectory replan, if actual and projected conditions diverge out of tolerance.

Designing the entire trajectory, instead of just following a canned reference, allows a holistic approach with numerous benefits. For example, the RLV can receive radio updates of current wind conditions at various altitudes, evaluating the downstream consequences on energy margins and intelligently incorporating the anticipated effect in



the flight plan design well before reaching the actual winds. The full impact of downstream banking maneuvers that dump lift and alter groundtrack distance can also be taken into account. An entire trajectory history provides feedforward information to the control functions, which improves performance and maintains robustness.

### 4.3.3 General Algorithm Scope and Format Decisions

The inherent difficulty, or impossibility, of seeking an analytical solution to a complete trajectory for flight within the atmosphere necessitated numerical methods. The desire for high precision (thus highly usable) output led to the preservation of the full nonlinearity of the problem. Therefore, the approach avoided the attendant errors and added complexity of finding suitably small trajectory segments for linearization.

To generate guidance states, a propagation technique is used that balances the dynamics necessary to maintain the flight conditions along a trajectory of imposed geometry. This approach, described later in Chapter 5, also provides the trajectory control variables  $\alpha$  and  $\mu$  ( $\beta$  is assumed to be zero). Furthermore, control surface deflections can be extracted. For example, the required elevon position,  $\delta_e$ , is bound by trimming the vehicle for each  $\alpha$ . The speedbrake position,  $\delta_{sb}$ , also factors into the physical relationships. Therefore, in addition to defining the guidance state variables of a complete 3-DOF trajectory, knowledge of the complete trajectory control history and selected aerosurface deflection data allows the control functions to access feedforward information for better response. For example, knowing the future required position of the speedbrake will alert the flight control to begin the actuation command in advance, removing lag. It should be mentioned that the elevon position is only accurate for purely longitudinal maneuvers, as the split behavior of the port and starboard elevons for banking actions is not addressed due to the assumption of steady state bank conditions and uncorrelated changes for each altitude step.

It is important to note that while the variables defining a 6-DOF trajectory can be provided, a full 6-DOF implementation is not used. This has the advantage of omitting

the computationally intensive integration of the three rotational equations of motion, but has the disadvantage of bypassing physical rate-of-change limitations on some trajectory variables. For example, although each  $\alpha$  along the trajectory is exact, the implied change in  $\alpha$  between two trajectory points is not guaranteed to be physically realizable, especially at geometric segment transitions. The body roll, pitch, and yaw rates ( $P$ ,  $Q$ , and  $R$ ) can be found by differentiating between known successive roll, pitch, and yaw positions. Although not obtained through a pure 6-DOF method, the time-averaged values of these rates serve as an excellent guide for the flight controller, especially over the integration step sizes typically encountered.

#### **4.3.4 Optimization Issues**

The issue of optimization requires some context. “Optimization” is a key term possessing slightly different shades of meaning in different technical subtexts and communities. Indeed, optimization is always with respect to a parameter or set of parameters that serves as a comparison metric. When speaking about optimum trajectories, one should be very specific. For gliding flight, a typical evaluation parameter is the final energy error. However, reaching the required terminal conditions from a wide (though bounded) variety of initial conditions usually poses few problems to a vehicle with the flight capabilities of the X-34. In other words, many trajectories can be designed that satisfy the imposed constraints. In an energy management problem, in addition to satisfying end requirements, it is desirable that the *path itself* be optimized with respect to a figure of merit. This leads to the following two definitions used throughout the remainder of this thesis:

***ROBUSTNESS*** – Tolerance to dispersions.

***“OPTIMIZED” TRAJECTORY*** – Trajectory with maximum duration at a condition of maximum robustness.

It is important to note that the onboard trajectory generator is not formulated to provide a truly optimized output in the most strict sense. Mandating such a result could impose

severe burdens on computation time. Real-time, truly optimized, onboard trajectory generation is beyond the scope of this thesis. Therefore, it is more strictly accurate to describe the onboard guidance trajectories produced by this method as “feasible” rather than “optimal”. Nevertheless, the autonomous algorithms do seek the “best” solution within a restricted set of satisfactory solutions constrained by the geometric formulation of the design tool, so a process of optimization definitely does occur. A technique described in Chapter 5 handles this process sufficiently quickly to enable its real-time implementation. Therefore, the autonomous algorithms drive toward an “optimized trajectory”, although with the aforementioned caveat concerning strict usage of the term.

## **4.4 Design Heritage**

Many fundamental design methodology decisions were influenced by techniques used in the Auto Landing I-Load Program (ALIP) developed by Gregg Barton of Draper [11]. This software program for rapid pre-mission design of autoland trajectories for the X-34 served as a valuable starting point for onboard trajectory generation in the subsonic TAEM regime.

ALIP designs unpowered reference trajectories from the ALI at 10,000 ft to touchdown. The use of well-defined geometric segments (steep glide slope, circular flare, exponential decay, shallow glide slope, and final flare) enables a constrained trajectory propagation technique to solve for exact vehicle dynamic states and control histories. ALIP operates with altitude rather than time as the independent variable in the reformulated equations of motion so as to allow the specified geometry to reduce the order of the system.

ALIP pioneered some crucial techniques for fast generation of inherently flyable trajectories, but remains unsuitable for onboard implementation. It incorporates only the longitudinal flight dynamics, restricting flight to a two dimensional plane. This is not problematic for the autoland segment, when all crossrange errors have been significantly reduced, but is clearly inconsistent with the banking maneuvers of TAEM. ALIP also uses a two point boundary value problem formulation, but of unconstrained range. This is illustrated in Figure 4.3, where variation in the initial downrange state is

used to remove landing energy errors at the final state. The variable  $X_{ZERO}$  represents the outer glideslope intercept with the landing altitude. Although converging nicely, several complete trajectories are generated before finding the final solution. This technique, known as a “shooting method,” is perfectly suitable for offline design, but is undesirable for the real-time needs of an onboard system. Furthermore, geometric variations in initial conditions are a necessary part of designing reference autoland trajectories, but an onboard system is forced to design from a single set of unique initial conditions. In other words, the initial conditions for an onboard system are completely defined, so the two point boundary value problem is constrained in range.

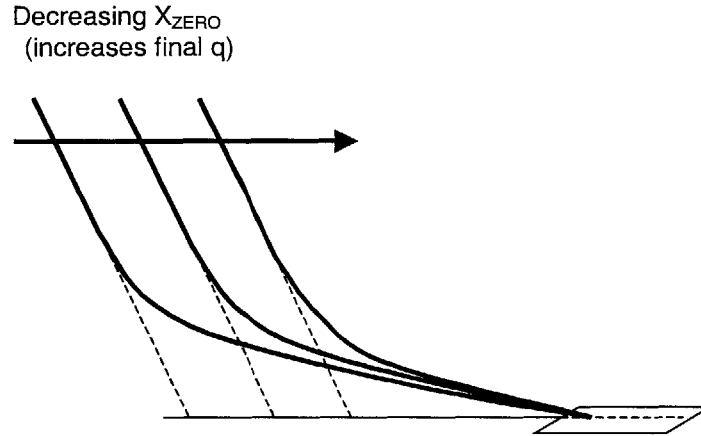


**Figure 4.3:** Effect of Decreasing  $X_{ZERO}$

## Chapter 5

# Onboard Trajectory Generation Technology Components

### 5.1 Introduction and Overview

This chapter seeks to introduce the various enabling techniques in detail, showing relevant functionality from a component-level perspective, and describing the rationale behind the development process. A thorough understanding of each individual component allows greater appreciation for the system-level interactions between components as described in Chapter six. Five key technology component classifications emerge, allowing the current implementation of onboard trajectory generation. These are listed as follows:

***Two point boundary value problem (TPBVP)*** - Captures the required and desired states, incorporates system constraints, and simplifies a difficult problem while maintaining fidelity.

***Constrained trajectory propagation*** - Rapidly generates realistic trajectories with exact control histories by using a specified geometry to reduce the order of the dynamic system.

***Fast Tradespace Scanning*** - Offers an efficient method for discovering a range of allowable trajectories without resorting to iterative techniques.

***Adaptive center-of-capability reference*** - Serves as the enabling ingredient for subsequent optimization.

***Optimized trajectory computation*** - Quickly outputs an inherently flyable reference that is optimized for robustness.

## 5.2 Two Point Boundary Value Problem

### 5.2.1 Rationale and Overview

The onboard trajectory generator calculates a trajectory solution between the known initial states and the desired terminal states. The initial (subsonic TAEM) and terminal (ALI) states represent the two points of the Boundary Value Problem. Table 5.1 lists the boundary value states and terminal conditions for a typical approach and landing profile. The path between the boundary values is composed of geometric segments that are designed to keep the vehicle within its performance limits.

**Table 5.1:** States and Conditions for Approach and Landing Profile

<b>Boundary State</b>	<b>Initial Condition</b>	<b>Terminal Condition (ALI)</b>
Altitude	Initial $h$	10,000 ft
Dynamic Pressure	Initial $q$	335 psf
x position	Initial $x$	33,668 ft
y position	Initial $y$	0 ft
Flight path angle	Relaxed	-20.5 degrees
Heading angle	Initial $\chi$	0 degrees

Using well-defined longitudinal and lateral geometric segments while enforcing dynamic constraints such as loads and continuity condenses the design effort into the convenient TPBVP. It should be emphasized that these boundary conditions are always of fixed range (straight line distance), although the groundtrack distance will vary with alternate lateral profiles. The advantage of this geometric approach is that it simplifies the design problem while enforcing intrinsically flyable and controllable guidance outputs. Thus the possibility does not exist, for example, of unwelcome phugoid motions to which the flight control cannot respond adequately.

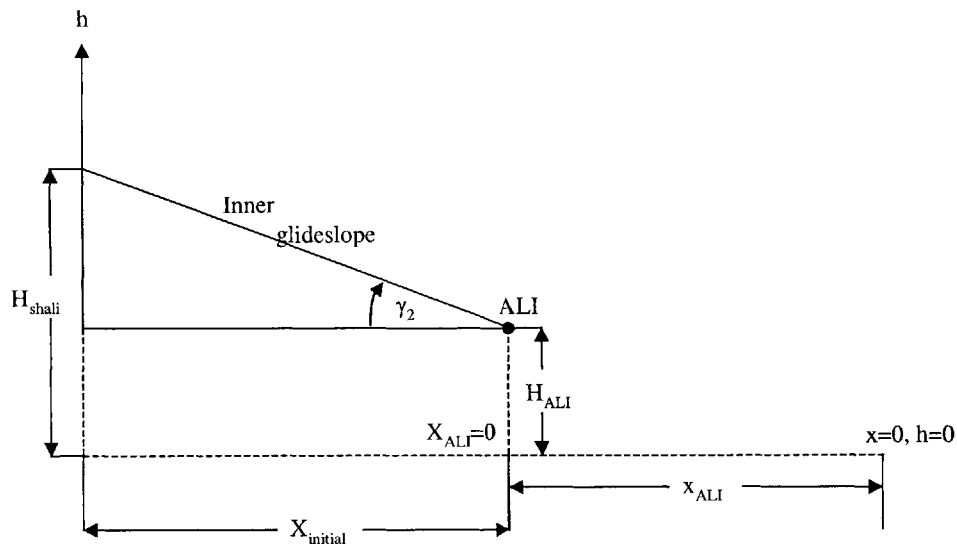
The three dimensional geometry is split into longitudinal and lateral design spaces for convenience. While described separately in this chapter for clarity, these spaces are coupled both geometrically and dynamically. Chapter six provides a full description of the coupling procedure.

Relaxation of the initial gamma constraint allows the chosen geometric framework to be applied without inconsistency. In addition, it frees gamma as a trajectory parameter for tradespace searches. Reintroduction of the gamma constraint after trajectory propagation is deferred to the flight control system, which capitalizes on the flight control’s inherent capability without imposing additional complexities on the guidance tasks.

## 5.2.2 Longitudinal Formulation

### 5.2.2.1 Longitudinal Basics




With a fixed-point drop condition and a fixed-point ALI end position, the TPBVP is of set range. Figure 5.1 illustrates the basic longitudinal geometry as imposed by the TPBVP conditions. Since the terminal gamma is specified at the ALI, it can be represented in the two-dimensional geometry as a glideslope, fixed in space, anchored at the ALI, and extended backward (upward) in altitude indefinitely. This glideslope is properly called the “inner glideslope”. The altitude,  $H_{shali}$ , of the inner glideslope intercept with the initial groundtrack can be above or below the actual initial altitude. The initial groundtrack is represented by an estimate of the projection of the flightpath onto the surface from the current state.



**Figure 5.1:** Basic Longitudinal Geometry

Figure 5.1 only shows the components of the geometric framework innately defined from the imposition of initial and terminal conditions, and clearly lacks the additional geometric information to describe a proper path. Indeed, the actual path cannot be innately defined, but is rather designed according to a chosen methodology. A wide variety of options exists for such a design, but for the purposes of onboard guidance the choice of a limited number of simple geometric segments emerges as most attractive. A combination of linear and circular arc segments provides longitudinal flexibility in the most straightforward manner, without the added complexity of complex curvilinear segments of higher order. In addition, the successful use of simple geometric segments in longitudinal trajectory design has been demonstrated effectively by the existing Shuttle approach and landing guidance. Table 5.2 lists the simple geometric segments.

**Table 5.2: Geometric Segments**

<b>Segment</b>	<b>Form</b>	<b>Description</b>
Straight Line		Linear segment of constant gamma
Flare		Constant decrease in the magnitude of gamma w.r.t. altitude
Anti-flare		Constant increase in the magnitude of gamma w.r.t. altitude

#### 5.2.2.2 Compound vs. Non-Compound Curves

With the adoption of simple geometric segments for path planning, the question then becomes how many of each segment type should be used. The identification of two major classes of geometric combinations provides the proper background for the eventual design decision. These two classes are compound-curve and non-compound-curve trajectories.

**Definition of Compound-Curve Trajectory:** Any trajectory that combines multiple flares and/or anti-flares, even though the curves may be adjoining or separated by a straight-line segment.



Figures 5.2 and 5.3 provide examples of compound curve trajectories. Note that the “outer glideslopes” are anchored at the initial location coordinates and determined by the choice of initial gamma. Figure 5.2 shows two trajectories with adjoining circular flares and anti-flares that commence with different initial flight path angles and thus different outer glideslopes. Either a flare/anti-flare or an anti-flare/flare combination brings the path to a tangential intersection with the inner glideslope. Note that in one case, a large radius anti-flare satisfies the terminal gamma condition no earlier than the ALI, without any prior duration on an inner glideslope. The two path examples of Figure 5.2 show compound curve trajectories using three or four segments. Compound curve trajectories using only two segments (not shown) are also possible. Figure 5.3 illustrates a compound curve trajectory with five segments using an anti-flare and a flare that are not adjoining, but separated by an intermediate linear segment.

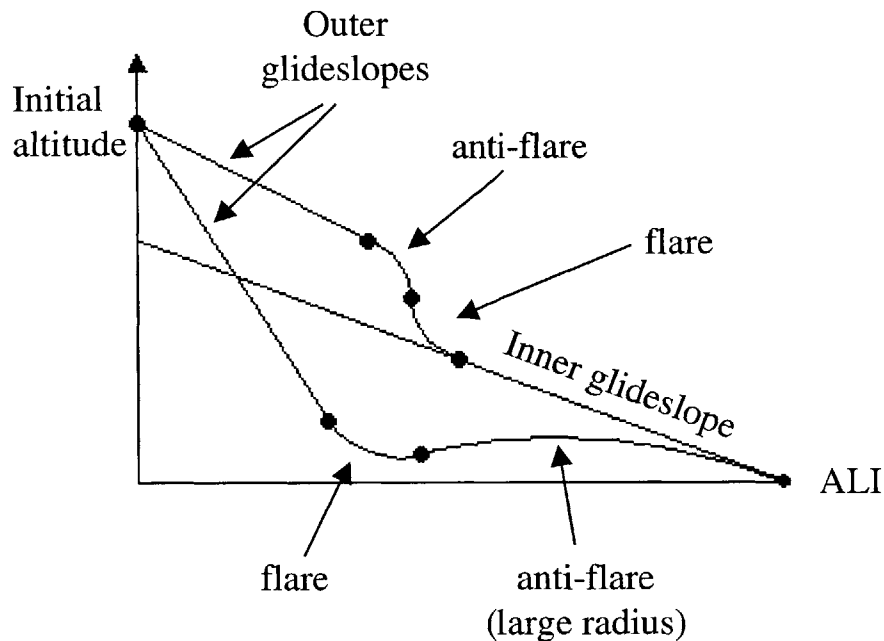


**Figure 5.2:** Compound Curve Trajectories (3-4 Segments)

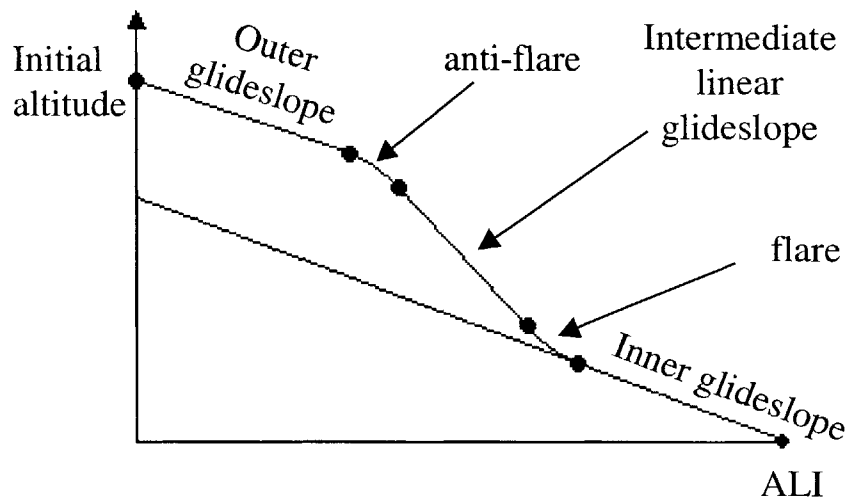


**Figure 5.3:** Compound Curve Trajectory (5 Segments)

The use of compound curve trajectories engenders a large variety of geometrically suitable paths that satisfy the geometric boundary conditions. (Dynamic suitability will be addressed later.) In fact, some formulations of compound curve trajectories can traverse the entire two-dimensional four-sided rectangular longitudinal region bounded by the initial altitude, initial downrange, final altitude, and final downrange. This suggests any point within that region could be a viable candidate for a waypoint through which the trajectory passes. For completeness, it must be noted that total coverage of the extreme corner regions is only theoretically possible in the limit as the radii of curvature of the flares or anti-flares approach zero, which would not obviously represent flyable maneuvers. In addition, trajectories using non-negative glideslopes (enabling maneuvers with altitude increases) with a sufficient number of segments could even leave the rectangular region and still satisfy the geometric constraints. Clearly then, meeting the geometric boundary conditions is a necessary but insufficient driver for path planning. More design guidelines are needed.

In the search for a suitable path planning method, the following design rules emerged:

- Satisfy Geometric Constraints
- Enforce Practical Solutions
- Minimize Complexity (while guaranteeing flexibility)

The word “practical” is a subjective term, but for the purposes of gliding entry guidance it enforces all trajectories to decrease in altitude monotonically. In addition, it outlaws designs with poor flight behaviors like steep vertical dives and extended durations at overly shallow glideslopes, effectively limiting trajectories to benign, straightforward, and commonsense plans. For example, the two trajectories of Figure 5.2 would violate the practicality guidelines, since the upper trajectory approaches a near vertical dive between its anti-flare and flare, and the lower trajectory violates the principle of monotonic altitude decrease. By contrast, Figure 5.3 illustrates a practical trajectory.

Although some formulations of compound curve trajectories result in practical path solutions, there exist unnecessary degrees of freedom in the design choice, often resulting in a huge and unwieldy tradespace. In essence, compound curve trajectories fail to minimize design complexity, posing trajectory design problems classified as underdetermined.

A trajectory class does exist that satisfies all three design rules for a suitable path planning technique. It utilizes non-compound curve trajectories.

***Definition of Non-Compound Curve Trajectory:*** Any trajectory comprising up to three geometric segments, but including only one flare or anti-flare.

Figure 5.4 shows an example of a non-compound curve trajectory. In the case depicted, an outer glideslope transitions to an inner glideslope by means of a circular flare. All non-compound curve trajectories satisfy the geometric constraints of a TPBVP, enforce practical solutions when combined with easily automated parameter constraints, and minimize design complexity while offering flexibility. In fact, only two parameters are needed to completely determine a path: (1) the initial glideslope, and (2) the tangent point on that initial glideslope where the circular flare (or anti-flare) commences. For the remainder of this thesis, we will consider the arc radius  $R$  as the second parameter, since the information provided by the tangent point is also supplied by  $R$ , due to the geometry of the non-compound curve formulation. Basically, by imposing the design constraints of

a non-compound curve trajectory, the design problem becomes tractable. It might be argued that this approach limits the available tradespace and thus discards trajectory options potentially more nearly optimal for hypothetical criteria. However, for the vital purposes and real-world demands of an onboard trajectory designer the simplicity, straightforward workability, and high inherent flexibility make it an ideal framework.

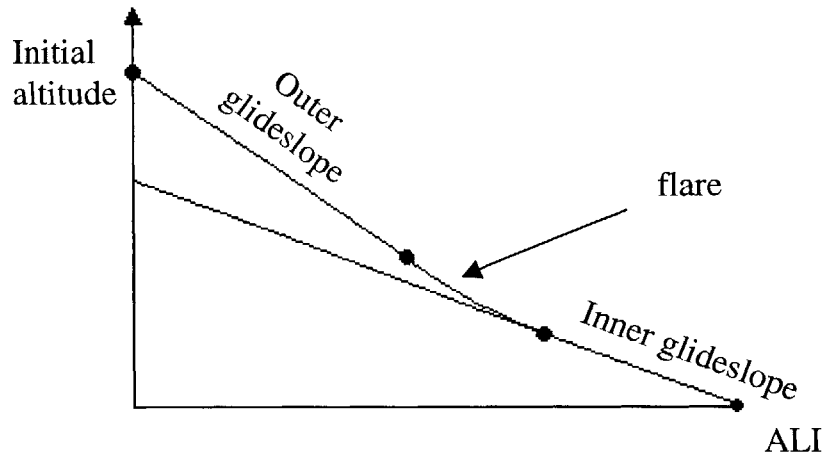


**Figure 5.4:** Non-Compound Curve Trajectory

### 5.2.2.3 Longitudinal Geometry

Restricted to non-compound curves, the longitudinal aspects of the trajectory can be defined entirely by the parameters listed in Table 5.3 and shown in Figures 5.5 and 5.6.

**Table 5.3:** Defining Geometric Parameters

Parameter	Description	Dependencies
$\gamma_1$	Outer glideslope	Chosen
$\gamma_2$	Inner glideslope	Given
R	Radius of curvature of the circular arc	Chosen
$X_{ZERO}$	Outer glideslope intercept with ALI altitude	Derives from $\gamma_1$
XK	Groundtrack distance between $X_{ALI}$ and the center of the circular arc	Derives from R, $\gamma_1$ , and $\gamma_2$
HK	Altitude of the center of the circular arc	Derives from R, $\gamma_1$ , and $\gamma_2$
$H_{LOOP}$	Altitude of circular arc initiation	Derives from R, $\gamma_1$ , and $\gamma_2$

Figure 5.5 shows an example of a *flare* trajectory that occurs whenever the following condition is met:

$$(H_{REF1} > H_{shali}) \rightarrow (|\gamma_1| > |\gamma_2|) \quad (5.1)$$

Due to the non-compound curve formulation, whenever the initial altitude,  $H_{REF1}$ , exceeds the altitude of the inner glideslope intercept with the initial groundtrack,  $H_{shali}$ , the magnitude of the outer glideslope must be greater than the magnitude of the inner glideslope. This is a necessary though insufficient condition for an appropriate intersection between glideslopes (the additional sufficiency requirement is introduced in section 5.4). For the purposes of the current discussion, the condition simply requires a transition from a steep to shallow glideslope, and thus necessitates a flare.

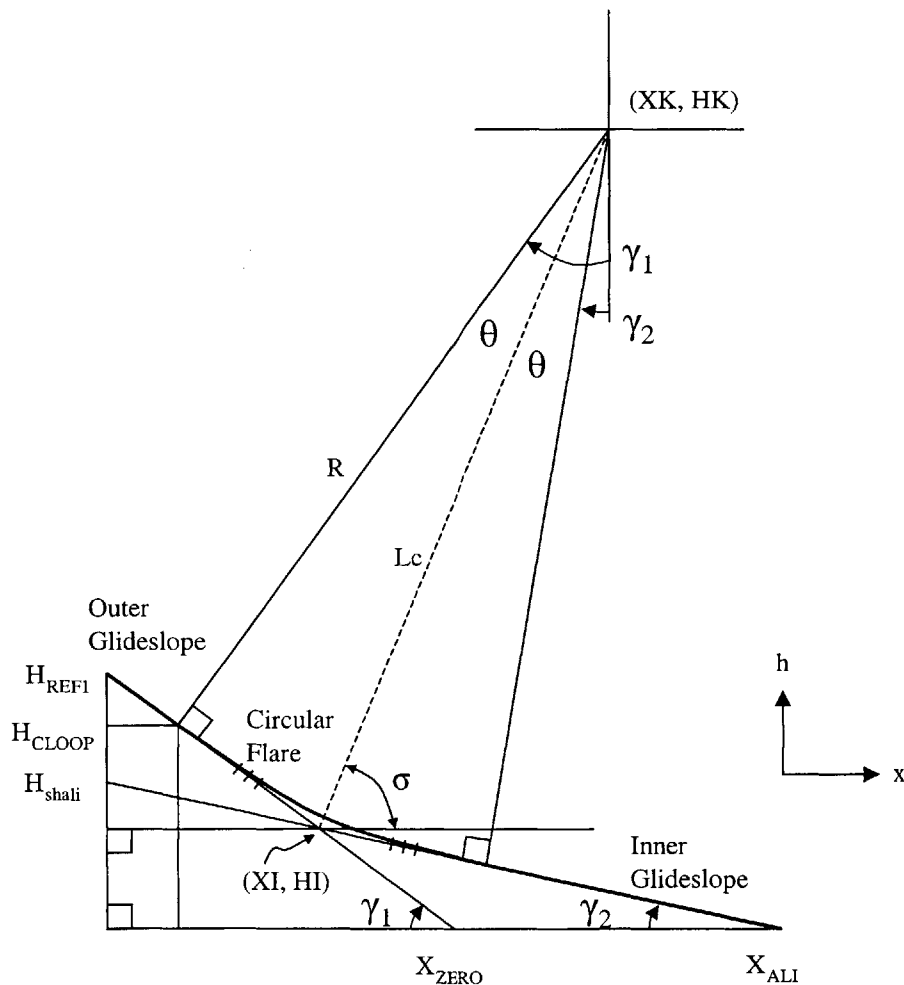


**Figure 5.5:** Flare Trajectory Particulars

In addition to showing the parameters of Table 5.3, Figure 5.5 introduces some helpful terms that highlight salient geometric features of the non-compound curve trajectory. The circular flare arc of radius  $R$  and turn angle  $2\theta$  is bisected by the locus line  $L_c$ , which runs from the intercept point (XI, HI) of the two glideslopes to the center of the arc circle (XK, HK). Even before choosing a radius length, the locus line is fixed in space from its anchor at the intercept point and its horizontal reference angle  $\sigma$ , an angle only dependent on  $\gamma_1$  and  $\gamma_2$ . In addition, the half turn angle  $\theta$  is independent of  $R$ , so every possible flare arc will traverse the same angle about its center for a set  $\gamma_1$  and  $\gamma_2$  combination.

Figure 5.6 illustrates the value of the locus line. For a single combination of glideslopes, the family of allowable flare curves will have centers along the locus line. In other words, Figure 5.6 demonstrates the remaining variations in trajectory stemming from the design parameter  $R$ , after the first design parameter ( $\gamma_1$ ) has been set. Note, in this rigid geometric framework, every possible radial vector must start oriented orthogonal to  $\gamma_1$ , and then, after a turn angle of  $2\theta$ , end orthogonally to  $\gamma_2$ . This negates path discontinuities by ensuring a smooth geometric transition of the actual trajectory with the flare initiation and termination instantaneously parallel to the local glideslope.

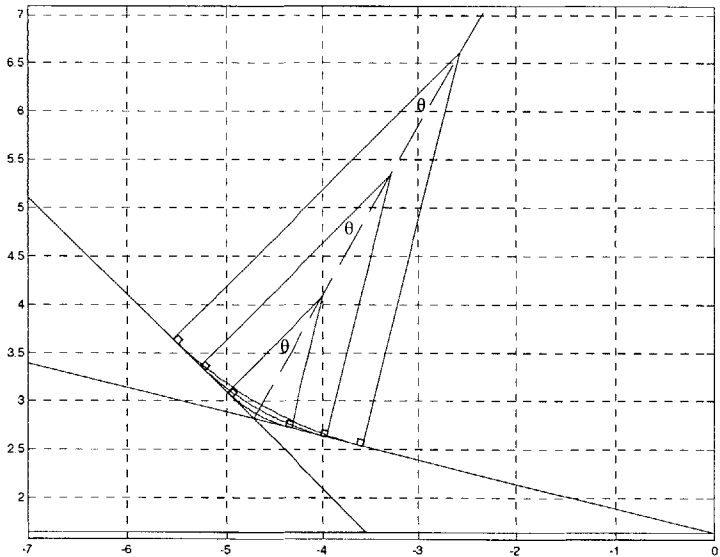


**Figure 5.6:** Locus Line for Flare Case

Figure 5.7 exhibits an example of an *anti-flare* trajectory that occurs when the following condition is met:

$$(H_{REF1} < H_{shali}) \rightarrow (|\gamma_1| < |\gamma_2|) \tag{5.2}$$

In the opposite scenario from the condition specifying a flare,  $H_{REF1}$  lies below  $H_{shali}$ , and therefore forces the magnitude of the outer glideslope to be less than the magnitude of the inner glideslope. This requires a transition from a shallow to a steep glideslope utilizing a diving maneuver called the anti-flare. Notice that  $X_{ZERO}$  lies beyond  $X_{ALI}$  (w.r.t. the initial condition), and the locus line extends downward in altitude.

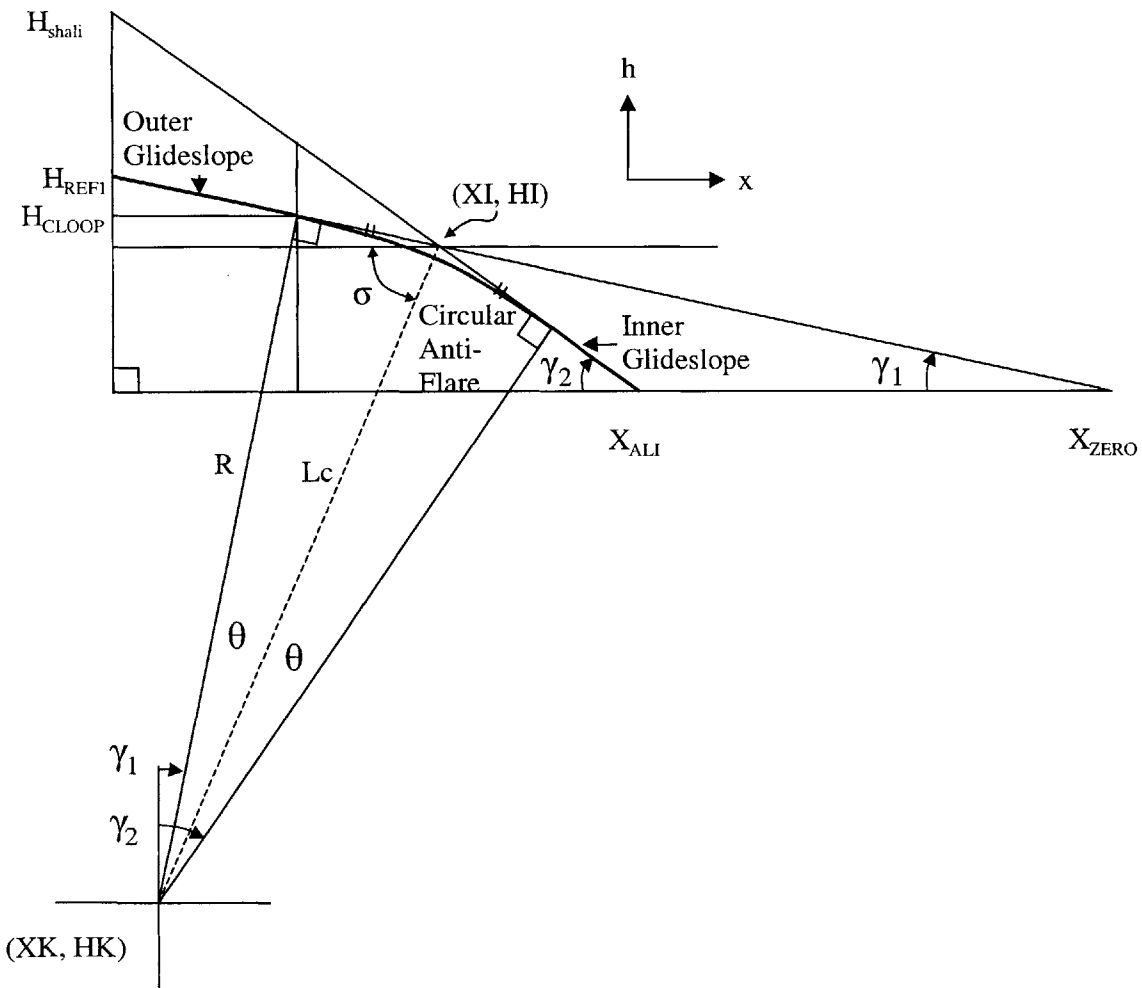


**Figure 5.7:** Anti-Flare Particulars

In a manner functionally identical to the flare case, the locus line for the anti-flare case governs the centers of the allowable arc segments as illustrated in Figure 5.8.

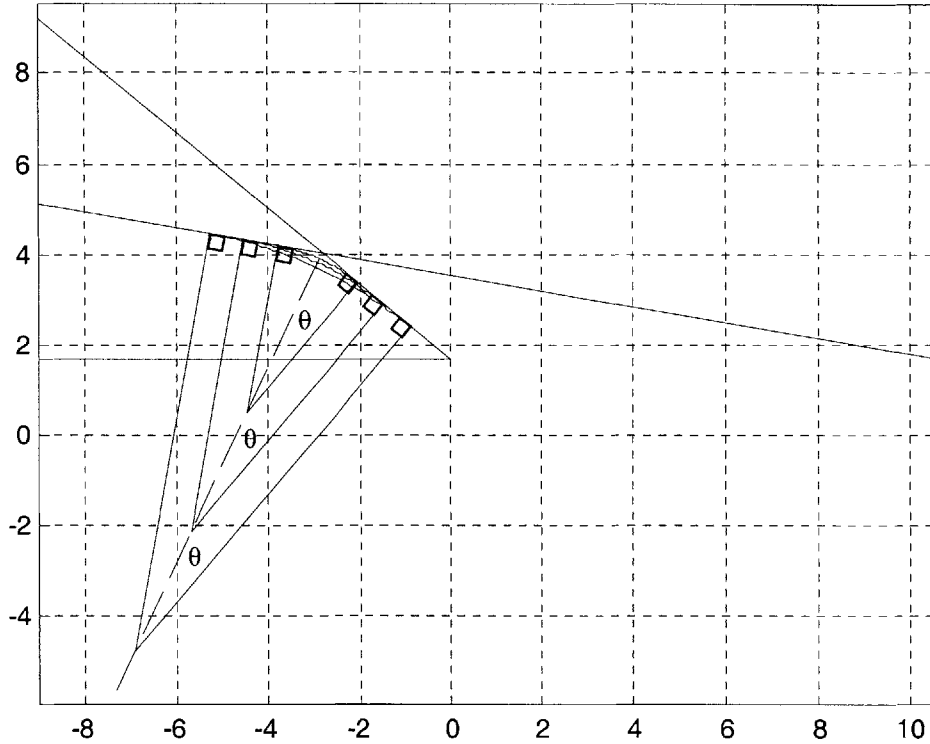


**Figure 5.8:** Locus Line for Anti-Flare Case

Although Table 5.3 introduced some of the dependencies of the key parameters and Figures 5.5-5.8 illustrated the significant graphical relationships, it is nonetheless important to provide the underlying definitions in equation form. The coordinates for the intersection of the inner and outer glideslopes are given by

$$XI = (X_{ZERO} \tan \gamma_1) / (\tan \gamma_1 - \tan \gamma_2) \quad (5.3)$$

$$HI = XI \tan \gamma_2 + H_{ALI} \quad (5.4)$$

Where the term  $X_{ZERO}$  is written in function form as



$$X_{ZERO} = X_{initial} - \left( \frac{H_{REF1} - H_{ALI}}{\tan \gamma_1} \right) \quad (5.5)$$

The two angular quantities  $\theta$  and  $\sigma$  are defined as

$$\theta = \frac{(\gamma_2 - \gamma_1)}{2} \quad (5.6)$$

$$\sigma = 90^\circ + \frac{(\gamma_1 + \gamma_2)}{2} \quad (5.7)$$

Equations 5.3-5.7 represent all the available geometric knowledge before finalization of the design parameter R. Choosing a value for R enables the calculation of the coordinates for the circular arc center, given by

$$XK = XI + \frac{R \cos \sigma}{\cos \theta} \quad (5.8)$$

$$HK = HI + \frac{R \sin \sigma}{\cos \theta} \quad (5.9)$$

With the design parameters set, the following equations provide a mathematical description of the resulting trajectory

$$h_{outer} = (X - X_{ZERO}) \tan \gamma_1 + H_{ALI} \quad (5.10)$$

$$h_{circ} \quad (\text{flare}) = HK - \sqrt{R^2 - (X - XK)^2} \quad (5.11)$$

$$(\text{anti-flare}) = HK + \sqrt{R^2 - (X - XK)^2}$$

$$h_{inner} = X \tan \gamma_2 + H_{ALI} \quad (5.12)$$

where  $h_{outer}$ ,  $h_{circ}$ , and  $h_{inner}$  are the vehicle altitudes for each of the geometric flight segments at an ALI-referenced groundtrack distance X. The value of this X is equal to zero at the ALI.

## 5.2.3 Lateral Formulation

The purpose of lateral guidance is to eliminate crossrange errors and bring the vehicle into heading alignment with the runway using a robust sequence of maneuvers. In a manner analogous to the longitudinal formulation, the lateral design space consists of a series of geometric segments that allow straightforward onboard trajectory calculation while offering flexibility to handle a variety of conditions. A vital element of the lateral guidance is the prediction of ground track distance to either the runway threshold or some intermediate waypoint such as the ALI. Many of the longitudinal elements are formulated as functions of the lateral-derived ground track distance, revealing the coupled nature of the two guidance divisions. For clarity, this subsection provides a thorough description of the lateral guidance as a distinct component, while Chapter six covers the nature of the inherent coupling.

### 5.2.3.1 Lateral Basics

Four geometric segments comprise the elements of the lateral framework, as shown in Figure 5.9. The first segment, the circular acquisition turn, changes the initial heading of the vehicle towards the tangency to the Heading Alignment Cone (HAC). Knowledge of the selected turn radius and the circular nature of the turn maneuver enables a straightforward calculation of the segment distance  $d_{AC}$ . The second segment,  $d_1$ , represents a linear connection between the end of the acquisition turn and the beginning of the HAC turn. The third segment,  $d_{HAC}$ , designates the distance traveled on the spiral HAC turn, and is calculated as a cubic function of the heading alignment turn angle,  $p_{sha}$ , and loaded radius parameters defining the spiral. The fourth segment,  $d_T$  denotes the straight line from the HAC end to either the runway threshold, or the ALI.

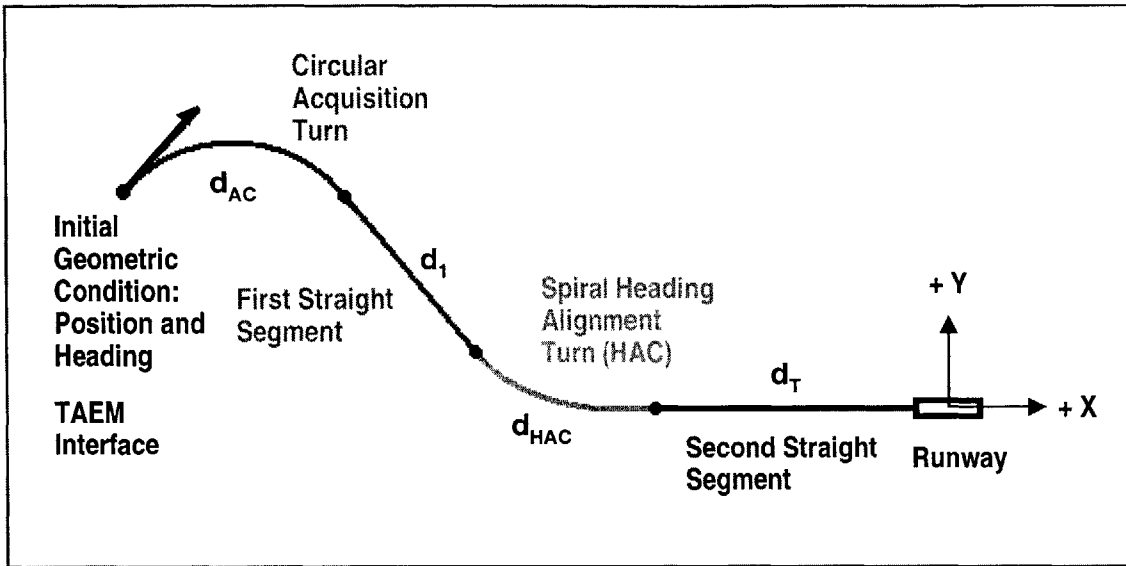
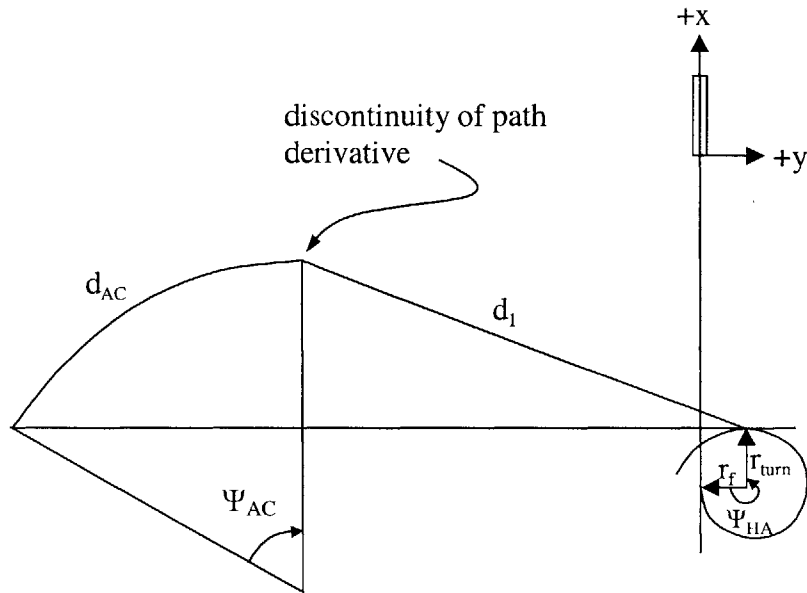


Figure 5.9: Elements of the Lateral Framework

### 5.2.3.2 Shuttle vs. Next Generation

The majority of the lateral guidance concept stems directly from methods pioneered by the Space Shuttle program, and subsequently adopted by the X-34. However, a slight though fundamental difference between the Shuttle and next-generation guidance goals prevented the sharing of identical technology. For the Shuttle, (and classic X-34), the role of the lateral guidance is to provide valid steering directions to the flight control during each guidance update. While serving this function as well, the next-generation guidance also seeks to produce a complete and valid trajectory reference for all future steps. The incompatibility is illustrated in Figure 5.10, which shows the traditional Shuttle lateral guidance segments with pertinent angle information.



**Figure 5.10:** Incompatibility of Shuttle and Next-Generation Lateral Guidance

The acquisition turn progresses through an angle  $\Psi_{AC}$ , which is the difference between the initial heading and a heading tangent to the HAC from that point. The segment  $d_1$  then connects the endpoint of the acquisition turn to the tangent point of the HAC turn. It is here where the incompatibility becomes obvious. The segment  $d_1$  is clearly not tangent to the HAC since the tangency point was determined from the initial position of the vehicle, not the projected position at the end of the acquisition turn. In addition, there is a discontinuity of the path derivative at the end of the acquisition turn, which is unacceptable for a physically flyable reference.

In fairness to the Shuttle guidance, it must be stressed that *over the course of time* a path will be followed with valid tangencies and no path discontinuities, as the acquisition turn particulars become slightly revised over each successive guidance step, with errors falling to zero in the limit. The Shuttle does not truly fly a geometrical lateral profile, as it commands a bank angle, with the resulting arc representing an estimate of the path assuming constant velocity. However, that path is not known in entirety at the initial position, and while the Shuttle technique may provide suitable directional inputs for the

immediate demands of the vehicle, the initial predicted ground track will be in error. Longer turns produce larger inaccuracies in the initial ground track estimate.

The next generation guidance computes the exact ground track distance for a trajectory of continuous path derivatives from the initial to terminal conditions without relying on successive updates over time. This improves the accuracy of the longitudinal guidance, which uses ground track distance referenced from the current condition. In addition, knowledge of the exact turn maneuvers required along the valid lateral trajectory contributes to the proper coupling of events downstream of the current condition, resulting in a more accurate lateral and longitudinal combination. Appendix B provides a description of the mathematical techniques used to assure tangency between the circular acquisition turn and spiral HAC turn.

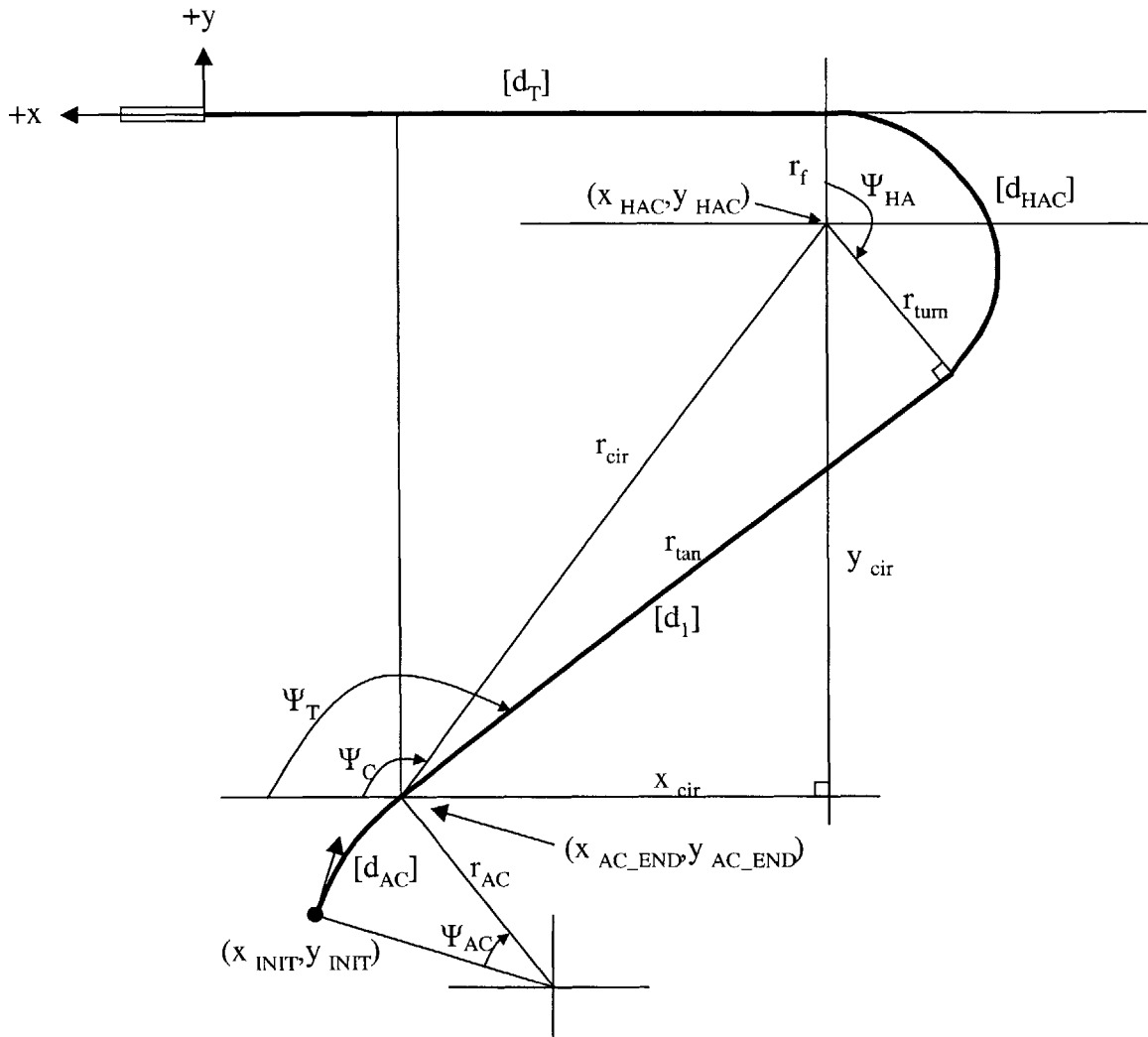
### 5.2.3.3 Detailed Lateral Geometry

Figure 5.11 provides a convenient reference for the geometric descriptions in this subsection. Proceeding backwards along the trajectory from the terminal condition, the final segment,  $d_T$ , is simply the distance along the x axis from the end of the HAC to the terminal condition. No crossrange errors exist in this segment of the reference trajectory, and any erupting in reality will be minimized by the flight control system.

The lateral position of the vehicle along the HAC turn can be given in polar coordinates by a radius,  $r_{turn}$ , and a HAC turn angle,  $\Psi_{HA}$ . Unlike a circle's constant radius, the HAC's spiral radius depends on its position in space, and is given by

$$r_{turn} = r_f + r_1\Psi_{HA} + r_2\Psi_{HA}^2 \quad (5.13)$$

where  $r_f$ , the final turn radius, and  $r_1$  and  $r_2$  are all constant coefficients which define the spiral.



**Figure 5.11: Lateral Geometry**

The center of the HAC which anchors the spiral is fixed in space at distance  $x_{HAC}$  away from the runway threshold along the x axis and at distance  $r_f$  along the y axis. The location of  $y_{HAC}$  is given by

$$y_{HAC} = (y_{SGN})r_f \quad (5.14)$$

where  $y_{SGN}$  is merely a sign indicator to place the HAC center on either side of the runway centerline. The  $y_{SGN}$  therefore toggles between straight-in and overhead HAC positions, as shown in Figure 5.12. A straight-in scenario places the HAC on the same

side of the runway centerline as the approaching vehicle, whereas an overhead scenario places the HAC on the opposite side. For the purposes of this thesis, only the straight-in scenario was implemented.

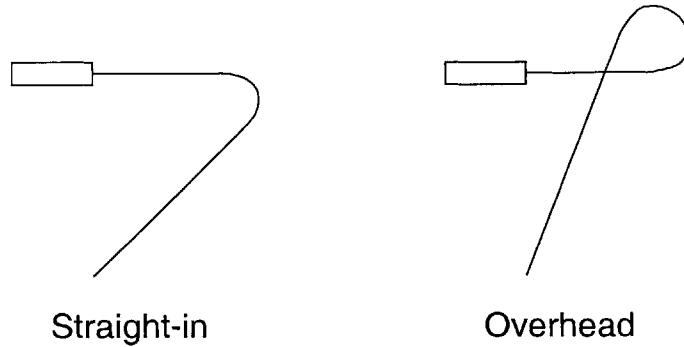


**Figure 5.12:** Straight-in and Overhead HAC Positions

The arc length distance  $d_{HAC}$  along the HAC spiral is given by

$$d_{HAC} = r_f \psi_{HA} + \frac{1}{2} r_1 \psi_{HA}^2 + \frac{1}{3} r_2 \psi_{HA}^3 \quad (5.15)$$

To find the segment distance  $d_1$ , a distance  $r_{cir}$  is first used to capture the distance from the acquisition turn end ( $x_{AC\_END}$ ,  $y_{AC\_END}$ ) to the centerpoint of the HAC, given by

$$r_{cir} = \sqrt{(x_{cir})^2 + (y_{cir})^2} \quad (5.16)$$

where the distances  $x_{cir}$  and  $y_{cir}$  are given by

$$x_{cir} = x_{HAC} - x_{AC\_END} \quad (5.17)$$

$$y_{cir} = y_{HAC} - y_{AC\_END} \quad (5.18)$$

Then, the desired distance  $d_1$  can be found from

$$d_1 = r_{tan} = \sqrt{(r_{cir})^2 - (r_{turn})^2} \quad (5.19)$$

where  $r_{turn}$  represents the HAC turn radius at the HAC initiation, and is calculated from equation 5.13 using the full  $\Psi_{HA}$ .

The heading to the center of the HAC,  $\Psi_C$ , is given by

$$\psi_C = \tan^{-1}\left(\frac{y_{cir}}{x_{cir}}\right) \quad (5.20)$$

The heading to the HAC tangency at which the spiral begins, is then

$$\psi_T = \psi_C - y_{SGN} \tan^{-1}\left(\frac{r_{turn}}{r_{tan}}\right) \quad (5.21)$$

The difference between the tangency heading and the initial heading is

$$\psi_{AC} = \psi_T - \psi \quad (5.22)$$

The distance along the circular acquisition turn arc,  $d_{AC}$ , is given by

$$d_{AC} = r_{AC} |\psi_{AC}| \quad (5.23)$$

where the acquisition turn radius  $r_{AC}$  is determined through tradespace considerations described in section 5.4.

The predicted ground track distance is the sum of the four geometric segment distances

$$r_{pred} = d_{AC} + d_1 + d_{HAC} + d_T \quad (5.24)$$

where segments  $d_{AC}$ ,  $d_1$ , or  $d_{HAC}$  may be set to zero for certain conditions.



## 5.3 Constrained Trajectory Propagation

### 5.3.1 Rationale and Overview

Section 5.2 introduced the two point boundary value problem and described the rationale for a trajectory generation approach using geometric segments. Of the six boundary guidance states of the TPBVP shown in Table 5.1, five are geometric and only one (dynamic pressure,  $q$ ) is dynamic. This section presents a method to calculate the  $q$  state along the trajectory by propagating the vehicle dynamics over a specified geometry. Since exact knowledge of the total path geometry is available before calculation of dynamics, the trajectory propagation problem is geometrically constrained. It is important to note that the specified geometry implicitly forces a control history, which, as shall be seen, can be utilized advantageously.

By imposing geometric constraints and satisfying the equations of motion at each position along the trajectory, we can determine the flight conditions necessary to maintain the trajectory. These flight conditions include the remaining guidance state  $q$ , as well as trajectory control variables such as angle of attack and bank angle. A constrained trajectory propagation technique introduced by Barton and Tragesser for longitudinal autoland analysis [11] reduces the order of the governing system by substituting the geometric trajectory constraint directly into the equations of motion. This provides an advantage for time-critical applications over traditional trajectory simulators, which perform computationally costly integrations of the equations of motion to arrive at desired guidance or control histories.

This section begins with the equations of motion and explains the decision to use dynamic pressure rather than velocity as one of the guidance states. Next it provides a rationale for switching the independent variable in the equations from time to altitude. Then, geometric variables are derived as functions of altitude for both longitude and lateral domains. Finally, the reduced-order governing equation is introduced and a propagation algorithm outlined.

### 5.3.2 Change of States

We begin with the equations of motion derived in Chapter 2 and reproduced here for ease of reference.

$$\dot{V} = \frac{-D}{m} - g \sin \gamma \quad (5.25)$$

$$\dot{\gamma} = \frac{1}{V} \left( \frac{L \cos \mu}{m} - g \cos \gamma \right) \quad (5.26)$$

$$\dot{\chi} = \frac{L \sin \mu}{mV \cos \gamma} \quad (5.27)$$

A change from velocity to dynamic pressure, as one of the guidance states, allows more benign behavior of these equations of motion. The dynamic pressure is given by

$$q = \frac{1}{2} \rho v^2 \quad (5.28)$$

Usually, a nominal entry profile is characterized by monotonically decreasing velocity, although atypical conditions like an abort or low altitude drop test may require localized regions of velocity increase. In general, for Eqn (5.28) the monotonically decreasing velocity component is partially countered by the monotonically increasing density component, resulting in dynamic pressure being a more slowly varying parameter than velocity alone[11].

In addition to improving the behavior of the equations of motion, switching the guidance state to  $q$  allows an intuitive grasp of a very important design feature embedded in the selection of the final glideslope. The equilibrium glideslope is defined according to the condition

$$\dot{\gamma} = 0, \dot{q} = 0 \quad (5.29)$$

where the derivative of  $q$  is zero for a constant  $\gamma$ . This condition is found through a solution of the two coupled nonlinear equations for a particular altitude, resulting in the flight path angle and an associated angle of attack. Variations in altitude will cause the equilibrium condition to change marginally, since the flight dynamics are non-linear with

altitude. Therefore, when the glideslope of an equilibrium solution is held constant at altitudes above or below the condition it uniquely solved, the dynamic pressure derivatives will be non-zero, but still very small. Thus, such a constant glideslope is properly defined as a quasi-static equilibrium glideslope over a local altitude range.

The final glideslope of TAEM is designed to be a quasi-static equilibrium glideslope calculated for a point at or slightly below the ALI. This has the beneficial effect of forming a natural bucket for the flight dynamics to converge to the desired ALI values, and therefore improves trajectory robustness. Energy errors tend to be rejected by the flight dynamics along the quasi-equilibrium glideslope, with the effect becoming more pronounced with increasing proximity to the ALI.

With the rationale for the state change from velocity to dynamic pressure established, we now step through the conversion derivation to transform Eqn (5.25) to an equation governing  $\dot{q}$ . Differentiating Eqn (5.28) with respect to time yields

$$\dot{q} = \frac{1}{2} \dot{\rho} v^2 + \rho v \dot{v} \quad (5.30)$$

Next, we conveniently rewrite  $\dot{\rho}$  as

$$\dot{\rho} = \left( \frac{d\rho}{dh} \right) \left( \frac{dh}{dt} \right) \quad (5.31)$$

where  $\frac{d\rho}{dh}$  can be obtained from an atmospheric model and easily extracted from tabular

data, and  $\frac{dh}{dt}$  is related to velocity via

$$\frac{dh}{dt} = \dot{h} = v \sin \gamma \quad (5.32)$$

Recalling the definition of the drag force  $D$  as

$$D = q S C_D \quad (5.33)$$

and substituting Eqn (5.25) into Eqn (5.30) while using the relationships of Eqns (5.28, 5.31, and 5.32) yields the sought after  $\dot{q}$  equation written as

$$\dot{q} = \dot{h} \left[ q \left( \frac{1}{\rho} \frac{d\rho}{dh} - \frac{\rho SC_D}{m \sin \gamma} \right) - \rho g \right] \quad (5.34)$$

### 5.3.3 Change of Independent Variable

Changing the independent variable in the equations of motion to altitude from time provides a more convenient analysis perspective since the time history of the trajectory is usually less interesting and useful than the altitude history. Additionally, the altitude history provides a superior link to the geometric history, which is fundamental to the constrained trajectory propagation approach. It should be stressed that the time history is not lost, since it can be extracted from the state variables when necessary. After transformation of the independent variable, Eqns (5.34, 5.26, and 5.27) are rewritten as

$$\frac{dq}{dh} = q \left( \frac{1}{\rho} \frac{d\rho}{dh} - \frac{\rho SC_D}{m \sin \gamma} \right) - \rho g \quad (5.35)$$

$$\frac{d\gamma}{dh} = \frac{\rho}{2 \sin \gamma} \left( \frac{SC_L \cos \mu}{m} - \frac{g \cos \gamma}{q} \right) \quad (5.36)$$

$$\frac{d\chi}{dh} = \frac{\rho g SC_L \sin \mu}{2W \sin \gamma \cos \gamma} \quad (5.37)$$

Interestingly, Eqn (5.37) governing the change in lateral heading has no explicit dependence on dynamic pressure. Solving equation (5.36) for  $q$  gives

$$q = \frac{W \cos \gamma}{SC_L \cos \mu - 2m \sin \gamma \left( \frac{1}{\rho} \frac{d\gamma}{dh} \right)} \quad (5.38)$$

### 5.3.4 Geometric Variables

The known geometry of the longitudinal trajectory allows  $\gamma(h)$  and  $\frac{d\gamma}{dh}(h)$  on the right hand side of Eqns (5.35, 5.37, and 5.38) to be expressed in closed-form. In addition, the known lateral geometry allows  $\frac{d\chi}{dh}(h)$  to be expressed in closed-form. This is made possible by the convenient change in the independent variable from time to altitude.

#### 5.3.4.1 Longitudinal Derivation

We now seek to find the flight path angle and its derivative as functions of altitude. The definition of flight path angle gives

$$\gamma = \tan^{-1}\left(\frac{dh}{dX}\right) \quad (5.39)$$

Differentiating Eqns. (5.10-12) provides the derivative  $\frac{dh}{dX}$  for each of the flight phases, and substituting the results into equation (5.39) gives the desired closed-form relationships

*Inner and Outer Glideslope:*

$$\gamma = \gamma_1, \gamma = \gamma_2 \quad (5.40)$$

*Circular Flare:*

$$\gamma = \tan^{-1}\left(\frac{\sqrt{R^2 - (h - HK)^2}}{h - HK}\right) \quad (5.41)$$

In order to find  $\frac{d\gamma}{dh}(h)$ , the chain rule is used to differentiate Eqn (5.39), giving

$$\frac{d\gamma}{dh} = \frac{\cos^2 \gamma}{\tan \gamma} \frac{d^2 h}{dX^2} \quad (5.42)$$

Proceeding, as before, by differentiating Eqns. (5.10-12) and substituting into Eqn. (5.42) we produce

*Inner and Outer Glideslope:*

$$\frac{d\gamma}{dh} = 0 \quad (5.43)$$

*Circular Flare:*

$$\frac{d\gamma}{dh} = \frac{1}{(HK - h)\tan \gamma} \quad (5.44)$$

#### 5.3.4.2 Lateral Derivation

We start with the circular acquisition turn, where the differential heading change is equivalent to the differential turn angle change, since the heading is always perpendicular to the turn angle radial vector. Hence

$$\frac{d\chi}{d\psi_{AC}} = 1 \quad (5.45)$$

Since the differential groundtrack distance along a differential turn angle is simply

$$dX = R_{AC} d\psi_{AC} \quad (5.46)$$

we can use Eqns. (5.39, 5.45 and 5.46) to arrive at

*Circular Acquisition Turn:*

$$\frac{d\chi}{dh} = \frac{1}{R_{AC} \tan \gamma} \quad (5.47)$$

For the straight lateral segments, the heading is by definition constant, so

*Straight Lateral Segments:*

$$\frac{d\chi}{dh} = 0 \quad (5.48)$$

To find  $\frac{d\chi}{dh}$  for the HAC spiral, we take a slightly different approach. Unlike the arc of a circle, the tangent to the curve of a spiral is not perpendicular to the radial vector. Knowing the HAC radius as a function of HAC turn angle (Eqn (5.13)), we can also derive the heading as a function of HAC turn angle. Since the heading is merely the tangent of the slope of the spiral path in the x-y plane, we find the slope in polar coordinates as a function of the HAC turn angle.

$$slope = \frac{dy}{dx}(\psi_{HA}) = \frac{\frac{dr}{d\psi_{HA}} \sin \psi_{HA} + r \cos \psi_{HA}}{\frac{dr}{d\psi_{HA}} \cos \psi_{HA} - r \sin \psi_{HA}} \quad (5.49)$$

Substituting Eqn (5.13) and its derivative into Eqn (5.49) yields

$$slope = \frac{(r_1 + 2r_2\psi_{HA}) \sin \psi_{HA} + (r_f + r_1\psi_{HA} + r_2\psi_{HA}^2) \cos \psi_{HA}}{(r_1 + 2r_2\psi_{HA}) \cos \psi_{HA} - (r_f + r_1\psi_{HA} + r_2\psi_{HA}^2) \sin \psi_{HA}} \quad (5.50)$$

Therefore, the heading angle as a function of psi becomes

$$\chi(\psi_{HA}) = \tan^{-1}(slope) = \tan^{-1} \left[ \frac{(r_1 + 2r_2\psi_{HA}) \sin \psi_{HA} + (r_f + r_1\psi_{HA} + r_2\psi_{HA}^2) \cos \psi_{HA}}{(r_1 + 2r_2\psi_{HA}) \cos \psi_{HA} - (r_f + r_1\psi_{HA} + r_2\psi_{HA}^2) \sin \psi_{HA}} \right] \quad (5.51)$$

The closed-form derivative of  $\chi$  with respect to  $\psi_{HA}$  is very large and unwieldy, so we use a simple numerical technique to compute the delta chi for each integration step. Tests have shown that

$$\frac{\Delta\chi}{\Delta h} = \frac{\chi_{n+1} - \chi_{n-1}}{h_{n+1} - h_{n-1}} \Rightarrow \frac{d\chi}{dh} \quad (5.52)$$

with excellent accuracy for the step sizes typically encountered. The center-point differencing numerical technique, shown in Figure 5.13, offers superior results over forward or backward differencing techniques for all but the first and last integration steps of a turn array.

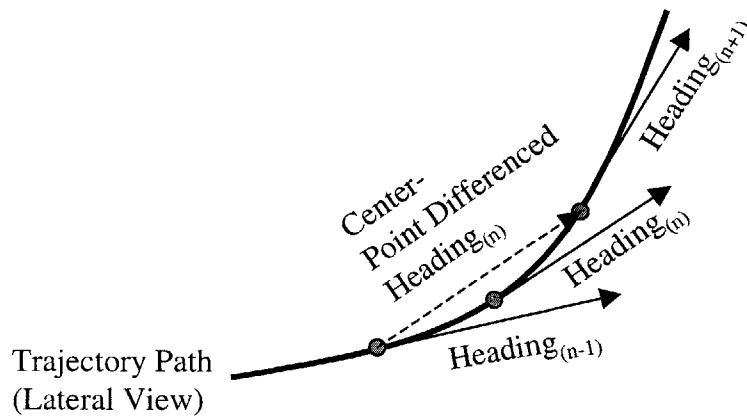


**Figure 5.13:** Center-Point Differencing Numerical Technique

### 5.3.5 Propagation Algorithm

The flight-phase-specific longitudinal geometric relations of  $\gamma$  (Eqns. 5.40, 5.41) and  $\gamma$  derivative (Eqns 5.43, and 5.44) can be substituted into the rewritten governing equations of motion (Eqns. 5.35 and 5.38) to yield a system of the form

$$\frac{dq}{dh} = f_1(q, \alpha, h) \quad (5.53)$$

$$q = f_2(\alpha, h, \mu) \quad (5.54)$$

To include the lateral component, we solve Eqn 5.37 for bank angle  $\mu$



$$\mu = \sin^{-1} \left( \frac{d\chi}{dh} \frac{2W \sin \gamma \cos \gamma}{\rho g S C_L} \right) \quad (5.55)$$

Substituting into Eqn 5.55 the longitudinal geometric relations of  $\gamma$  (Eqns. 5.40, 5.41) and the lateral geometric relations of  $\frac{d\chi}{dh}$  (Eqns 5.47, 5.48, and 5.52) yields

$$\mu = f_3(\alpha, h) \quad (5.56)$$

Therefore, since the bank angle is a function of the other variables in Eqn 5.54, we can condense Eqn 5.54 into

$$q = f_2(\alpha, h) \quad (5.57)$$

At this point, the value of enforcing the specified geometry becomes very clear, as it allows dynamic pressure to be the only remaining state in the reduced-order system of Eqns 5.53 and 5.57. The algorithm used to solve the resulting differential-algebraic system is shown in Figure 5.14.

The algorithm commences with the dynamic pressure at program initiation and the angle of attack theoretically necessary for flight at the guidance-specified flight path angle. (The real angle of attack at program initiation is not used since, for example, the vehicle may be experiencing transients due to a rapidly changing glideslope immediately after release in a drop-test scenario. Any errors between the actual and guidance-specified  $\alpha$  and  $\gamma$  values during the first few iteration steps are thus relegated to the flight control system to rectify, and therefore do not complicate the trajectory propagation process.) For the next integration step,  $h+\Delta h$ , where  $\Delta h$  is negative for decreasing altitude, we guess a value of  $\alpha$ . This value of  $\alpha$  allows two dynamic pressure estimates at altitude  $h+\Delta h$ . The first estimate,  $q_{\text{alg}}$ , is found from the algebraic constraint of Eqn 5.57. The second estimate,  $q_{\text{diff}}$ , uses the differential equation of Eqn 5.53 with a simple Euler

numerical integration technique. If the  $q$  estimates converge to a match, the value of  $\alpha$  satisfies the requirement to maintain the specified geometry, and ensures the governing equations are consistent. If not, the value of  $\alpha$  is varied by a secant root finding method until a valid solution occurs. After a successful match, the solution for  $(h+\Delta h)$  and  $q(h+\Delta h)$  is recorded and the algorithm repeats for subsequent altitude steps. Since  $q$  changes slowly over altitude, the altitude steps can be relatively large and the integration process accordingly rapid.

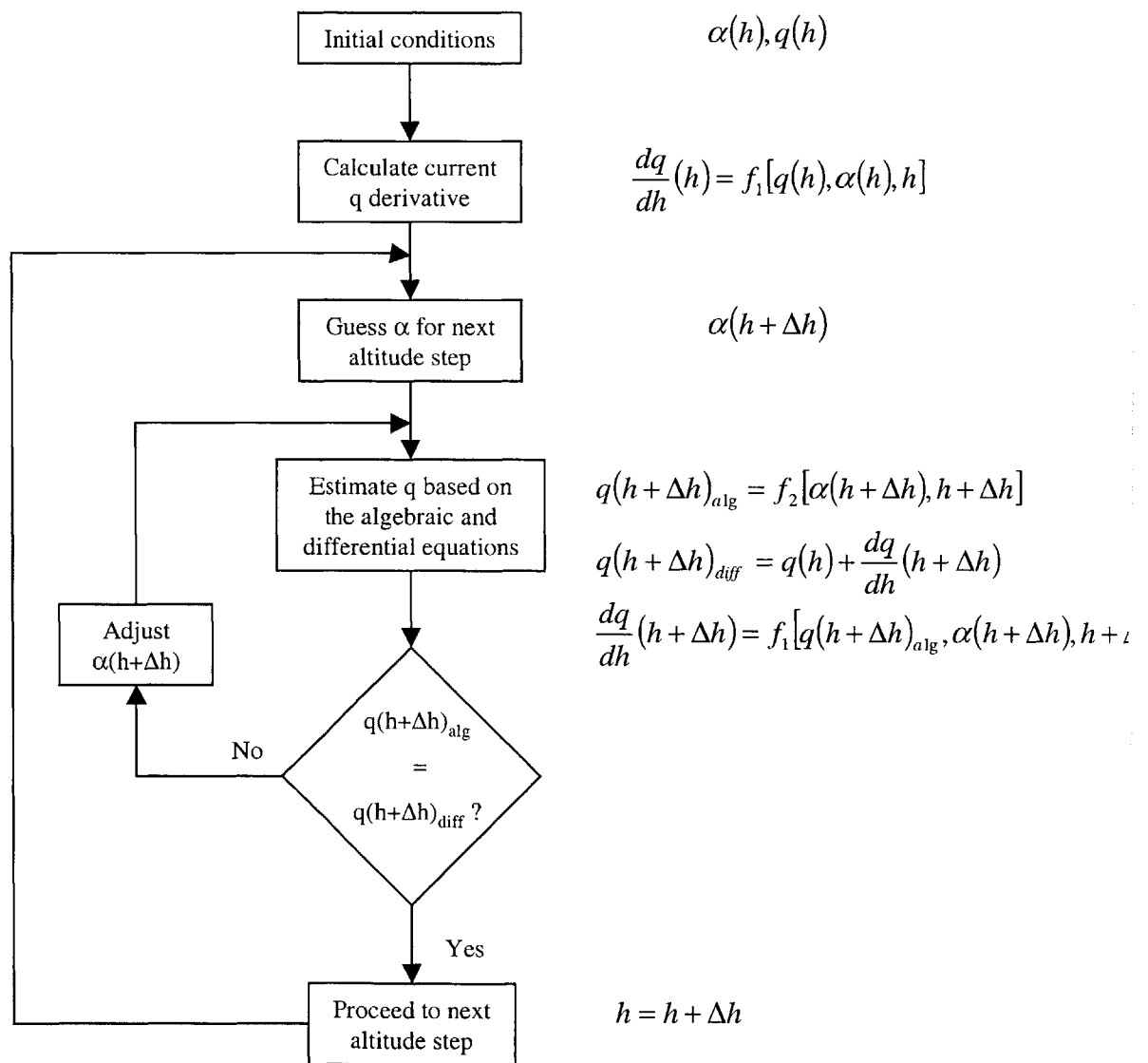


**Figure 5.14:** Propagation Algorithm [11]

## 5.4 Fast Tradespace Scanning

### 5.4.1 Rationale and Overview

Many combinations of initial and final states of the TPBVP can support multiple valid trajectories that satisfy all imposed constraints. To function effectively (and safely), the autonomous trajectory generator should be aware of its operating range, with boundaries and limits clearly defined. Early knowledge of the tradespace prevents computation resources from wasting precious time chasing unsatisfactory designs. In addition, such information can identify cases when no feasible solution is even possible.

This section begins with an explanation of the techniques used to generate tradespaces for trajectory parameters in the longitudinal and lateral domains. Next, an introduction to the concept of a desirability criterion describes the decision rationale for a trajectory choice within the defined tradespace. Finally, a description of the NZ tradespace for a specific gamma shows how the autonomous trajectory planner can provide consistent designs for flare maneuvers.

### 5.4.2 Tradespace Generation

For each TPBVP the onboard system quickly discovers a range of allowable trajectories. This correlates to finding the range of acceptable outer glideslopes for the longitudinal domain, and the range of allowable acquisition turn radii for the lateral domain. The tradespace definition process uses a family of constraints from both the imposed geometry and mandated dynamics to arrive at the feasible solution boundaries.

#### 5.4.2.1 Longitudinal Tradespace Constraints

As explained earlier, the outer glideslope ( $\gamma_1$ ) and the circular arc curvature radius ( $R$ ) remain the only two parameters needed to completely define a longitudinal trajectory at program initiation. One can find the extreme geometric boundaries of the allowable trajectory options by varying  $\gamma_1$  and treating  $R$  as a restriction from the vehicle's NZ

constraint. The graphical region bounded by the trajectory extremes represents the tradespace, as depicted in Figure 5.15 for an example flare case. Notice that the shaded region is bracketed by a steepest and shallowest trajectory, corresponding to the angle of the initial glideslope. Therefore, finding the tradespace amounts to discovering the boundaries of acceptable  $\gamma_1$ 's.  $R$  is incorporated in the calculation of the  $\gamma_1$  limits for tradespace definition and otherwise kept as a free parameter for trajectory designs within those limits. This latter condition is described later in subsection 5.4.4.

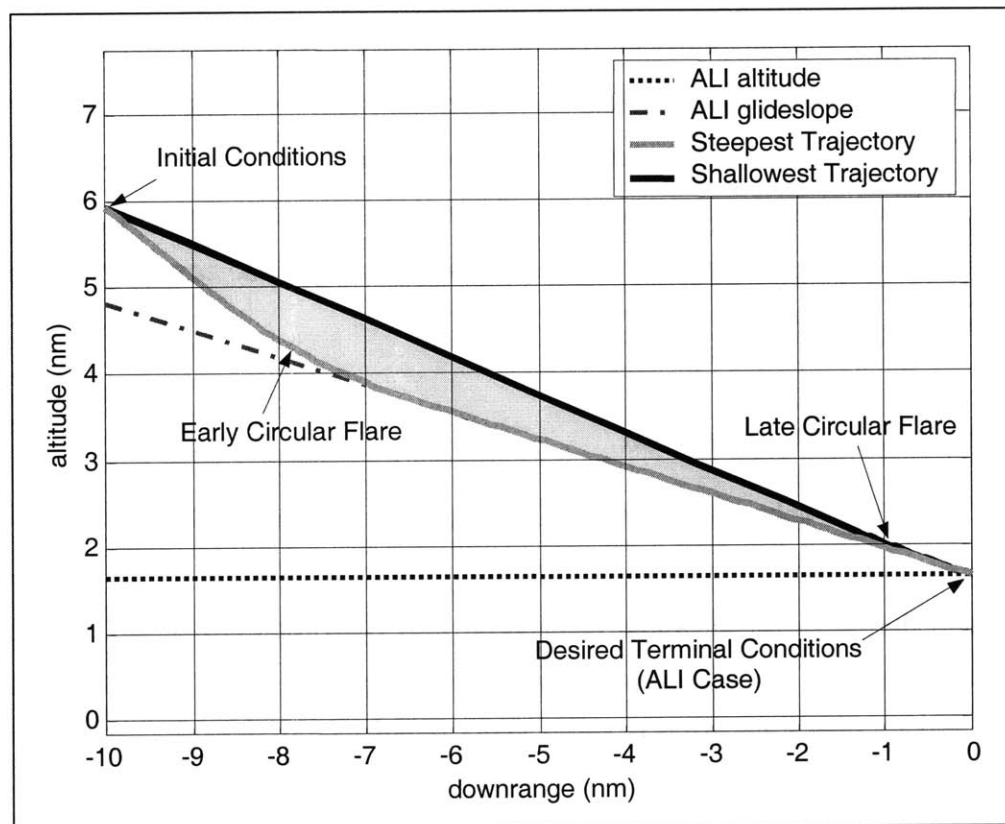


**Figure 5.15:** Longitudinal Tradespace

Identifying the solution tradespace requires finding the  $\gamma_1$  range subject to three criteria:

- **Geometric limits** – from the constrained nature of the available flare/anti-flare and linear path components of the non-compound curve trajectory construction
- **Max dive and max glide limits** – from dynamic pressure and range considerations
- **NZ limits** – from dynamic loadings

The tradespace is useful in that it defines the acceptable trajectory options over a widely varying set of initial conditions. This very breadth, though, may allow any one criterion to dominate the others as the driving constraint for a particular initial condition. Therefore, the tradespace represents the mutually satisfiable limit, with the result that the outer glideslopes from the most restrictive criteria will form the boundary.

#### 5.4.2.1.1 Geometric Limits

The geometric limits are the trajectory constraints stemming from the use of a non-compound-curve path construction. Figure 5.16 shows the geometric limits for an example anti-flare case, where the initial altitude lies below the inner glideslope. The steepest dive angle permitted is the linear glideslope connecting the coordinates of the initial and final conditions, which assumes an instantaneous transition to  $\gamma_2$  at the ALI. While physically possible, diving more steeply would violate the formal constraint by necessitating the use of compound curves, and may, if steeper than  $\gamma_2$ , uproot the commonsense guideline of monotonic convergence to the final glideslope condition. Since monotonic altitude decrease is desirable (if not practically mandated by the physics of low  $L/D$  vehicles), the shallowest dive angle must be at least below the horizontal.

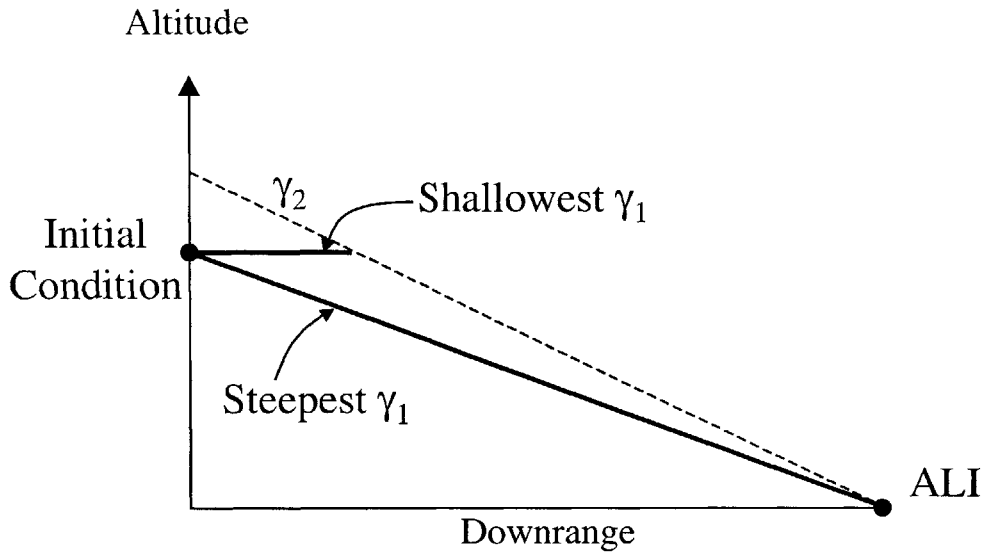


**Figure 5.16:** Geometric Limits for Anti-Flare Case

Figure 5.17 shows the geometric limits for an example flare case, where the initial altitude lies above the inner glideslope. The shallowest dive angle is the linear glideslope connecting the coordinates of the initial and final conditions. The steepest dive angle must be at least above the vertical, because while inverted flight may be amusing for airshow spectators, it is of no practical value for gliding reentry vehicles.

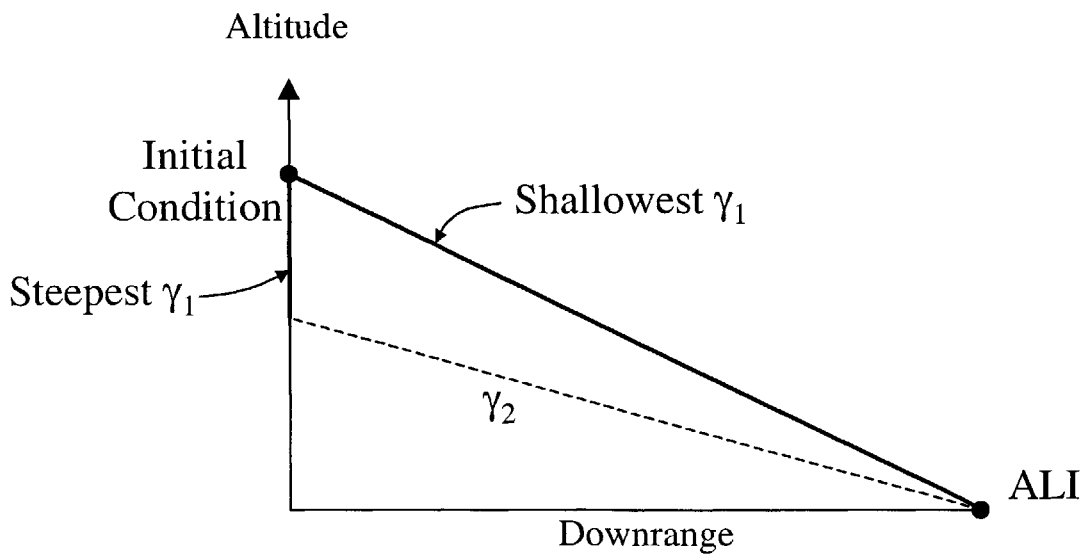


**Figure 5.17:** Geometric Limits for Flare Case

#### 5.4.2.1.2 Max Dive and Max Glide Limits

Unlike the geometric limits, the max dive and max glide limits are related to the vehicle dynamics. These limits serve not to maintain the non-compound-curve path structure, but rather to avoid glideslopes that threaten violating the boundaries of the energy corridor.

The max dive limit derives from the dynamic pressure constraint, which forms an upper boundary on allowable  $q$  values. For the X-34, the maximum dynamic pressure limit (conservative) is 500 psf. Maintaining a glideslope steeper than the max dive limit quickly forces the vehicle to exceed the 500 psf boundary. A key point is the necessity for a sustained glideslope to produce the eventual violation conditions. Momentary violations of the max dive limit, starting from appropriately low energy states, could conceivably be performed without undue consequence. However, with only one outer glideslope to select, short duration dips of extreme steepness followed by corrective pull-up maneuvers would almost always be irreconcilable with the non-compound-curve formulation, and furthermore would result in trajectory plans of questionable logic. Therefore, while not necessarily representing the steepest possible instantaneous dive, the max dive limit provides a conservative bound on the vehicle's outer glideslope that harmonizes effectively with the available geometric segments.

Calculation of the max dive limit clearly depends on the atmospheric density and vehicle energy states. The local limit may change, therefore, as the vehicle proceeds along its trajectory. For the purposes of onboard trajectory design, only the initial conditions matter in this calculation, serving merely to bound the tradespace. Nevertheless, at the time of writing, the procedure to calculate the max dive limit from an arbitrary condition was not available in a robust, near-instantaneous, autonomous form, and has actually evolved into an expansive research topic in its own right. Therefore, the onboard generator uses a pre-programmed value of  $\gamma = -39^\circ$ , derived off-line for this purpose, with subsequent improved functionality earmarked for modular insertion. This fixed max dive limit performs its role well, albeit more conservatively than theoretically necessary, because it represents the critical glideslope along the high-energy boundary at a typical initial condition altitude.

The max glide limit derives from range considerations, denoting the glideslope that maximizes the achievable downrange distance capability while flying at maximum lift-over-drag. In a manner akin to the relationship between the max dive limit and the upper bound of the energy corridor, the max glide limit represents a necessary flight condition along the lower bound. Flaring more shallowly than the max glide limit is unsustainable for any extended period of time.

Calculation of the max glide limit, like the max dive limit, also depends on atmospheric density and vehicle energy. Additionally, like the max dive, an acceptable onboard method to calculate this limit from an arbitrary condition was unavailable. The onboard generator uses a pre-programmed value of  $\gamma = -6.7^\circ$  derived from the critical glideslope along the low-energy boundary at an altitude representative of subsonic TAEM initiation. This value therefore serves as a conservative limit.

#### **5.4.2.1.3 NZ Limits**

The NZ limits are related to the vehicle dynamic loadings. The name stems from the acceleration component along the body z-axis. Longitudinal maneuvers like flares affect this acceleration; sharp flares produce higher loadings than more gradual ones.

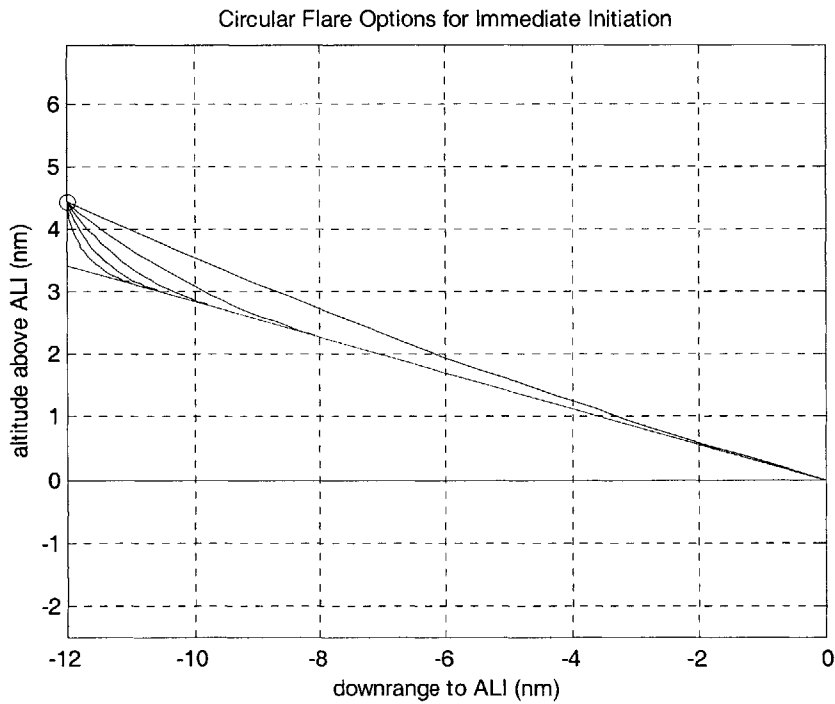
To avoid confusion, some nomenclature clarification may be useful. It is important to remember that NZ limits, like the geometric and max dive and glide limits, represent the extremes of  $\gamma_1$  according to the respective criteria. The maximum allowable NZ loading is an acceleration value described as the NZ bound.

The challenge for tradespace generation is to incorporate NZ constraints into the outer glideslope boundaries. Because each flare or anti-flare maneuver is restricted to follow a circular longitudinal geometry, as well as maintain instantaneous path continuity at the local glideslope intersections, the family of geometrically allowable curves is entirely defined by the arc radius  $R$  for a single  $\gamma_1$ . At this point it is useful to recall the locus line relationship introduced in Figures 5.6 and 5.8. Each of those flares or anti-flares has an



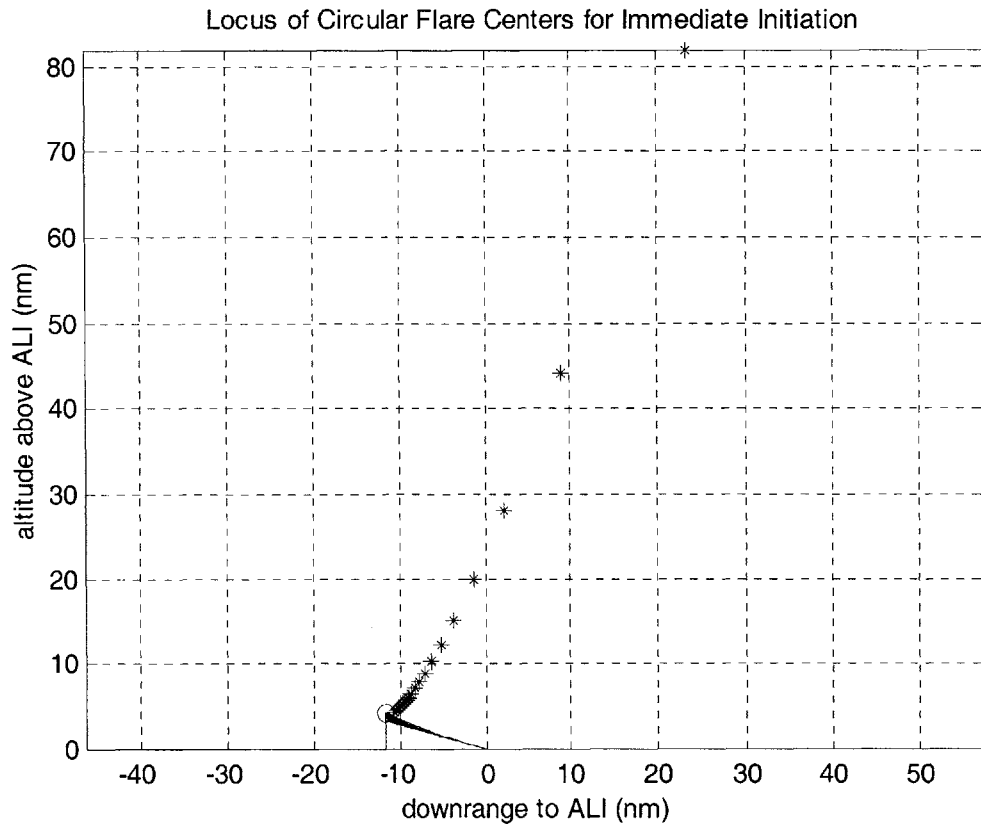
associated NZ loading. In almost all cases, larger R values correspond to lower NZ loadings. Therefore, flares or anti-flares started closer to the initial condition will cause less severe accelerations than those commenced later along an outer glideslope. The practical value of this observation is that flares or anti-flares that begin at the initial condition should have the least NZ loading of any alternative. Therefore, the outer glideslopes where immediate circular arcs produce the maximum allowable NZ loadings represent the NZ-influenced tradespace boundaries. Glideslopes outside these values would be clearly illegal, since the most benign flare or anti-flare possible would certainly exceed the NZ bound.

Figure 5.18 shows a family of circular arcs (flare example) that commence immediately at the initial condition. The choice of outer glideslope uniquely determines the geometry of each flare. As the candidate glideslopes become steeper, the required flares become more dynamically extreme. Glideslopes whose NZ loadings exceed the NZ bound are declared illegal.



**Figure 5.18: Immediate Arc Options**

Figure 5.19 provides another useful insight to the implications of a  $\gamma_1$  choice. It shows the family of arc centers for the immediate flares of Figure 5.18. Notice the nonlinear relationship between the arc radius and  $\gamma_1$ . The plot was generated by varying the  $\gamma_1$  angle in equal increments, yet the magnitude of R clearly does not modulate in a similar fashion. Indeed, the sensitivity of R to  $\gamma_1$  is not a constant; at one extreme (Figure 5.18's shallow glideslopes) small changes in  $\gamma_1$  can provoke very disparate flare radii, while the opposite is true on the other extreme (Figure 5.18's steeper glideslopes).



**Figure 5.19:** Locus of Circular Flare Centers for Immediate Arcs

The key to finding the NZ limits lies in two equations for the circular arc radius R. The first equation

$$R = \frac{V^2}{gNZ} \quad (5.58)$$

stems from the dynamics of radial acceleration along a circular path. The variables V, g, and NZ represent the velocity, gravity force, and NZ loading, respectively. [In some formulations, the NZ value is given as (NZ-1), to account for the preexisting gravity load. By contrast, the use of NZ alone describes the NZ component due to a given maneuver. For example, a NZ of zero (level flight) represents a maneuver with no acceleration consequence, with a fictional pilot only experiencing the common 1g load from gravity. A NZ of -1 represents a maneuver (anti-flare) that offsets the common gravity load, providing a fictional pilot the sensation of weightlessness. A NZ of +1 represents a maneuver (flare) where the pilot feels twice as heavy.] The second equation

$$R = \frac{H_{travel}}{\sin \gamma_1 \tan \Phi} \quad (5.59)$$

derives purely from the geometry. The familiar  $\gamma_1$  is the outer glideslope and  $\theta$  is the half-turn angle of Eqn 5.6. The variable  $H_{travel}$ , highlighted in Figure 5.20 for a flare case, represents the altitude difference between a flare initiation and the intercept point of the inner and outer glideslopes. In this particular example,  $H_{travel}$  corresponds to an immediate flare. Notice that any valid flare initiation must occur before the altitude of the glideslope intercept.

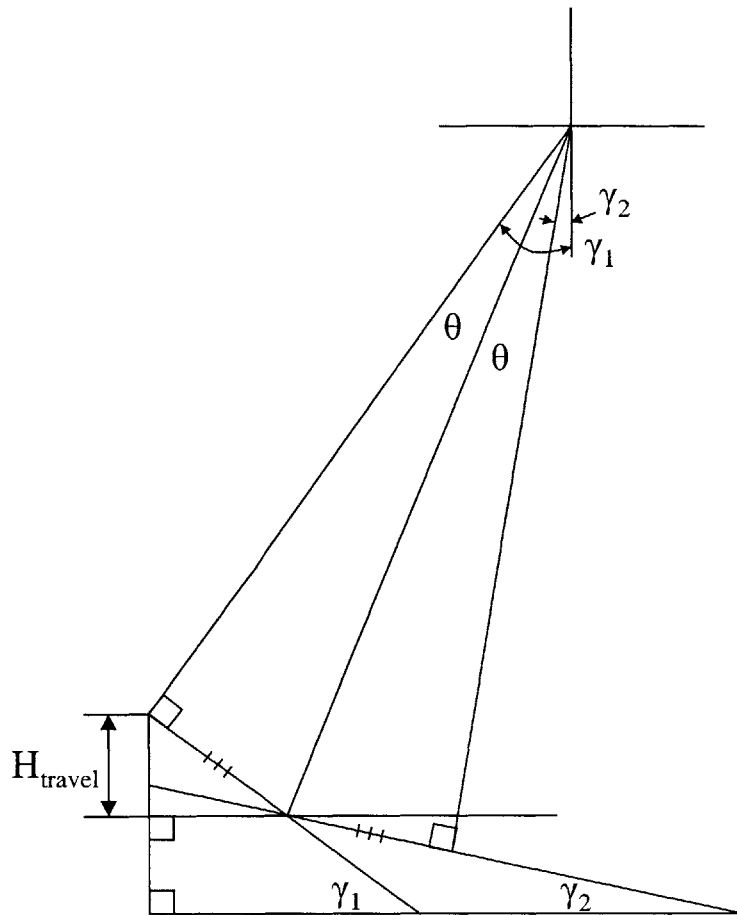


**Figure 5.20:**  $H_{\text{travel}}$  in Context

Since  $H_{\text{travel}}$  is trivially determined for an immediate flare/anti-flare, equation 5.59 can give  $R$  solely as a function of  $\gamma_1$ . Additionally for an immediate flare/anti-flare, since the velocity is also known at the initial condition and the gravity force can be assumed constant over the TAEM altitude regime, Equation 5.58 can define  $R$  solely as a function of the NZ value. Therefore, both equations can be used together to find the  $\gamma_1$ 's of the NZ limit when restricting the NZ value to the NZ bound.

To find the  $\gamma_1$ 's of the NZ limit, one might be tempted to set equations 5.58 and 5.59 equal to each other and merely solve for  $\gamma_1$  as a function of the NZ bound. However, both  $H_{\text{travel}}$  and  $\theta$  are functions of  $\gamma_1$ , and conspire to make such a straightforward approach transcendental. Thus, even though a solution may exist, there is no way to

solve for it in closed form. More importantly, not all NZ bounds have associated outer glideslopes. In fact, a single NZ bound may have two glideslopes that satisfy the equations (typically on the steep and shallow boundaries). Therefore, instead of solving for  $\gamma_1$  as a function of the NZ bound, the onboard trajectory generator works in reverse, solving for the NZ value that each  $\gamma_1$  uniquely defines, and then identifying the target  $\gamma_1$ 's as having NZ values that match the NZ bound.

The beauty of immediate flares/anti-flares is that valid NZ limits on  $\gamma_1$  can be calculated quickly, using only the readily available geometric and dynamic information at the initial condition. No computationally costly trajectory propagation steps are necessary. Unfortunately, some geometries forbid immediate arcs, requiring time spent on the outer glideslope before commencing the flare/anti-flare maneuver. Flying along the outer glideslope for any period of time usually changes the vehicle velocity, so that the initial velocity is no longer an accurate value to plug into Equation 5.58. For these cases, a limited trajectory propagation must be performed to obtain the velocity data.

In order to distinguish between cases permitting and prohibiting immediate flares/anti-flares, a systematic approach is needed. Figure 5.21 shows the geometric trends as  $\gamma_1$  is varied for an example anti-flare case. Each horizontal pair of cells, for which  $\gamma_1$  is held constant, highlights the boundary arc and some example middle arcs. Boundary arcs, which start immediately at the initial condition or terminate at the ALI final condition, always produce path geometries with less than three segments, and generate the maximum arc radii possible for a given  $\gamma_1$ . Middle arcs always form trajectories with exactly three segments and allow smaller arc radii than the boundary class. Starting from the uppermost cell pair, Figure 5.21 illustrates the effect of decreasing  $\gamma_1$ , making it more negative and steep. At a certain  $\gamma_1$ , known as the equivalency point, the boundary arc begins at the initial condition and ends at the final condition, and represents the maximum flare radius possible under any circumstance. Notice that the length of the outer glideslope to the  $\gamma_1/\gamma_2$  intercept is equivalent to that of the inner glideslope length after the intercept. Outer glideslopes past the equivalency point do not allow immediate

arcs, have boundary arcs that must end on the terminal condition, and require some trajectory propagation to generate the necessary velocity data for NZ limit calculations.

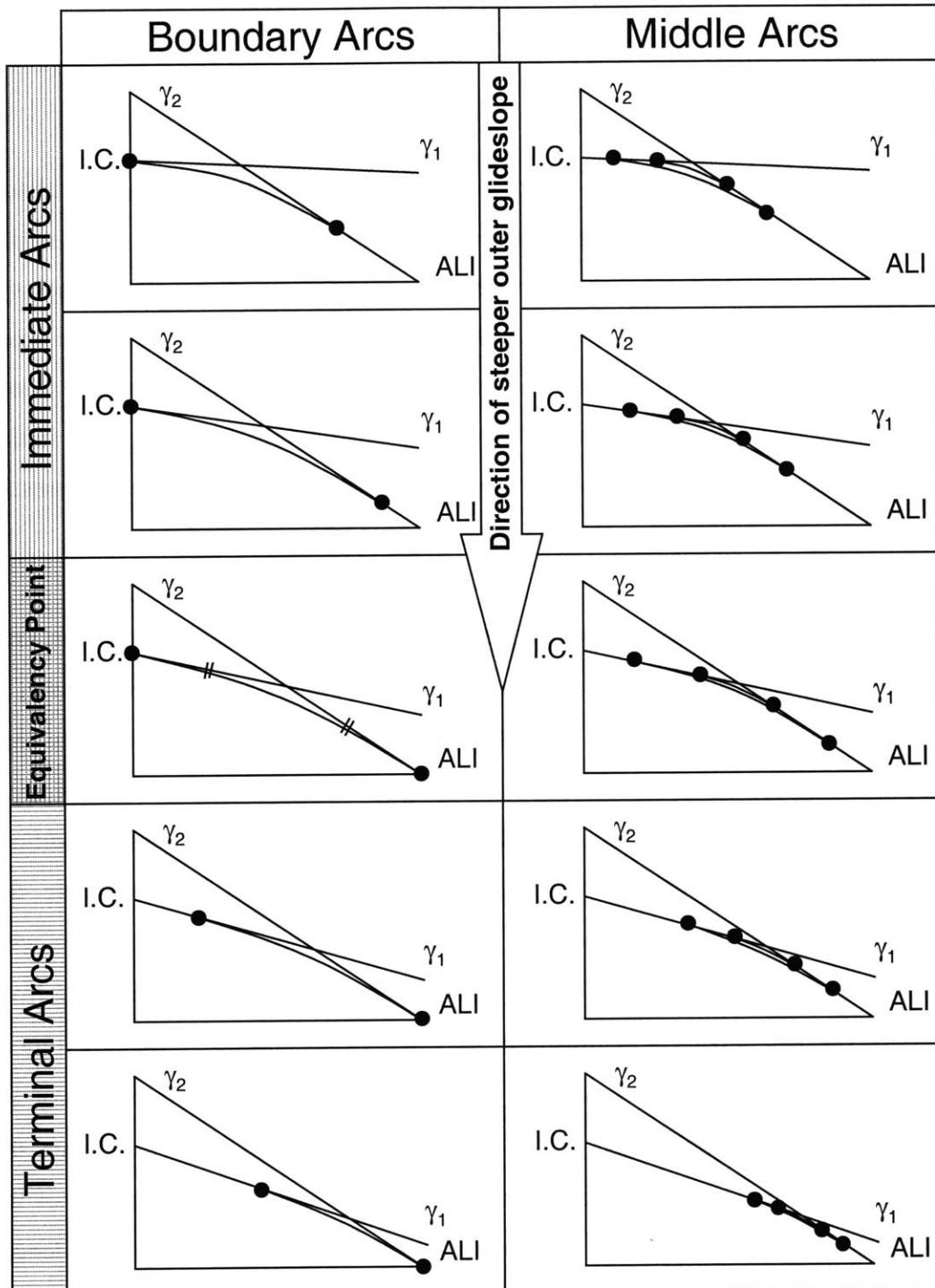


**Figure 5.21:** Geometric Arc Options vs. Outer Glideslope

The equivalency point designates a natural classification discriminator between candidate outer glideslopes. It should be noted that some geometries do not yield an equivalency point, allowing immediate arcs or terminal arcs but not both. Past the equivalency point, if it exists, terminal arcs serve the same role as immediate arcs because of their fixed “anchor” point. This provides a straightforward framework to calculate the arc radius. Table 5.4 summarizes the generalized components of Eqn 5.59 for every geometric possibility. For middle arcs,  $H_{\text{LOOP}}$  represents the altitude at maneuver start whereas  $H_{\text{END}}$  signifies the altitude at maneuver end.

**Table 5.4:** Generalized Components of Equation. 5.59

	<b>Boundary Arcs</b>	<b>Middle Arcs</b>
<b>Immediate Arcs</b> (before equivalency)	$H_{\text{travel}}=H_{\text{REF1}}-H_I$ denominator= $\sin\gamma_1\tan\Phi$	$H_{\text{travel}}=H_{\text{LOOP}}-H_I$ denominator= $\sin\gamma_1\tan\Phi$
<b>Terminal Arcs</b> (after equivalency)	$H_{\text{travel}}=H_I- H_{\text{ALI}}$ denominator= $\sin\gamma_2\tan\Phi$	$H_{\text{travel}}= H_I- H_{\text{END}}$ denominator= $\sin\gamma_2\tan\Phi$

As stated earlier, terminal arc conditions require some trajectory propagation to arrive at valid velocity values, and are therefore less computationally efficient than scenarios allowing immediate arcs. At this point it is important to remember that the challenge of finding the NZ limits lies in identifying the  $\gamma_i$  extremes. Thus, instead of propagating velocities along several candidate glideslopes, the maximum velocity along the steepest reasonable glideslope (using guidelines from the preceding geometric and max dive and glide limit calculations) serves as the entry into the dynamics of Eqn 5.58. Fortunately, this only requires a single trajectory propagation, performing the NZ limit-finding function in a fast and conservative manner.

Figure 5.22 shows the NZ data over a range of candidate glideslopes for an example anti-flare case. The lines of the immediate and terminal arcs represent the minimum absolute NZ magnitude possible for each  $\gamma_1$ . More severe NZ maneuvers can be performed using middle arcs. The allowable zone is restricted by the line of NZ bound, of magnitude 0.3 in this example. The sought-after  $\gamma_1$  limits are the intersections between the lines of

minimum NZ and NZ bound. Therefore, any choice of outer glideslope within those  $\gamma_1$  limits is guaranteed to support a dynamically valid trajectory. Note that the immediate and terminal arc lines do not exactly meet at the equivalency point. The small difference represents the largest possible error from the use of the conservative maximum velocity of the one-shot trajectory propagation for the terminal arc case.

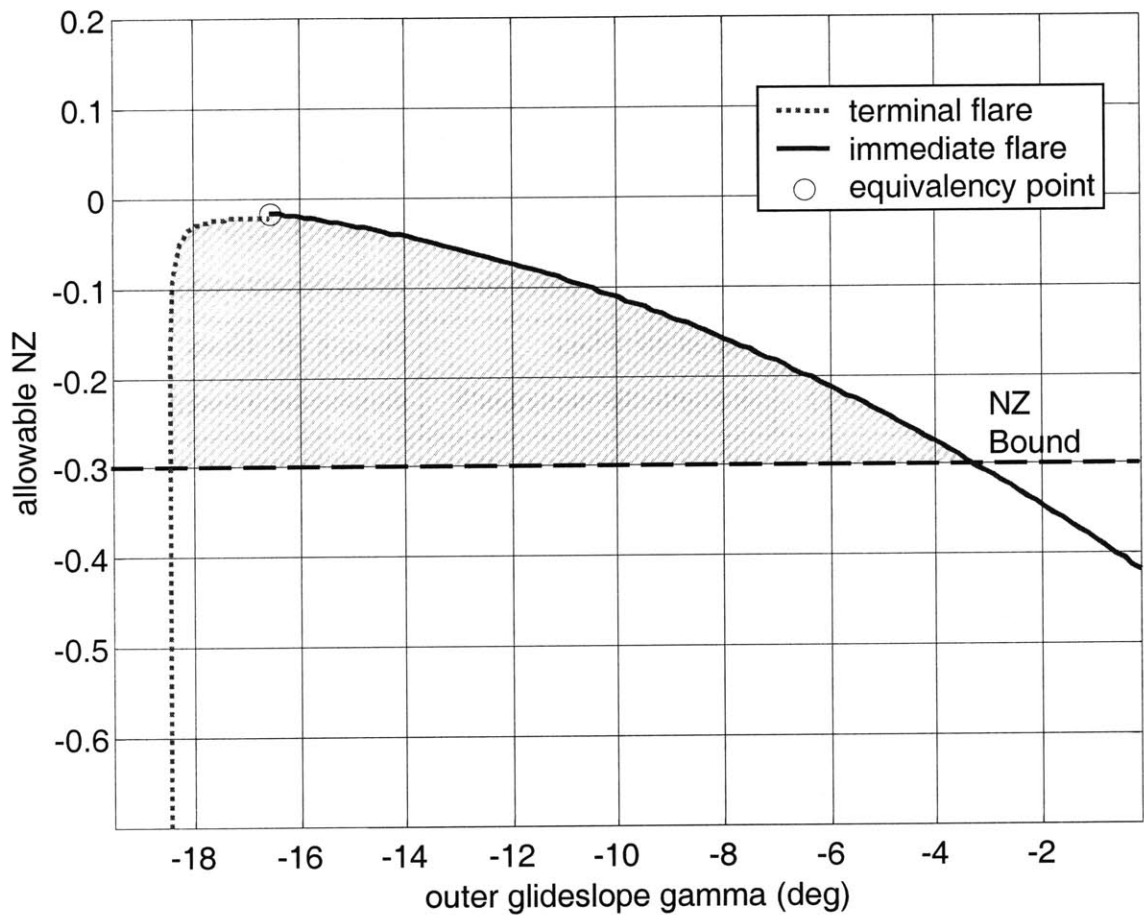


**Figure 5.22:** Allowable NZ Region vs. Outer Glideslope



### 5.4.2.2 Lateral Tradespace Constraints

In a role analogous to that performed by the outer glideslope for the longitudinal domain, the circular acquisition turn radius  $R_{AC}$  governs the lateral tradespace. The graphical region bounded by the trajectory extremes represents this tradespace, as depicted in Figure 5.23 for an example with significant initial heading misalignment. Notice that the shaded region is bracketed by trajectories resulting from the tightest and most gradual acquisition turns. Progress along each circular turn is continued until reaching a tangency with the HAC spiral. In fact, the choice of  $R_{AC}$  completely defines the lateral trajectory.

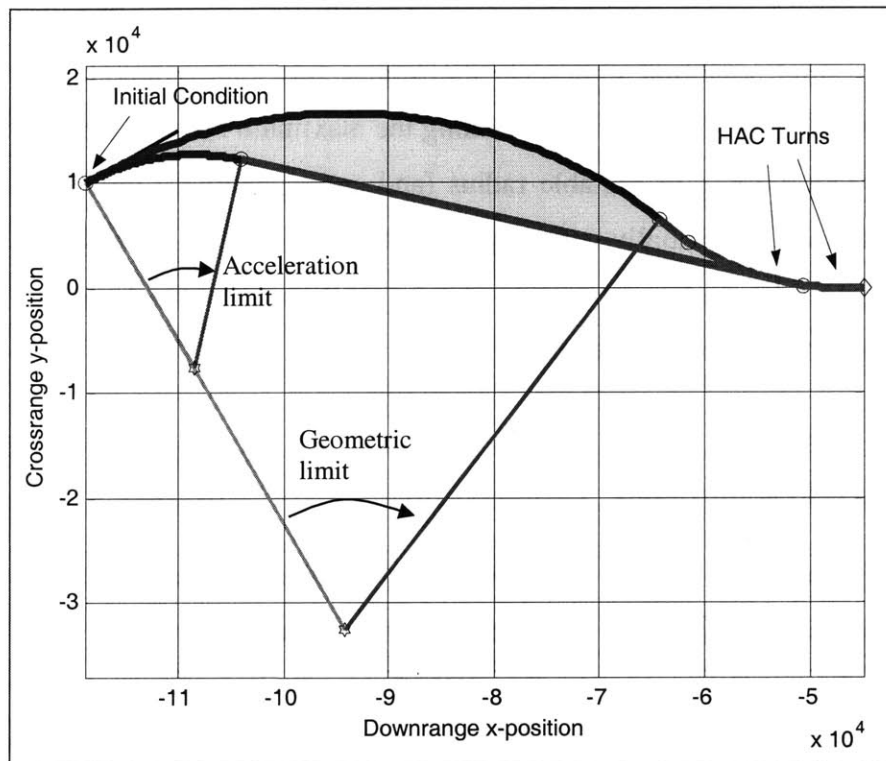


**Figure 5.23: Lateral Tradespace**

Identifying the solution tradespace requires finding the allowable acquisition turn radii range subject to two criteria:

- **Geometric limits** – from downrange constraints and restricted use of simple turn segments
- **Acceleration limits** – from dynamic loadings

Unlike the three categories of longitudinal limits, each of which determines an upper and lower  $\gamma_1$  extreme, the lateral limits only prescribe one radius. The geometric limit governs the largest turn radius while the acceleration limit sets the smallest.

#### **5.4.2.2.1 Geometric Limits**

The geometric limits are the trajectory constraints stemming from the use of simple lateral segments, and the decision to keep the HAC center at a fixed downrange location. Allowing flexibility in HAC placement would have contributed to a more expansive lateral tradespace, but was outside the scope of this thesis research. The geometric limit for a given initial condition represents the largest turn radius possible that does not violate the constraints. In many cases, finding the maximum  $R_{AC}$  involves solving for the condition where a circle of variable radius (and correspondingly variable radial center location) intersects tangentially with a spiral, whose own radius depends on the angle of tangential approach. Such a calculation is non-trivial, and the description of the method used for solution is deferred to Appendix B.

#### **5.4.2.2.2 Acceleration Limits**

The acceleration limits derive from the vehicle dynamic loadings, and mandate the minimum acquisition turn radii. Unlike the longitudinal NZ limit, which is determined solely via longitudinal criteria, the lateral acceleration limit incorporates both longitudinal and lateral maneuvers. This approach is necessary because flares or anti-flares are allowed to occur concurrently with acquisition turns. At first glance, it may appear that the longitudinal NZ limit receives preferential status since it is determined independently of lateral concerns, while the lateral acceleration harbors a provision for longitudinal effects. However, it must be remembered that the choice of acquisition turn influences the groundtrack distance, which obviously alters the longitudinal NZ determination. The full nature of this overarching coupling is discussed in Chapter 6. For this section, the notion of coupling applies only to addressing both acceleration components.

The orthogonal nature of maneuvers in both longitudinal and lateral planes suggests the use of an acceleration bookkeeping method that preserves these handy distinctions. The acceleration vector in the velocity frame was derived in Chapter 2 and is restated here as

$$\vec{a} = \dot{V}\hat{i}_v + V\dot{\chi}\cos\hat{\gamma}\hat{j}_v - V\dot{\gamma}\hat{k}_v \quad (5.60)$$

The acceleration vector that we are most concerned with is not the three-dimensional vector of Eqn 5.60, but rather the two-dimensional “lateral” vector always operating in a plane orthogonal to the velocity vector. This is convenient since we can calculate the total “lateral” resultant without regard to exact vehicle body position, which would involve body roll and alpha angles. The lateral acceleration resultant scalar is given by

$$a_{lat} = \sqrt{\left(\frac{V^2}{R}\right)^2 + \left(\frac{V_H^2}{R_{AC}}\right)^2} \quad (5.61)$$

where the quantities  $\frac{V^2}{R}$  and  $\frac{V_H^2}{R_{AC}}$  signify the longitudinal and lateral accelerations of their respective circular maneuvers. Here  $V_H$  is the horizontal velocity (since the acquisition turn is designed in the horizontal plane), and is related to the vehicle velocity via

$$V_H = V \cos \gamma \quad (5.62)$$

Adopting a maximum  $a_{lat}$ , substituting the NZ bound for the longitudinal component, and calculating  $V_H$  from the initial condition allows Equation 5.61 to be solved for  $R_{AC}$ . The result is a conservative bound on the minimum acquisition turn radius assuming a simultaneous flare or anti-flare maneuver of highest loading. Admittedly, the accuracy of this composite calculation usually decreases as the flare/anti-flare commences lower in altitude from the initial condition, as the initial velocity may no longer represent the

current velocity. However, a monotonic decreasing velocity profile (typical of an orbital entry scenario) merely adds to the conservatism.

Adhering to a circular acquisition turn means that while the acceleration restrictions can be met at the initial condition or at the point of flare/anti-flare initiation, there will be subtle variations during the turn, partially due to changes in velocity. An acquisition turn with constant acceleration over a non-constant velocity profile is theoretically possible, but would require a non-circular layout, which clearly violates the geometric framework adopted. The same observation holds for the longitudinal flares and anti-flares as well.

### **5.4.3 Desirability Criterion**

Performing the fast tradespace scan will quickly determine if any trajectory solutions exist. With sufficiently severe initial states, the limits may dictate no suitable path. In such a case, an abort planner may relax the limits or select an alternate set of terminal conditions (i.e. alternate runway) that can provide a solution to the newly revised TBVP. This is the definition of an inherent abort capability, and represents a significant improvement over current Shuttle guidance.

When a range of allowable trajectories exist within a given solution tradespace, the question becomes which should be chosen. The onboard system automatically selects the actual trajectory based on a pre-programmed desirability criterion, which is variable to meet the needs of different user communities. For example, early drop tests could place a premium on trajectories benign to potential control response uncertainties, whereas trajectories meant for use with fragile payloads might emphasize low total dynamic loadings. This feature is especially useful if the vehicle can be crewed. For the purposes of the research performed for this thesis, a desirability criterion optimizing robustness was chosen.

#### 5.4.4 NZ Tradespace for Specific Gamma

After the fast tradespace scan establishes a range of trajectory options, the desirability criterion chooses the actual outer glideslope. Although the limit finding process guarantees this specific  $\gamma_1$  to provide at least one valid trajectory, the undetermined value of the circular arc radius  $R$  at this stage denies complete geometric knowledge of the entire trajectory. The selection of  $R$  follows many of the same processes as the NZ limit finding method.

Unlike the immediate and terminal arcs, that either start or end at well-defined, fixed geometric locations, middle arcs can commence in many places along the outer glideslope. Each location along the outer glideslope has an uniquely associated potential flare/anti-flare geometry, although certain restricted zones forbidding arc initiation may apply. In addition, each location has a velocity, calculated through a simple trajectory propagation along the glideslope. Therefore, equations 5.58 and 5.59 can be solved to discover the theoretical NZ loading that would occur at the beginning of each possible flare/anti-flare initiation point for a chosen  $\gamma_1$ . In this manner, a desired NZ loading will determine  $R$  and complete the trajectory definition.

Figures 5.24 and 5.25 show the NZ tradespace for two outer glideslopes, which represent the boundaries of allowable  $\gamma_1$  for the example considered. In Figure 5.24, notice the allowable arc initiation zone ranges from the initial altitude of 31,000 ft to just below 30,000 ft. The desired NZ condition, circled, occurs partway through this altitude range, requiring a middle arc. Figure 5.25 shows the tradespace for the steepest  $\gamma_1$ . Note the lower altitude range of the allowable arc initiation zone, as well as the local trend of increasing dynamic pressure with dropping altitude. In this case, the desired NZ condition occurs near the start of the allowable zone.

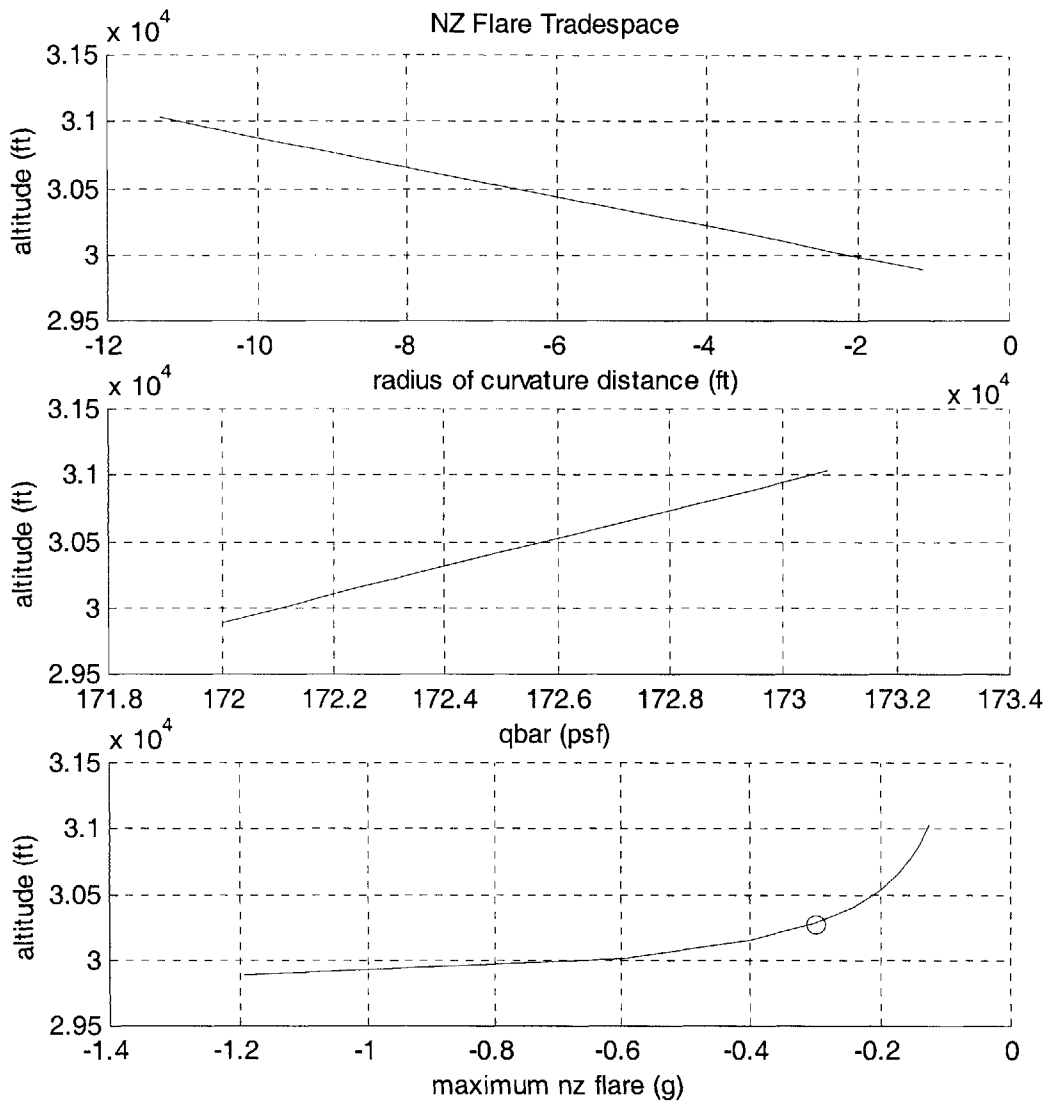


**Figure 5.24:** NZ Tradespace for Max Glide

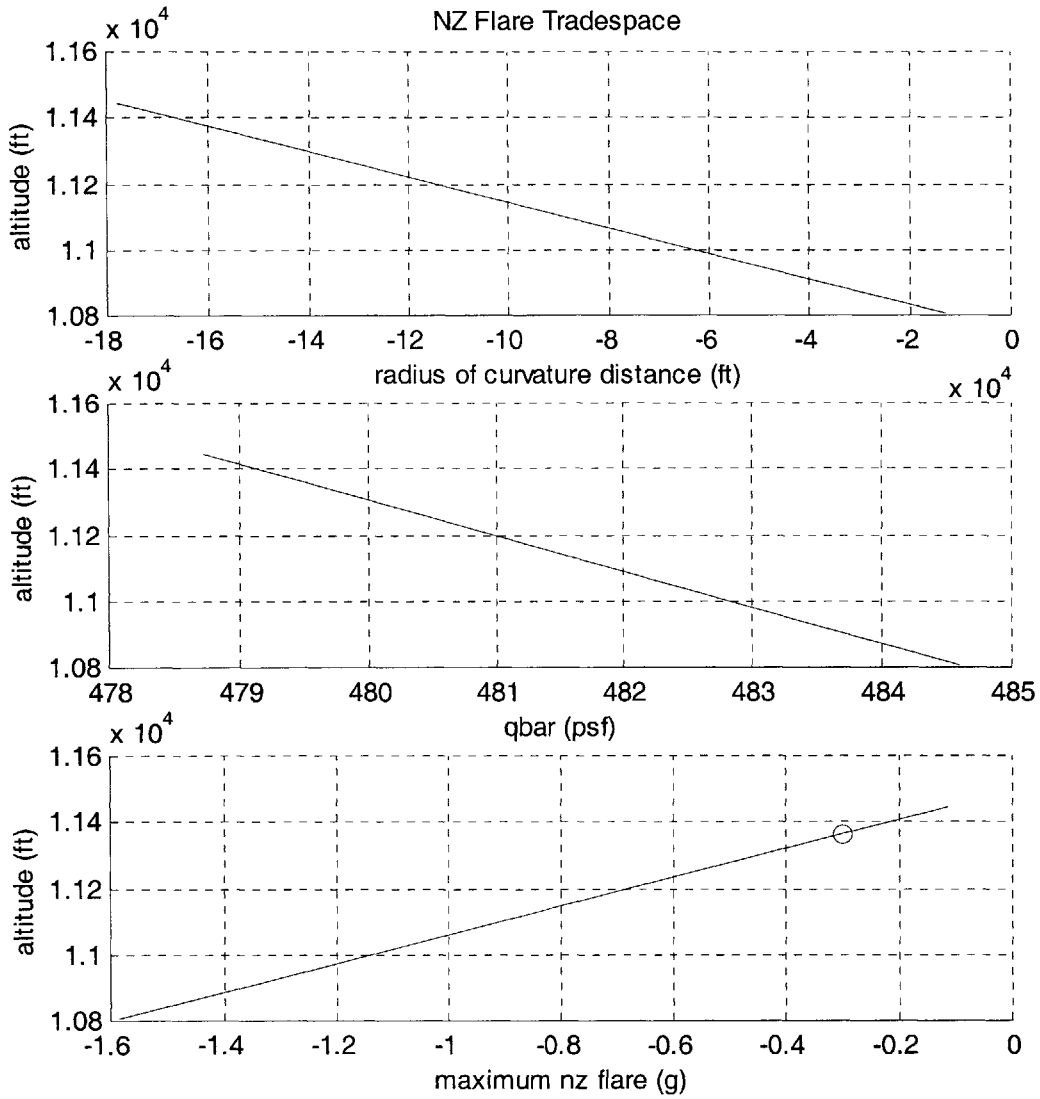


**Figure 5.25:** NZ Tradespace for Max Dive

## **5.5 Adaptive Center-of-Capability Reference**

### **5.5.1 Rationale and Overview**

While generation of the tradespace places some necessary boundaries on the available trajectory options, the primary onboard guidance task resides in the selection of a trajectory that satisfies the terminal conditions of the ALI. The requirements for the selection process mandate quickness, accuracy, and usefulness over a broad range of initial conditions. When several viable trajectories satisfy all constraints, it is desirable that the autonomous algorithms choose the option of maximum robustness.

This section details the rationale and technical particulars of a successful autonomous method to guide the trajectory design process. A survey of candidate control parameters justifies the adoption of the speedbrake as the most effective and elegant means to shape an energy profile. Next, development of a center-of-capability standard provides a quantitative definition of robustness that can be used to discriminate among competing trajectories. Finally, an adaptive reference is discovered that represents ideal vehicle energy conditions along a trajectory. This reference serves as the enabling ingredient for the optimized trajectory computation of section 5.6.

### **5.5.2 Control Parameter Survey**

Correctly choosing an appropriate control parameter upon which to base the trajectory design process in an effective yet efficient manner is paramount to the onboard generation process. Ideally, this allows the formulation of the most robust trajectory within the limits defined. With aspects of the geometric design partially constrained by the initial and final points, as well as adherence to the limited geometry segment options and defined tradespace, three candidates emerged for the role of chief design variable: NZ loading, outer glideslope, and speedbrake. The ability of each variable to individually produce the desired dynamic pressure at the terminal condition (the other terminal conditions of position, orientation, loading, and continuity being already satisfied by the existing geometric framework and tradespace) became a key determinant.



### 5.5.2.1 NZ Control

Least effective in altering the trajectory dynamics were variations in the NZ loading. Figure 5.26 shows the geometry of an example anti-flare case where the NZ load is varied while the outer glideslope and speedbrake are held constant. Notice how the highest NZ load allows a longer duration on the initial glideslope.

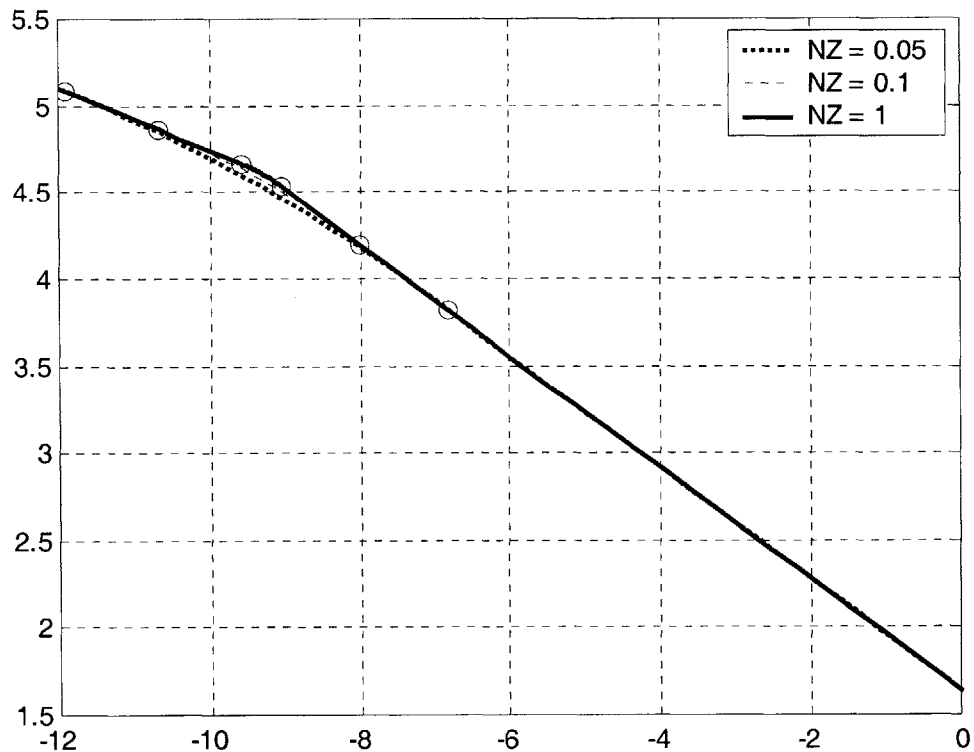


**Figure 5.26:** Geometric Effect of NZ Variations

Figure 5.27 illustrates the dynamic pressure profiles of these geometries. Most importantly, each trajectory converges to nearly exactly the same  $q$  at the ALI, regardless of NZ load. Early  $q$  differences caused by the staggered departure from the outer glideslope are dampened over the relatively long duration spent on the common inner glideslope. The instantaneous vehicle glidepath angles are the factors causing the early  $q$  differences, with steeper conditions imparting larger momentary kinetic increases. Since

altering the NZ load is an inefficient method of generating significantly different glidepath geometries, it fails as a meaningful trajectory design control parameter.

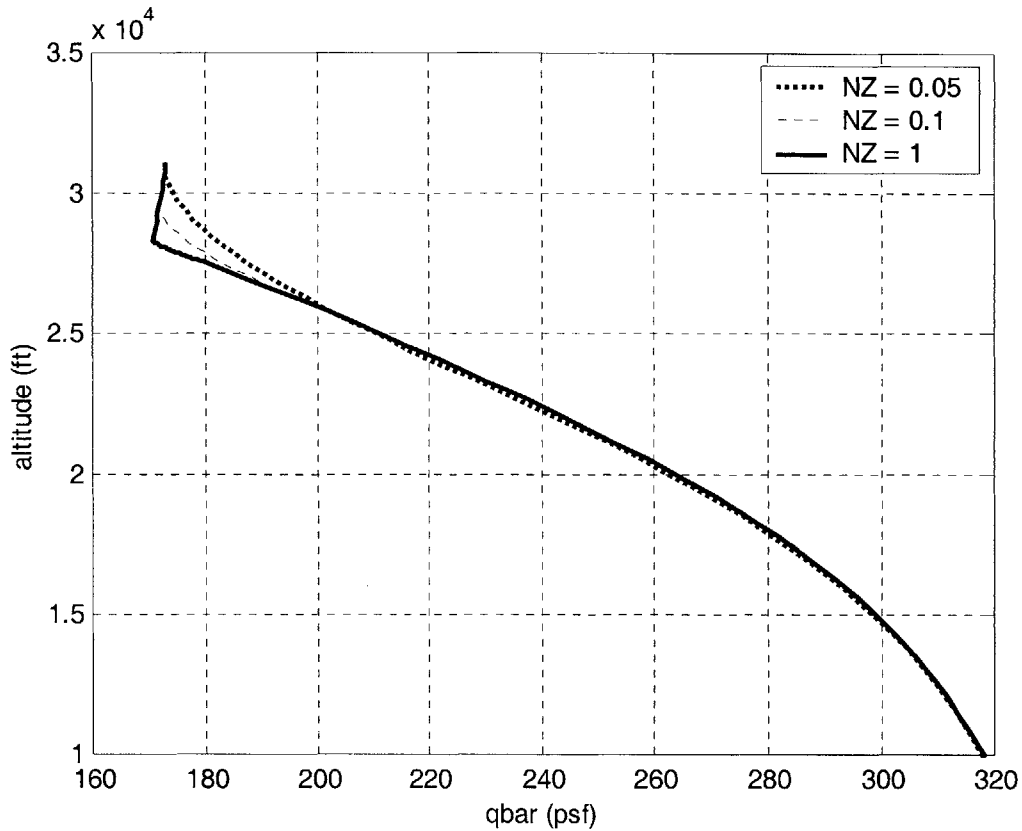


**Figure 5.27:** Dynamic Pressure Effect of NZ Variations

### 5.5.2.2 Outer Glideslope Control

Variations in the outer glideslope angle have a noticeable effect, but are plagued by a nonlinear correlation. Figure 5.28 shows the geometry of an example anti-flare case where the outer glideslope is varied in equal increments while the NZ load and speedbrake are held constant. Notice how the shallower gammas allow earlier anti-flares that enable earlier transitions to the inner glideslope. The steepest gamma forces an anti-flare at the last possible opportunity.

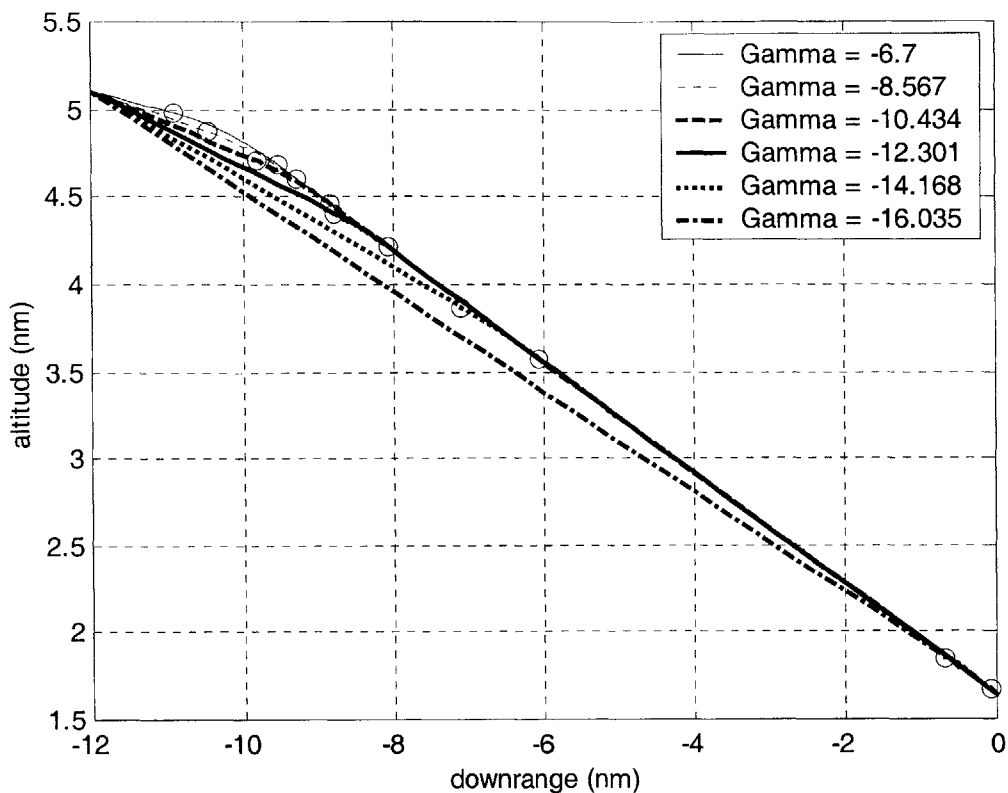


**Figure 5.28:** Geometric Effect of Outer Glideslope Variations

Figure 5.29 shows the dynamic consequence of the outer glideslope choice. The most shallow  $\gamma_1$  initially loses dynamic pressure quickly but increases thereafter following the early transition to the steeper  $\gamma_2$ . The steepest  $\gamma_1$  always experiences an increasing  $q$ , but at a lesser rate than available on the inner glideslope, to which it transitions only at the last moment. Differences in the final  $q$  are obviously more severe than the NZ load variation example of Figures 5.26 and 5.27, simply because altering the glideslope is a more efficient method of generating significantly dissimilar geometries. The important observation, however, lies not in the maximum terminal  $q$  difference between  $\gamma_1$  extremes (which can be larger or smaller for examples using different initial conditions), but rather their distribution. Figure 5.30 offers a closer view of the dynamic pressure behavior at the lower altitudes. The clearly nonlinear  $q$  distribution renders  $\gamma_1$  undesirable as a trajectory control parameter.

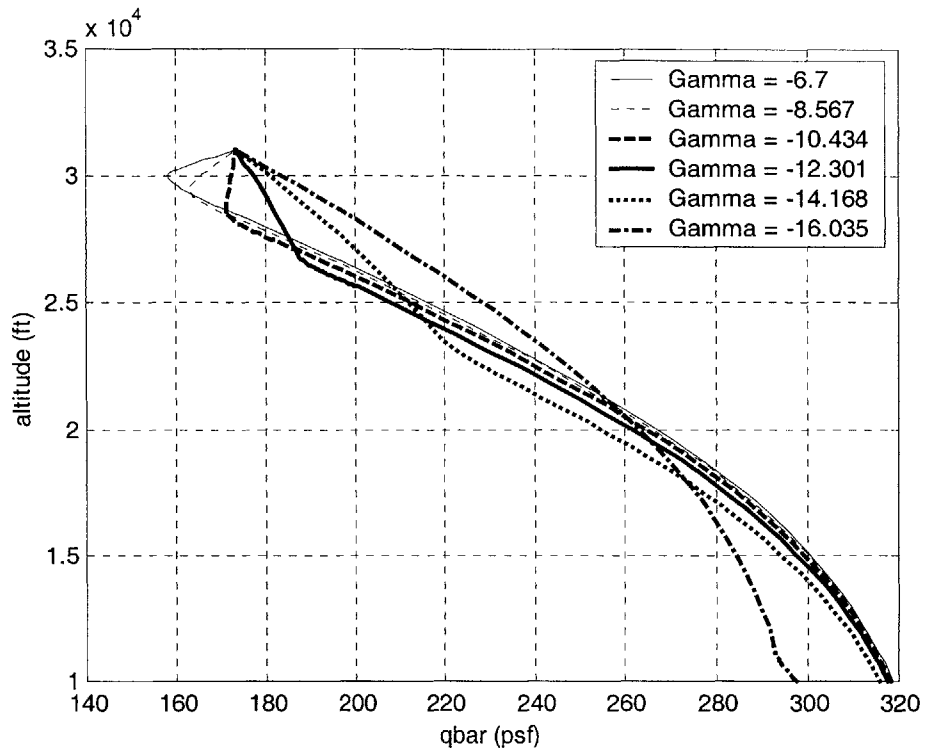


**Figure 5.29:** Dynamic Pressure Effect of Outer Glideslope Variation

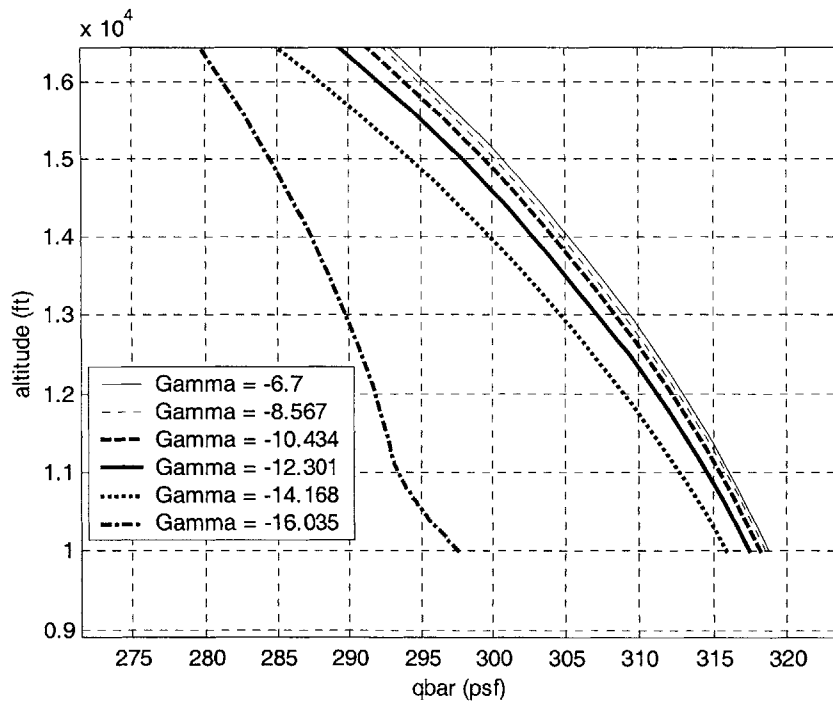


**Figure 5.30:** Detail of Dynamic Pressure Effect of Outer Glideslope Variations

### 5.5.2.3 Speedbrake Control

Variations in the speedbrake position are most effective in producing the desired terminal conditions over all geometric trajectory constructions, and have the added benefit of a relatively linear correlation. Figure 5.31 shows the geometry of an example anti-flare case where the speedbrake is varied in equal increments over a part of its capability (0 to 60 degrees) while the NZ load and outer glideslope are held constant. Any variation in trajectory geometry stems solely from the different velocities used in the anti-flare calculation, the effect of which is clearly insignificant.

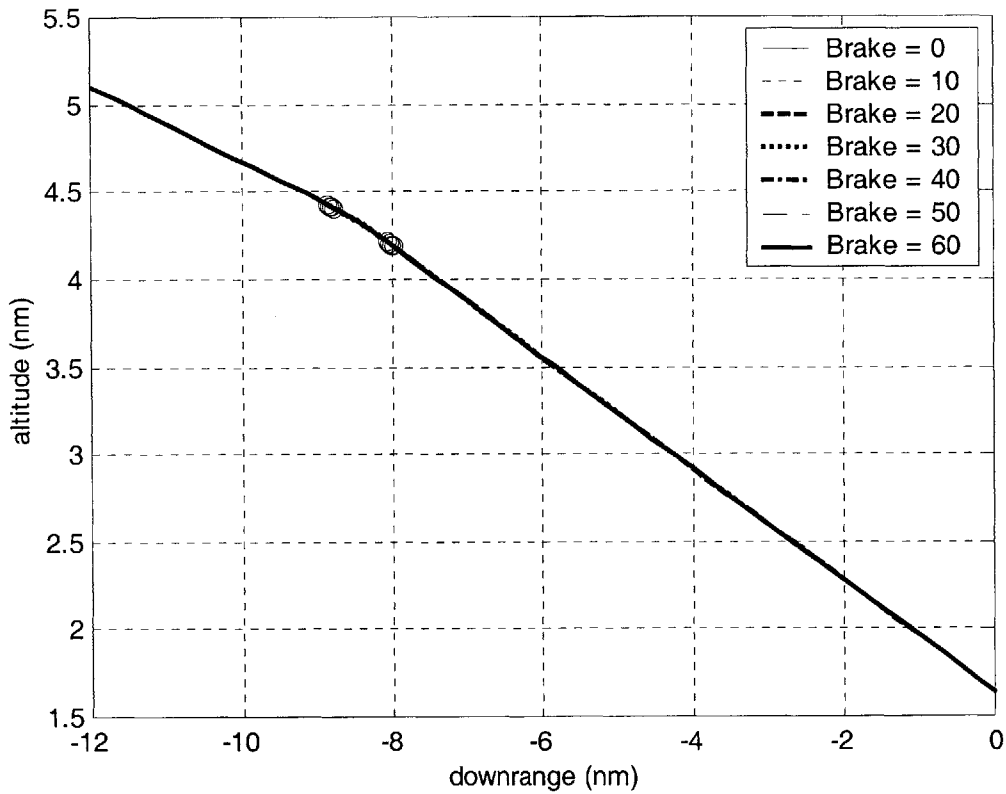


**Figure 5.31:** Geometric Effect of Speedbrake Variations

Figure 5.32 presents the dynamic consequence of speedbrake position. Not only does the speedbrake wield a dramatic influence over the terminal  $q$ , it operates in a conveniently

linear fashion. While not obviously displayed in the graph, this linearity also holds over very small variations in speedbrake position.

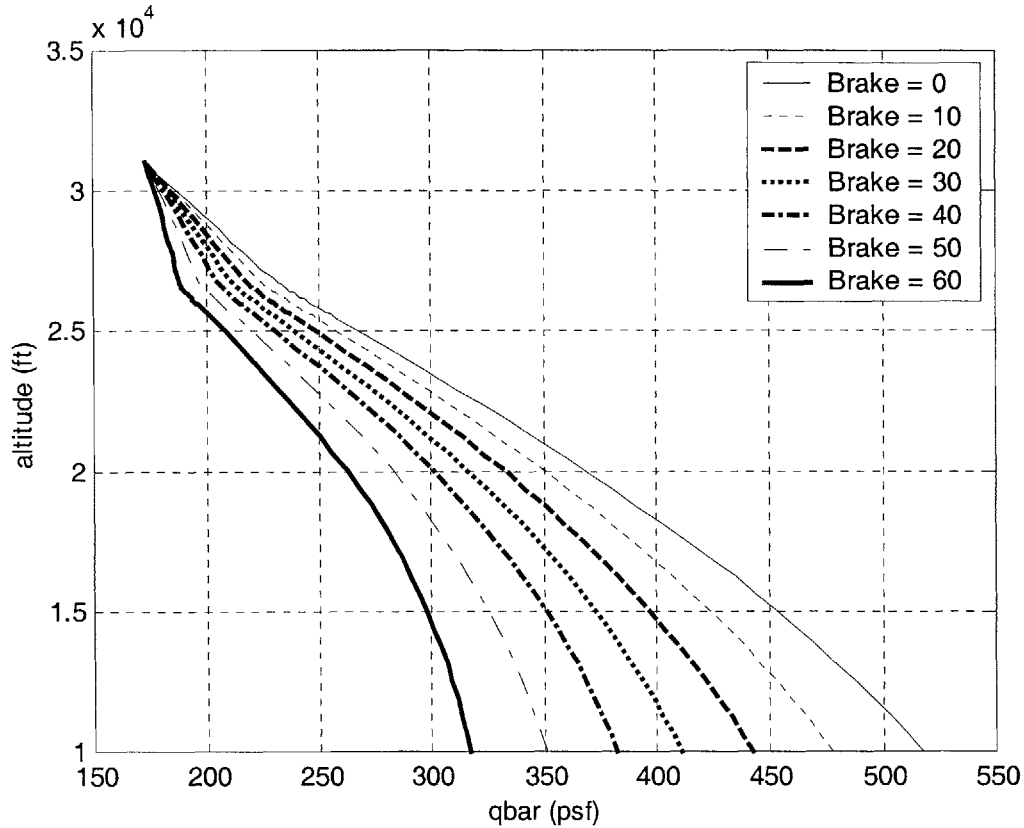


**Figure 5.32:** Dynamic Pressure Effect of Speedbrake Variation

The elegance, from a design standpoint, of choosing the speedbrake position as the trajectory control parameter is that it helps separate trajectory performance from trajectory shape. Of course, the trajectory shape is already confined within the tradespace, but geometric variations within that tradespace can be safely relegated to a pre-programmed desirability criterion, while variations in the speedbrake could satisfy the terminal conditions, and, as shall be explained next, the means of providing maximum robustness.

With a completely specified flight geometry that satisfies the imposed constraints, the speedbrake position is used to control the dynamic pressure profile of the trajectory.

Reaching the desired terminal conditions at the end of the trajectory is usually not difficult. A variety of factors contribute to this, one of which is the ALI glideslope segment at the end of the trajectory, which, being close to the equilibrium glideslope, has a natural tendency to minimize velocity errors. Another factor is that the X-34 speedbrake is very capable in the subsonic TAEM flight regime. Because of these benefits, multiple satisfactory solutions can be found for a majority of test cases. The optimum solution would be the speedbrake profile that maintains the dynamic pressure in the most robust possible manner.

### 5.5.3 Center of Capability

In an energy management problem, with no opportunities for thrust, a convenient measure of robustness is the center-of-capability. Figure 5.33 illustrates the concept. In this condition, the maximum increase of the change in dynamic pressure with respect to time ( $dq/dt$ ) equals the maximum decrease. It represents the measure of departure potential from the current dynamic pressure, and is very important in handling atmospheric disturbances. The challenge for an autonomous trajectory generator is how to modulate the speedbrake to attain the center-of-capability trajectory.

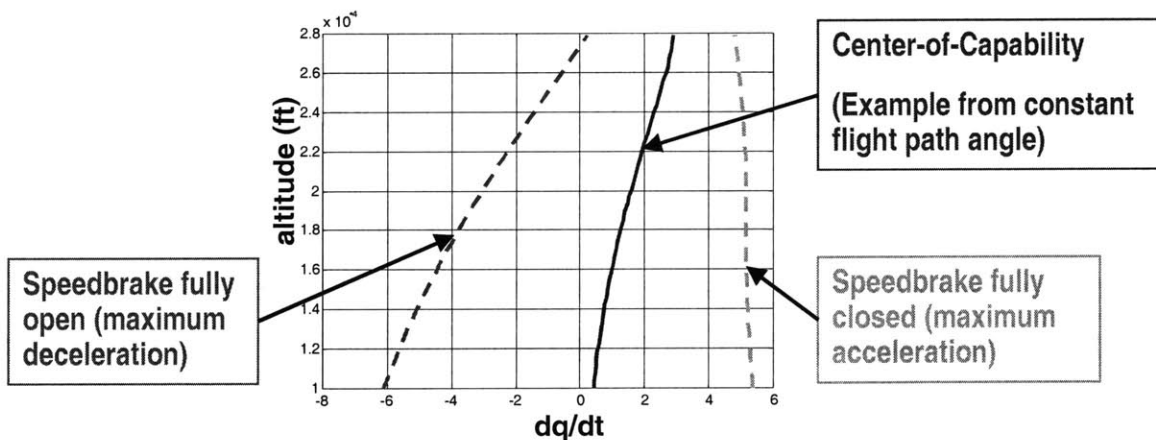


Figure 5.33: Center-of-Capability as Measure of Robustness

#### **5.5.4 Adaptive Center of Capability Reference**

An intelligent guidance system requires the ability to make decisions that alter the performance of the vehicle to reach desired states. Because of the expansive capability of the speedbrake, merely satisfying the mandatory terminal conditions is trivial from a wide variety of initial conditions. The onboard guidance can demonstrate performance beyond the minimum requisite functionality by aiming for optimal states throughout the trajectory. Therefore, the vehicle should seek a center-of-capability condition for optimal robustness. The question becomes: at what dynamic pressures does this preferred condition exist along a given trajectory? Such knowledge effectively provides “guidance for the guidance system” by furnishing an accurate decision criterion for energy modulation via the speedbrake. This standard is called an energy reference.

At this point, an astute reader may question the relative novelty of using an energy reference since practically all entry guidance schemes utilize them. However, these commonly employed references are pre-loaded, and therefore unresponsive to off-nominal conditions. Since the center-of-capability condition for a trajectory is very dependent on the path geometry, pre-loaded references are unable to calculate the most robust condition when geometries vary from some hypothesized norm. The onboard guidance system generates an energy reference that is adaptive in that it emulates the geometry of the chosen trajectory. This adaptive center-of-capability reference trajectory represents the ideal energy state of the vehicle along its actual flight path.

The reference is calculated “upwards” or “backwards” from the terminal state (ALI) along the emulated geometry of the chosen trajectory. This technique provides a continual and infallible reference for the speedbrake position logic with a minimum of computational effort, requiring only one trajectory propagation in the reverse direction. Each integration step along the propagation calculates the most robust energy condition referenced from the ideal condition of the preceding step.



An important distinction should be noted between an emulated and exact trajectory. An adaptive reference emulates the longitudinal geometry of a chosen trajectory because accurate values for the flare or anti-flare radii are unavailable at the time of its calculation. The reason is that reference-calibrated speedbrake modulations after the initial condition will necessarily alter the velocity profile along the outer glideslope, which will affect the NZ tradespace for a choice of arc radius. Therefore, the adaptive reference generator only uses geometric information concerning the two glideslopes,  $\gamma_1$  and  $\gamma_2$ . Propagating backwards, starting along  $\gamma_2$  from the ALI, the adaptive reference generator creates its own (ideal value) velocity profile, and picks an appropriate transition via circular arc to the outer glideslope using an NZ tradespace process nearly identical to that described in section 5.4.4. The only differences are the reverse order and the use of a slightly modified NZ bound, since the NZ load at the low-altitude terminus of the arc will differ from that at the high-altitude one. The arc radius generated by the adaptive reference process closely matches the actual value, so the emulated geometry is nearly exact. In fact, a sensitivity study that varied initial condition downrange from 11.5 to 7 nm and the NZ bound from 0.38 to 0.02 found that the differences between emulated and actual arc radii were less than 0.25%.

Figure 5.34 illustrates the use of a wings-level adaptive reference for both a flare and an anti-flare case, and compares each against an unadaptive reference that preserves a constant inner glideslope. In the flare case, (reckoning “backwards” from the terminal state) the adaptive reference initially matches the constant glideslope reference correlating to the final glideslope, but departs at 3.5 nm altitude when the circular flare starts the bend to the initial glideslope. A significant discrepancy arises between the two references, with only the adaptive reference incorporating the effect of the steeper initial glideslope. The smaller  $q$  values of the adaptive reference account for the potential of the vehicle to gain energy more rapidly while on a steeper trajectory. In the anti-flare case, the discrepancy between the adaptive and the constant glideslope reference is again apparent, but this time the adaptive reference has larger  $q$  values in the high altitude region. This accounts for the potential of the vehicle to lose energy rapidly when on a relatively shallow trajectory. Note that the reference trajectories can be computed

beyond the drop altitude of the vehicle. Also note that the difference in the shape of the constant glideslope reference (common to both flare and anti-flare cases) is due to the difference in scale of the horizontal axes.

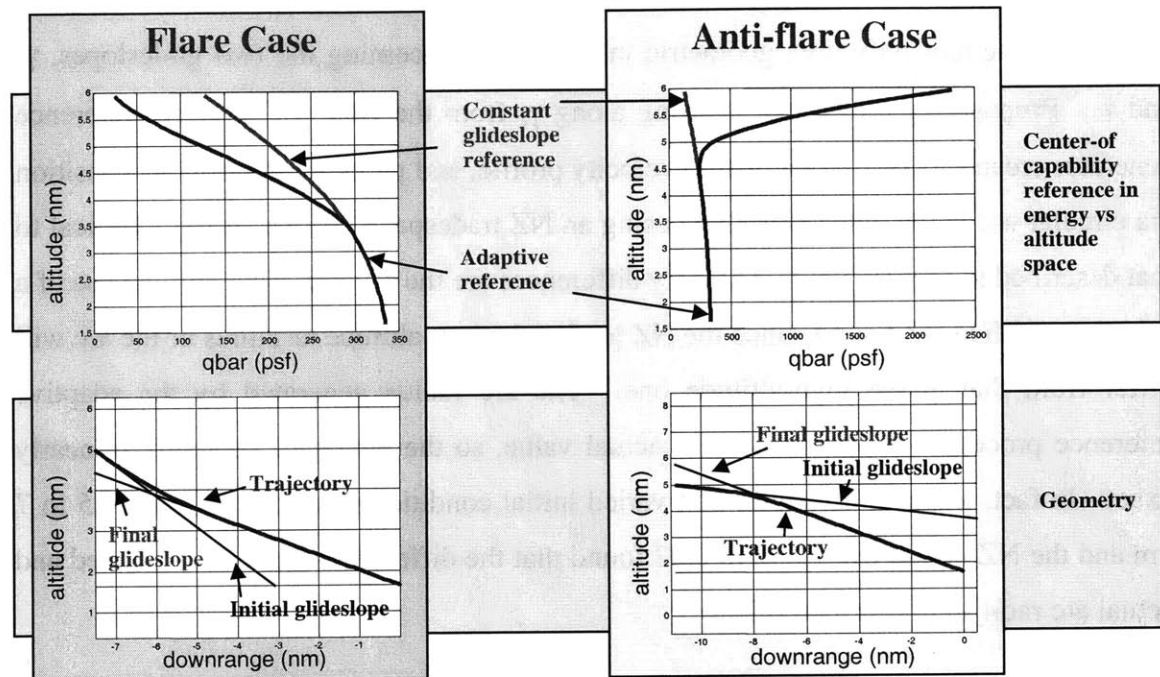


**Figure 5.34:** Adaptive C-o-c Reference (wings level) for Flare and Anti-Flare Cases

The adaptive reference, in addition to emulating the longitudinal geometry, must also incorporate the lateral channel. Bank maneuvers dump lift, and definitely affect the center-of-capability. Figure 5.35 shows the sensitivity of the center-of-capability condition to bank angle. Each reference was calculated “upwards” from the ALI and held at a constant bank for purposes of comparison. Notice that the references for  $0^\circ$  and  $10^\circ$  bank angle are almost identical, but those of  $40^\circ$  and  $50^\circ$  differ widely. As the bank angle increases, the induced effect becomes more pronounced. This behavior is intuitively understandable since loss of lift is proportional to the sine of the bank angle. It should also be noted that energy discrepancies are largest at the higher altitudes, due to the integrated effect of comparative lift variations. Therefore, the reference with a constant  $50^\circ$  bank requires an initial dynamic pressure over 500 psf from altitudes greater than 29,000 ft to offset the relatively protracted period of reduced lift.

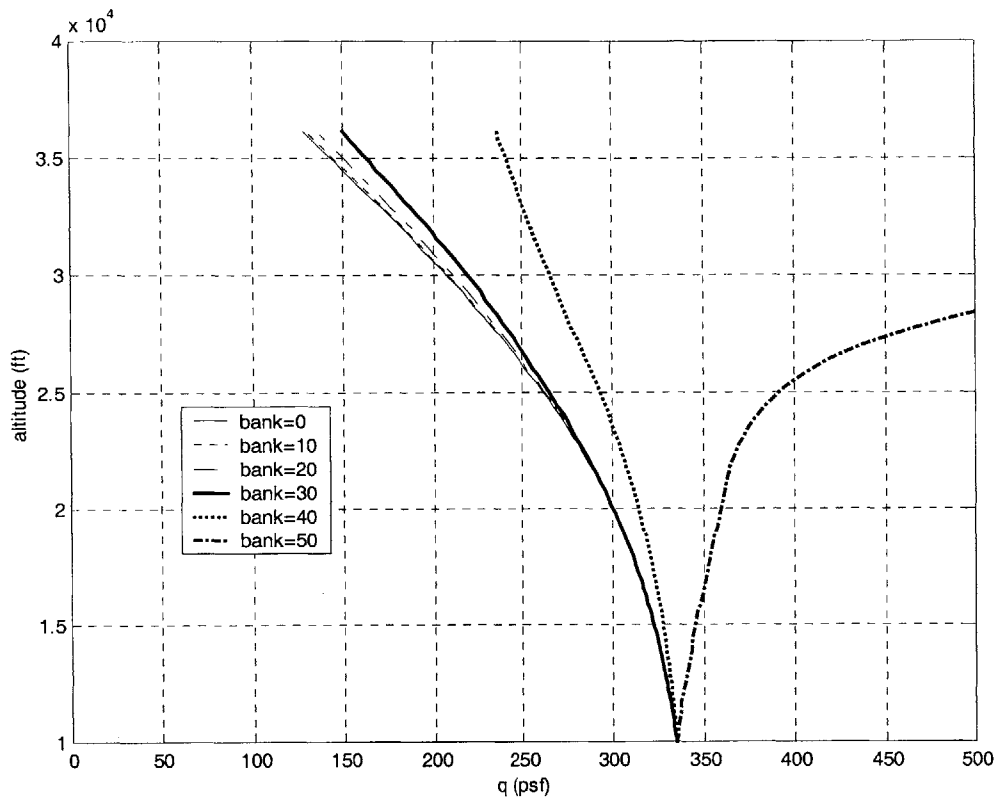


**Figure 5.35: Sensitivity of C-o-c to Constant Bank Angle**

In a typical entry scenario, bank angle would not normally be held constant over a significant altitude range, but correspond to necessary lateral maneuvers. The adaptive reference utilizes the exact lateral geometry of the chosen trajectory in its calculations. Therefore, the effect of bank maneuvers during the acquisition and HAC turns are properly incorporated at the corresponding altitudes. Unlike the longitudinal channel, all necessary lateral data is available before reference generation, so no emulation, however accurate, is needed. Figure 5.36 shows the difference in center-of-capability reference due to the inclusion of the lateral component. Note how the relatively brief HAC turn below  $30^\circ$  bank has hardly any effect, whereas the longer acquisition turn at a steeper sustained bank angle begins to generate a significant difference. The associated lateral geometry for this example is provided in Figure 5.37. An additional example

highlighting the effect of bank angle on the maximum and minimum dq/dt is provided in Appendix C.

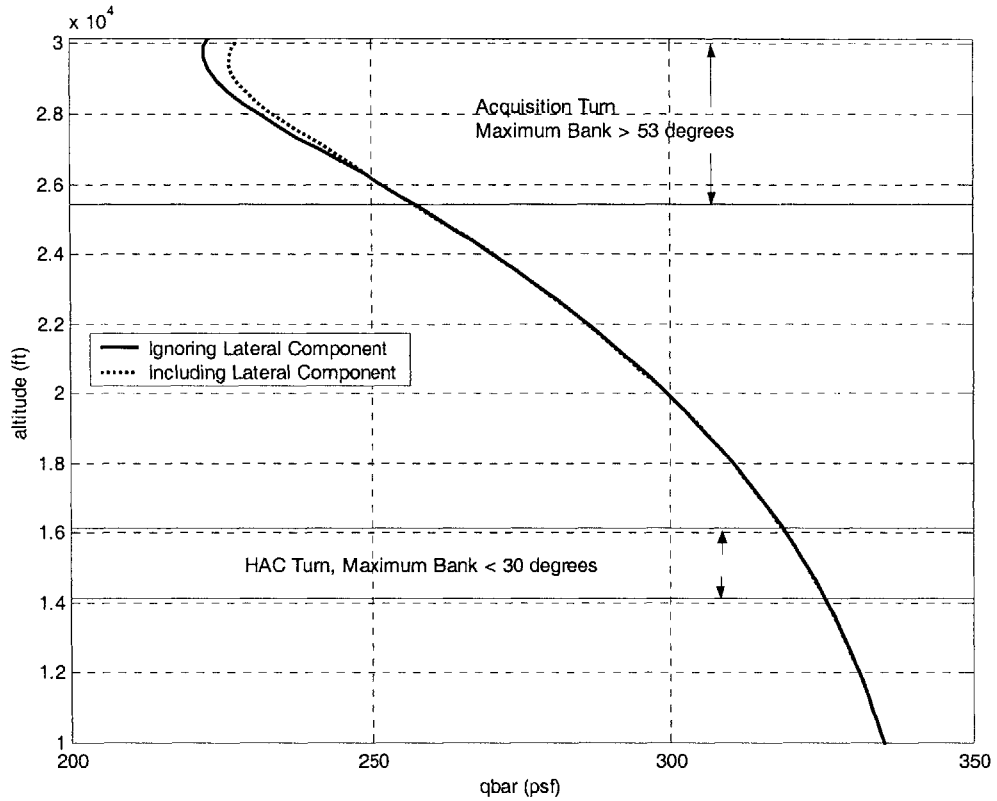


**Figure 5.36:** Effect on C-o-c Reference Due to Lateral Component

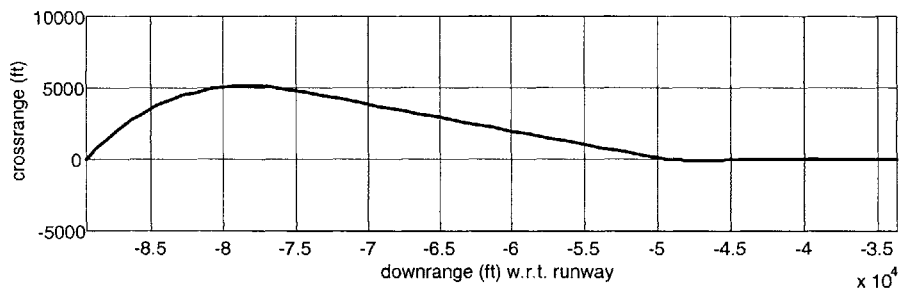


**Figure 5.37:** Lateral Geometry for Figure 5.36

## 5.6 Section 5.6 Optimized Trajectory Computation

While the adaptive center-of-capability reference represents the ideal energy state at each point along the trajectory, actual energy conditions do not usually match the ideal conditions at initiation. Trajectory computation algorithms bring the actual energy states to match the ideal reference in the minimum time and distance possible using:

- Full capability of the speedbrake
- Adherence to established geometric segments
- Continuous vehicle trim

The advantage of using the adaptive center-of-capability reference is apparent as it provides the logic for effective speedbrake placement. Figure 5.38 shows the energy matching procedure. At each altitude step, the trajectory computation algorithm propagates the dynamic pressure ( $q$ ) based on the current speedbrake setting. The error ( $q_{\text{cross}}$  error) at the next step between the propagated  $q$  and the center-of-capability reference is minimized using an adaptive gain on the speedbrake. The speedbrake position that minimizes the  $q_{\text{cross}}$  error at the next step becomes the desired setting for the current step. Note that while there is necessarily an iterative procedure at each altitude step to minimize the  $q_{\text{cross}}$  error, the technique does not rely on computationally intensive “shooting” methods, where different trajectories are generated in their entirety and subsequently analyzed to choose the most desirable. Additionally, since change in speedbrake position correlates approximately linearly to change in  $q$ , the small iterative procedure is highly convergent, stable, and quick. It should be noted that the X-34 speedbrake does not have infinite potential to eradicate  $q_{\text{cross}}$  errors, as it is physically limited between 0 and 103 degrees of extension. During conditions of considerable energy mismatch between the vehicle state and the center-of-capability reference, no speedbrake setting might bring the  $q_{\text{cross}}$  error to zero in a single altitude step. In the interests of decreasing the  $q_{\text{cross}}$  error in as little altitude as possible, the speedbrake is either fully open or closed. Note that this uses speedbrake saturation to reach the condition of maximum robustness most quickly. If such saturation is

considered undesirable, the alternative is simply reaching the maximum robustness condition more slowly.

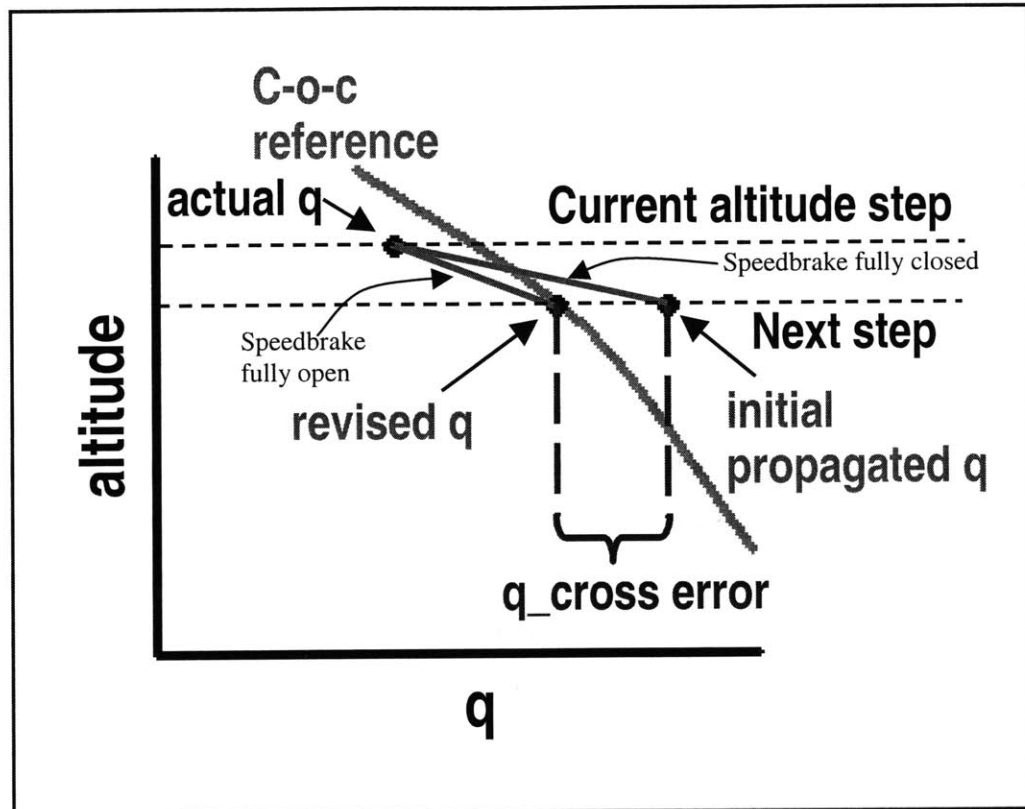


Figure 5.38: Energy Matching Procedure

## **Chapter 6**

# **Onboard Trajectory Generation Component Integration**

### **6.1 Overview**

A thorough understanding of the individual technology components introduced in Chapter 5 provides the necessary background to appreciate the system-level interactions between components described in this chapter. The components are employed within a self-contained master algorithm, coded in MATLAB, that performs the functions of onboard trajectory generation completely autonomously [16]. The behaviors of the output are intimately connected with the structure of component arrangement, which stems from an overarching obligation to minimize computation time while maintaining algorithmic stability over a wide range of conditions.

The chapter begins with a description of the nature of the longitudinal/lateral coupling, with particular attention to the ramifications for integrated tradespace scanning. Subsequently, the next generation guidance algorithm for onboard trajectory generation is explained in detail, with an outline of the data flow structure and its rationale. Finally, the special and highly leveraged contribution of the adaptive reference component is showcased within the context of program output.

### **6.2 Nature of Longitudinal/Lateral Coupling**

For an autonomous trajectory generation scheme that purports to produce flyable, three-dimensional trajectories, the integration of the longitudinal and lateral channels is an absolute requirement. The coupling occurs in both a geometric and dynamic sense, and is especially important in the tradespace formation process.

Geometry intimately connects the longitudinal and lateral design. Beyond producing a viable path that eliminates crossrange errors by bringing the vehicle into alignment with the runway centerline, the lateral channel generates an exact ground track distance to

either the runway threshold or a waypoint such as the ALI. Many of the longitudinal elements are formulated as functions of the ground track distance. In fact, the entire TPBVP setup demands ground track information, as evidenced in Figure 5.1. Geometry also connects the two channels in a relationship flowing from the opposite direction, establishing true mutual dependency. This is evidenced by the glideslope output of the longitudinal design being vital to the lateral plan. The cosine of  $\gamma$  in equation 5.62 converts the vehicle velocity into a horizontal velocity, which is necessary in the process used to account for the orthogonal acceleration components, and ultimately the acquisition radius.

In addition to the geometric relation, the two channels are coupled dynamically. The flight path angle of the longitudinal design affects the lateral bank angle calculation of equation 5.55, both of which are needed to generate suitable center-of-capability references. The velocity profile used in the NZ tradespace calculation for a specific gamma stems from speedbrake position choices that are influenced by the dynamically-coupled adaptive reference. Of course, the acceleration components of the longitudinal channel affect the acquisition turn radius.

The best way to understand the true nature of the longitudinal/lateral coupling is in the context of the onboard guidance algorithm. This section concentrates on the tradespace scanning function, which handles most of the intricacies of the coupling procedure. The following section provides a complete overview of the master algorithm from start to finish, and will reinforce some of the material introduced here.

Figure 6.1 showcases the nested interplay between the lateral and longitudinal tradespace scanning functions. The lateral scanning function occurs first, with the aim of determining the maximum and minimum acquisition turn radii (acquisition turn constraints), that permit the calculation of ground track distances. The maximum acquisition turn radius is calculated from lateral geometric limits that do not depend on the yet-to-be generated longitudinal design, hence it is calculated first. The minimum acquisition turn radius is determined from the lateral acceleration limits, which, as has



been explained, depend on the choice of glideslope. Since that information is unavailable at this point in the algorithm, a surrogate place-holder  $\gamma$  allows a predicted calculation of minimum  $R_{AC}$ . This prediction also relies on a longitudinal acceleration component allotment pegged at the maximum NZ bound.

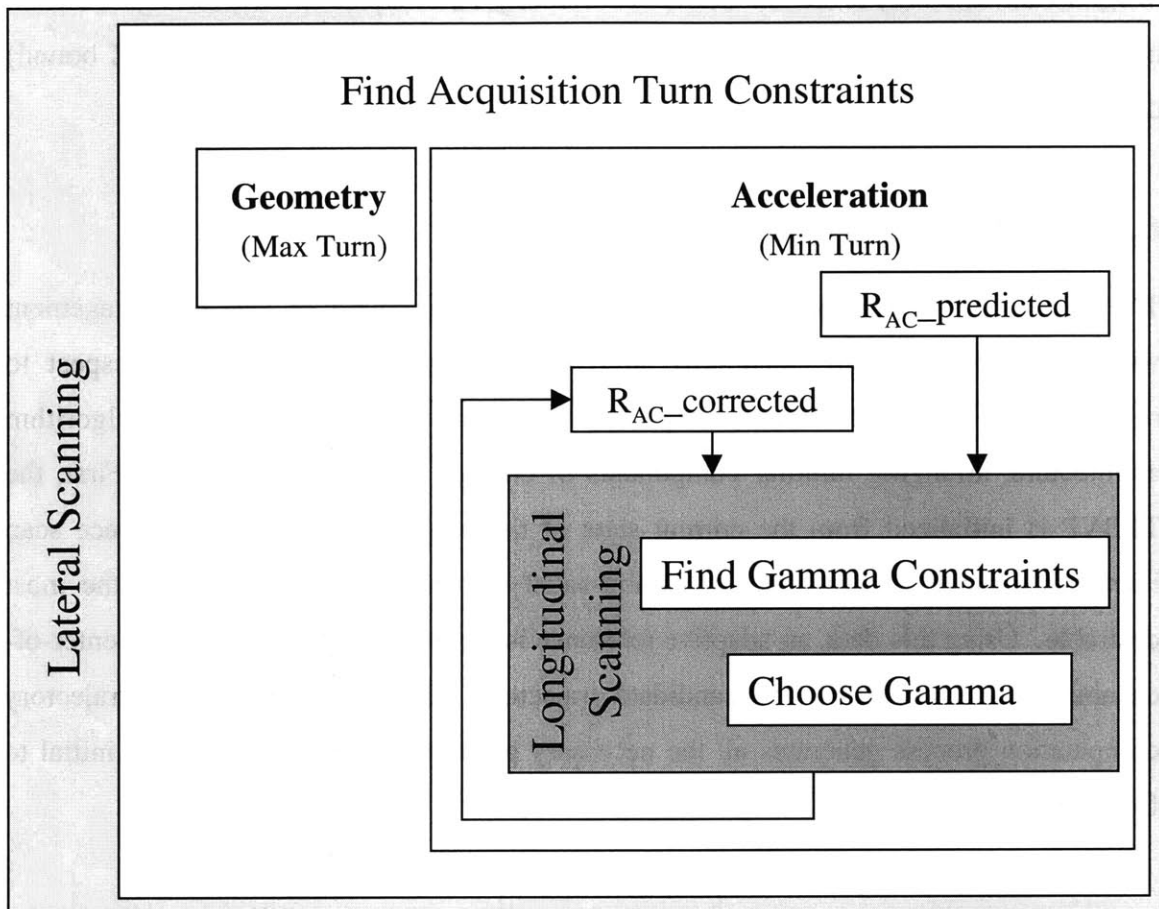


**Figure 6.1:** Scheme for Lateral and Longitudinal Tradespace Coupling

The ground track from the initial predicted minimum acquisition turn determination feeds into the longitudinal scanning function, which performs its usual procedures to ascertain the range of  $\gamma_1$ 's. Based on the desirability criterion, a candidate  $\gamma_1$  is chosen, which is then passed back to the lateral acceleration calculation, replacing the surrogate place-holder  $\gamma$ , and resulting in a revised minimum  $R_{AC}$ . At this point the lateral scan is complete. Of course, the longitudinal scan must then be re-initiated using either the recently-revised minimum turn ground track, or the maximum turn ground track

calculated earlier. The closed-loop coupling problem (a chicken & egg scenario) is therefore solved using a simple predictor-corrector process that provides a quick and conservative answer. Two factors minimize the need for additional lateral/longitudinal loop iterations. Further alterations to the flight path angle have been found to be insignificant, and only affect the horizontal velocity  $V_H$  of equation 5.62 through a cosine operator. In addition, the longitudinal acceleration component (maximum NZ bound) does not vary between iterations.

### 6.3 Master Algorithm Data Flow

The onboard trajectory generator solves the general problem of energy management without violating system constraints, and provides optimized output with respect to robustness. Figure 6.2 offers a simplified functional outline of the master algorithm architecture, arranging familiar components of chapter 5 in sequential form. First, the TPBVP is initialized from the current state of the vehicle. Next, the tradespace scan identifies a range of allowable, constraint-satisfying geometries and chooses the most desirable. Using this data, an adaptive reference is generated that identifies the center-of-capability condition along the candidate trajectory. Finally, an optimized trajectory computation process generates all the necessary guidance parameters from the initial to final state.

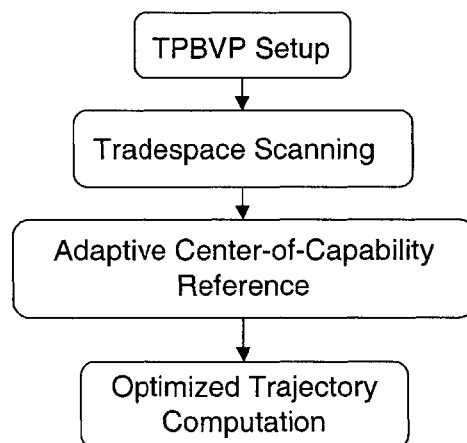


**Figure 6.2:** Simplified Master Algorithm Data Flow

Figure 6.3 shows the master algorithm data flow in more exhaustive detail. The onboard trajectory generator commences with an initialization of the I-loads that describe the X-34's aerodynamic and mass properties. The nominal landing site data is entered at this stage, along with HAC particulars and all the preferred vehicle states for the ALI. Desirability criteria, such as the NZ bound, are inserted here. Of course, the current vehicle states become the initial conditions for the TPBVP.

Next in the data flow is a series of functions that determine the admissible trajectory tradespace given the initialized setup. In the manner described earlier, the maximum and minimum acquisition turn radii are found from geometric and acceleration limits, providing the longest and shortest ground track distances allowable under the given constraints. If the minimum radius exceeds the maximum radius, the initial conditions must be incompatible with the given constraints, representing either an impossible situation or one requiring a relaxation of limits. For situations with a valid lateral tradespace, an acquisition radius is chosen from within the bounded region and the resulting ground track is fixed, the  $d\chi$  heading change data mapped, and the downrange and crossrange (x and y) positions known for every point along the trajectory. In this thesis research, the criterion for the turn choice was simply the minimum radius possible, as it represented the most robust universal bias, aiding critical low-energy cases by assuring the shortest flying distance while deferring to the powerful speedbrake capability the task of handling cases with excess initial energy. This guideline also minimizes the wait before a HAC tangency is reached. Using the lateral channel as a deliberate energy modulation control was beyond the scope of this thesis; a full geometric and dynamic integration with the longitudinal channel for flyable three-dimensional flight was considered sufficient.

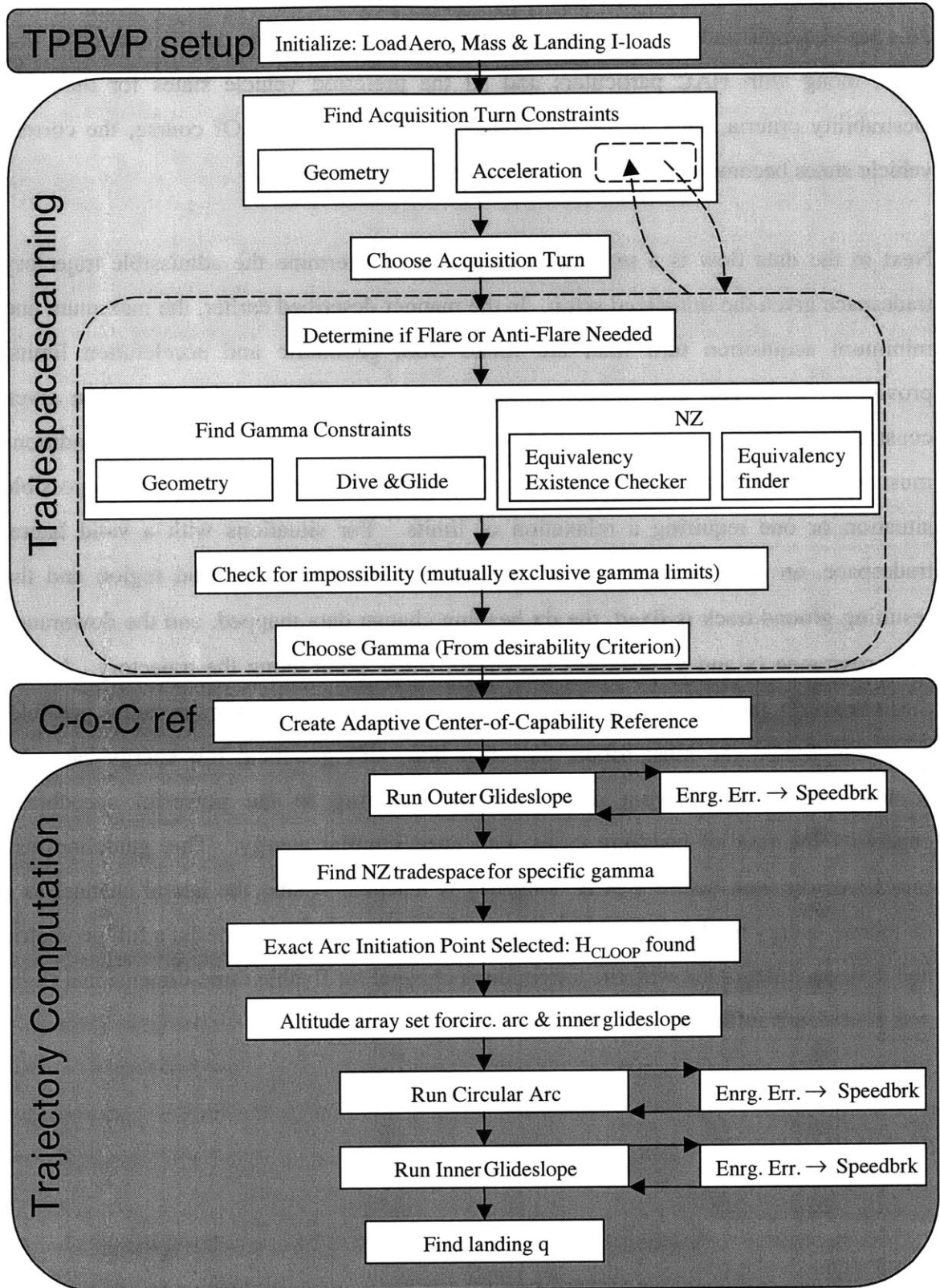


Figure 6.3: Detailed Master Algorithm Data Flow

After the establishment of a ground track distance and the lateral particulars, the longitudinal tradespace scan begins. First, a function determines whether a flare or an anti-flare is needed. The location of this function at the start of the repeated longitudinal tradespace scan is not accidental; the difference in ground track distance from the predicted and corrected  $R_{AC}$  has sometimes been sufficient to switch flare types since the  $H_{shali}$  point can change with respect to the initial vehicle position. Next, the steepest and shallowest outer glideslopes from each of the geometric, max dive and glide, and NZ limits are calculated. For the NZ process, a function determines if an equivalency point can possibly exist within the given geometric setup, and if affirmative, activates another function to discover it. For situations allowing immediate arcs, an NZ limit scanner uses initial condition velocity data; past the equivalency point the scanner performs a single propagation to ascertain the maximum velocity and generate a conservative limit. Once all the outer glideslope limits are found, the most restrictive set represents the longitudinal tradespace. If the boundary extremes are incompatible, the limits dictate no suitable trajectory. In the case of successful tradespace generation, a desirability criterion selects the actual outer glideslope for use. In this thesis, the customary criterion selected an outer glideslope allowing the quickest transition to the inner glideslope, where the width of the  $dq/dt$  corridor would be wider. Such a criterion favored robustness.

Armed with knowledge of the entire lateral profile and the chosen outer glideslope, the adaptive center-of-capability reference is calculated starting at the ALI and propagating upwards in altitude. Reference data for altitudes above the vehicle's initial condition can be produced for analytical purposes, but are omitted in practice for the sake of computational efficiency. Since the longitudinal flare/anti-flare radius has not been defined at this point, an emulated geometry provides a highly accurate estimation.

The optimized trajectory computation process begins with a propagation along the outer glideslope from the initial condition to the intercept point of  $\gamma_1$  and  $\gamma_2$ . The energy error between the vehicle state and the center-of-capability reference drives the speedbrake setting for each altitude. The dynamics calculation includes any lateral maneuvers that

may be occurring simultaneously, and determines the necessary bank angle. The outer glideslope propagation terminates once it reaches the intercept point, as the requisite velocity information at all conceivable flare/anti-flare initiation positions has been discovered and recorded. Using this data, the NZ tradespace function calculates the obligatory NZ loads for every candidate arc transition. The chosen arc (and corresponding initiation altitude  $H_{\text{LOOP}}$ ) is selected according to a desired NZ value, finally providing the last compulsory detail for the complete specification of the three-dimensional geometry. This information allows an altitude array to be generated as an index for the remaining constrained trajectory propagation.

The vehicle states at the start of the circular arc are interpolated from the previous outer glideslope propagation. State information along the outer glideslope below the  $H_{\text{LOOP}}$  altitude is thereafter stale and no longer useful. The optimized trajectory generation procedure continues along the circular arc and then the inner glideslope, including lateral dynamics and setting the speedbrake position to minimize energy errors. The final result of a successful run is a complete, flyable trajectory with terminal conditions that match the ALI criteria.

## **6.4 Significance of the Adaptive Reference in Program Output Context**

The adaptive center-of-capability reference deserves special recognition as the key ingredient that enables rapid trajectory optimization in the absence of computationally intensive shooting methods. Its highly leveraged contribution can now be appreciated within the context of program output.

Figure 6.4 showcases a comparison between trajectory outputs generated with and without the use of an adaptive reference. The initial conditions of both examples are identical, and the lateral channel is purposefully omitted (wings level situation) for clarity. A dashed line represents the energy reference in the  $q$  vs. altitude plots while the solid line indicates the output trajectory energy history.

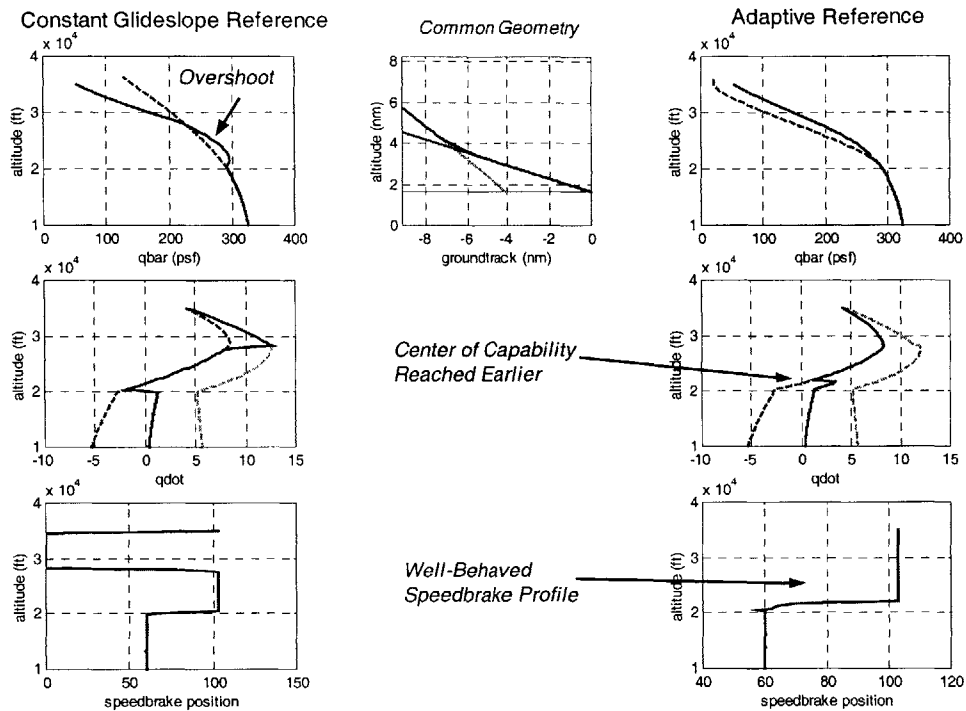


**Figure 6.4:** Comparative Impact of the Adaptive Reference on Trajectory Output

We first examine the family of constant glideslope (non-adaptive) reference outputs on the left side of the figure. We immediately see that an overshoot occurs in the  $q$ -space, seemingly indicating faulty speedbrake positioning. According to the energy reference, the initial condition represents a low energy case, so the optimized trajectory computation function uses the full capability of the speedbrake to minimize the energy error as quickly as possible. Since the vehicle must increase its energy relative to the reference, the speedbrake is commanded to  $0^\circ$  (completely closed). The condition of flying along the edge of the capability corridor is apparent in the altitude vs.  $q\dot{}$  plot, where the  $0^\circ$  speedbrake represents the maximum instantaneous potential for energy increase. At the overshoot altitude, the vehicle energy state suddenly exceeds the reference, and the speedbrake is forced to  $103^\circ$  (completely open). From here, the vehicle hugs the opposite edge of its capability corridor in an effort to decrease energy, until the reference is again reached, this time allowing a moderate speedbrake setting that keeps the vehicle in a condition of maximum robustness until the ALI.

We now examine the family of adaptive reference outputs on the right side of Figure 6.4. Here the initial condition represents a high energy case, so the optimized trajectory computation function commands the speedbrake fully open. Once the reference is reached, the speedbrake leaves its maximum deceleration capability and stabilizes around the setting providing maximum robustness. The adaptive reference clearly provides a more accurate guideline to the center-of-capability condition, offering a correct logic criterion for speedbrake position decisions. In addition to, and well as a consequence of, a better-behaved speedbrake profile, the adaptive reference allows the center-of-capability condition to be reached earlier, resulting in a quantifiably more robust total trajectory.



# Chapter 7

## Results

### 7.1 Overview

This chapter assesses the performance of the guidance output from the autonomous algorithms through a comparison with a standard X-34 reference profile and an inquiry into a series of off-nominal cases. The standard X-34 reference profile serves as a convenient baseline for a reality check, and the off-nominal cases provide demonstrations of the onboard guidance versatility.

### 7.2 Comparison with Existing Guidance

The DRM4 drop mission of the X-34 is used to demonstrate the trajectory design algorithms. This mission starts with a drop of the X-34 from the belly of the Orbital Sciences L1011 aircraft at 35,000 ft altitude at a specified drop location, velocity, and heading. The guidance initiates a few seconds after the drop, with the conditions given in Table 7.1. The vehicle is initialized in subsonic TAEM and must reach the final condition of the ALI. The ALI occurs at an altitude of 10,000 ft, a dynamic pressure of 335 psf, a downrange of 33668 ft, a glideslope of  $-20.5$  degrees, and a heading and crossrange of zero.

**Table 7.1:** Initial Conditions at Guidance Start for DRM4 Drop

Altitude	30413 ft.
Velocity	686.4324 ft/s
Crossrange	20,426 ft.
Downrange to runway	89,389 ft.
Heading angle	-29.9375 degrees

When faced with the DRM4 drop mission, the autonomous algorithms calculate the most robust trajectory under the prevailing constraints. Figure 7.1 compares some guidance references autonomously generated with standard DRM4 references for a nominal drop.

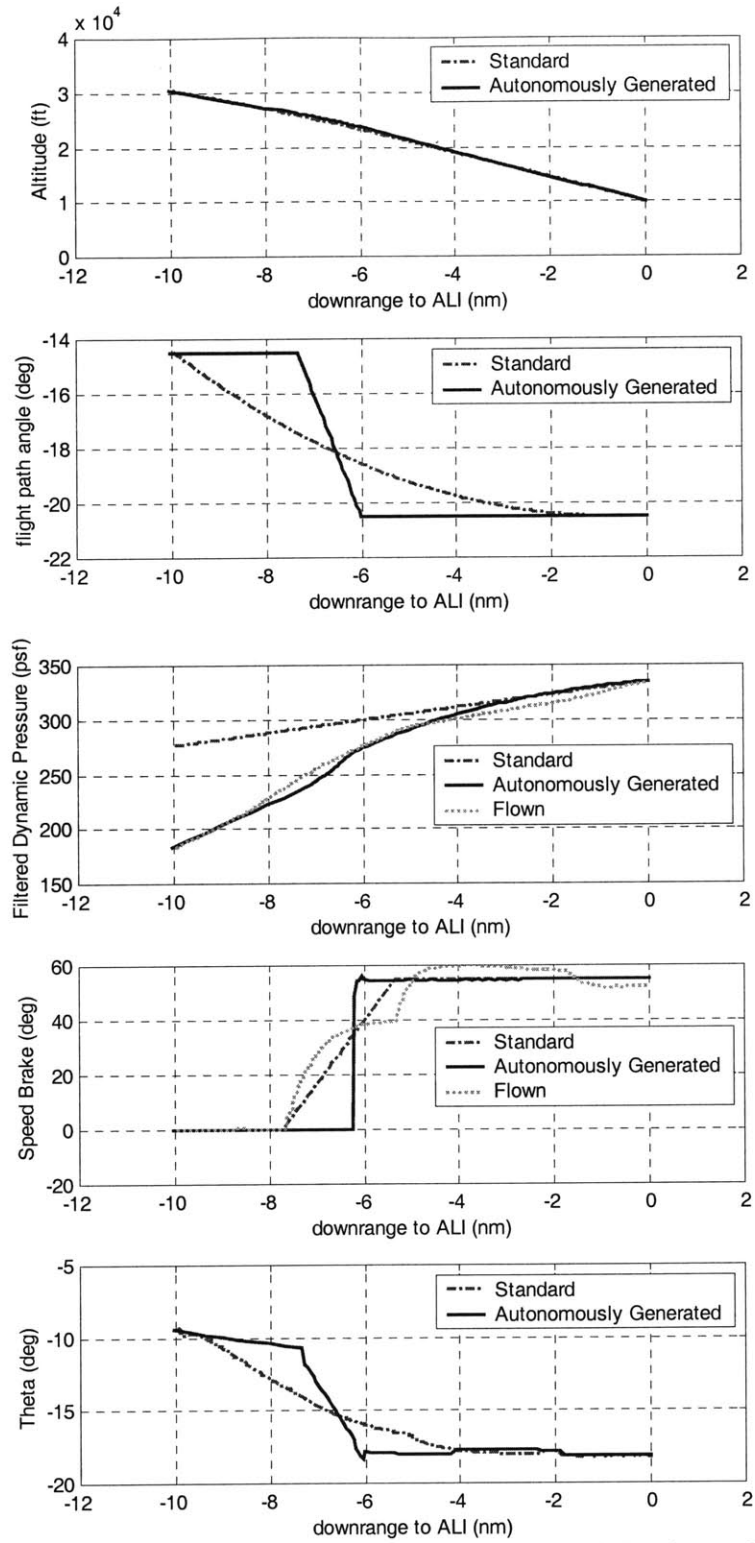


**Figure 7.1:** Comparison of Onboard and Traditional Guidance for DRM4 Drop

The altitude vs. downrange plot illustrates the onboard guidance reference closely matches the standard reference, which is performing a slight anti-flare for most of the regime. In the flight path angle vs. downrange plot, the effect of the three longitudinal segments of the onboard guidance methodology can be more clearly seen.

The dynamic pressure vs. downrange plot highlights a very important difference between onboard and traditional canned references. The  $q$  value of 170 psf at 10 nm downrange represents the actual vehicle state at its initial condition. The onboard reference represents a flyable path from this initial condition to the desired terminal condition of 335 psf. Most importantly, though, it represents the ideal path from the standpoint of robustness. The standard reference, being canned, only represents a guideline dynamic pressure profile considered desirable, which loses relevance the further the actual vehicle conditions diverge from it. In the traditional guidance scheme the flight control (its output also shown on the plot) will issue commands to decrease the errors between the vehicle's actual energy state and the reference energy, but cannot be relied upon to perform this feat with the intelligence necessary to ensure maximum robustness. The onboard guidance solves this problem.

The speedbrake vs. downrange plot highlights the decision of the onboard guidance to utilize the full capacity of the speedbrake to reach its desired trajectory. Both the standard and onboard guidance references start with the speedbrake fully closed in order to gain velocity since the initial drop condition is low on energy. While the standard guidance gradually opens the speedbrake over a distance of more than 2 nm, the onboard guidance keeps it closed until the conditions are right to transition to the desired 55 degree setting of the final glideslope. The result is reaching the final condition slightly sooner. One may note that the capability of a speedbrake to change its position is not infinite, i.e. there is a mechanical rate limit in deg/sec. The X-34 speedbrake actuator bandwidth is quite high and can control the rate changes requested. If desired, rate limiters can be included in the design process.

The theta vs. downrange plot exhibits many of the same general characteristics as the flight path angle vs. downrange plot. This would be expected since theta is the angular sum of the flight path (gamma) and angle of attack (alpha).

Figure 7.2 showcases additional data from onboard guidance output for the DRM4 Drop case. Here we witness the role of the adaptive reference, more geometric and performance data, and the capability corridor. Figure 7.3 provides a three-dimensional representation of the trajectory. Additional data for this case can be found in Appendix D.

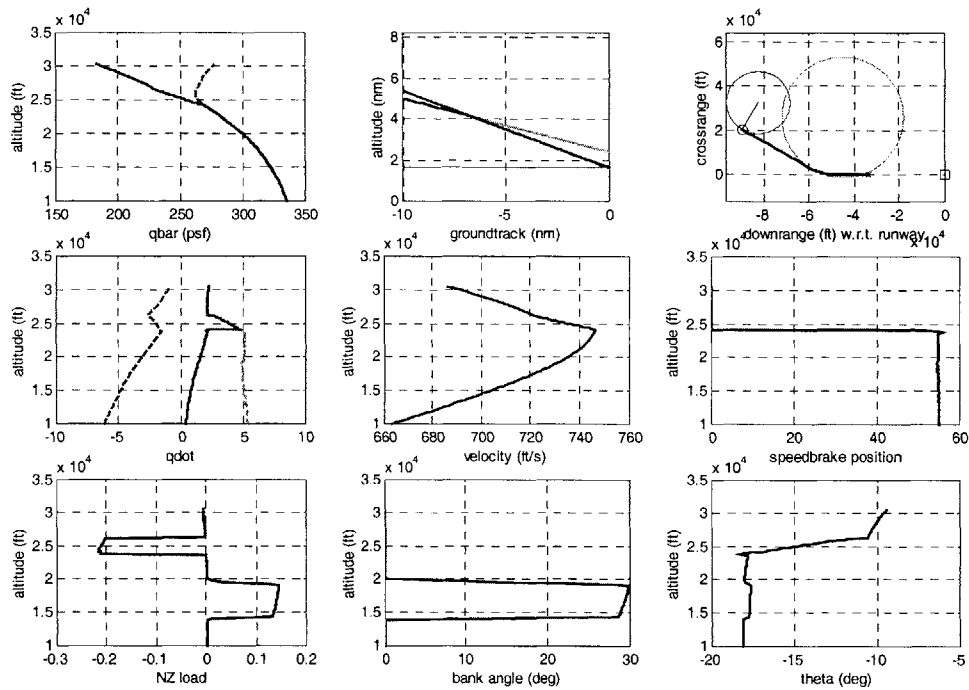


**Figure 7.2:** Program Output for DRM4 Drop Case

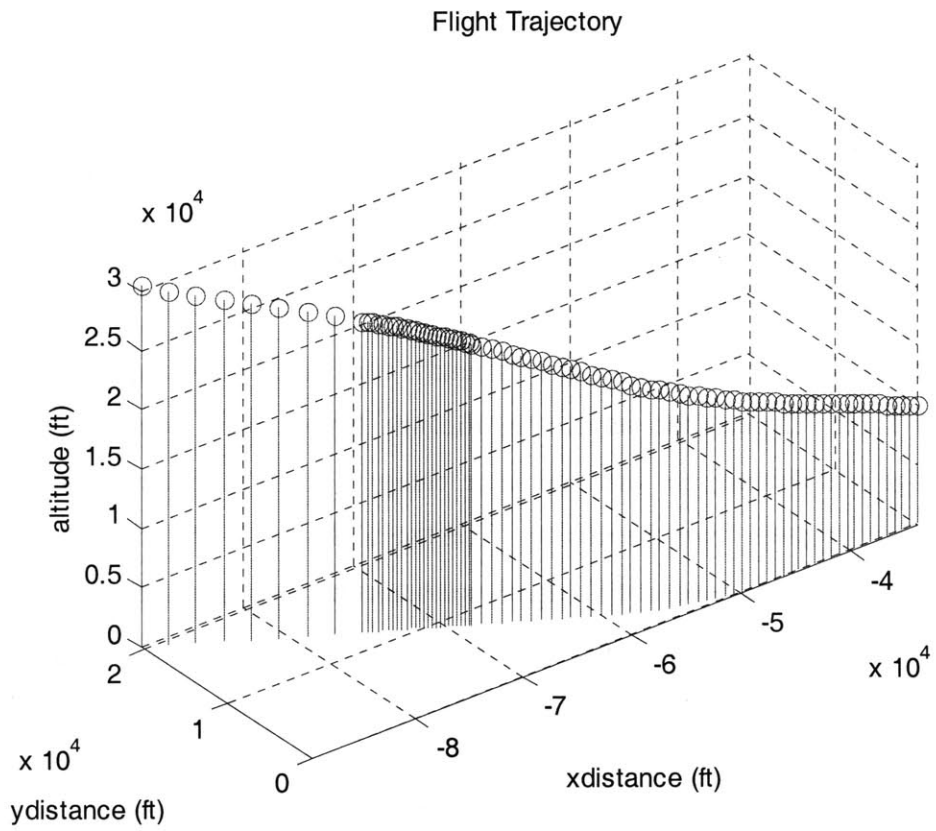


**Figure 7.3:** Three Dimensional Representation of DRM4 Drop Trajectory

### 7.3 Algorithm Performance for Off-Nominal Conditions

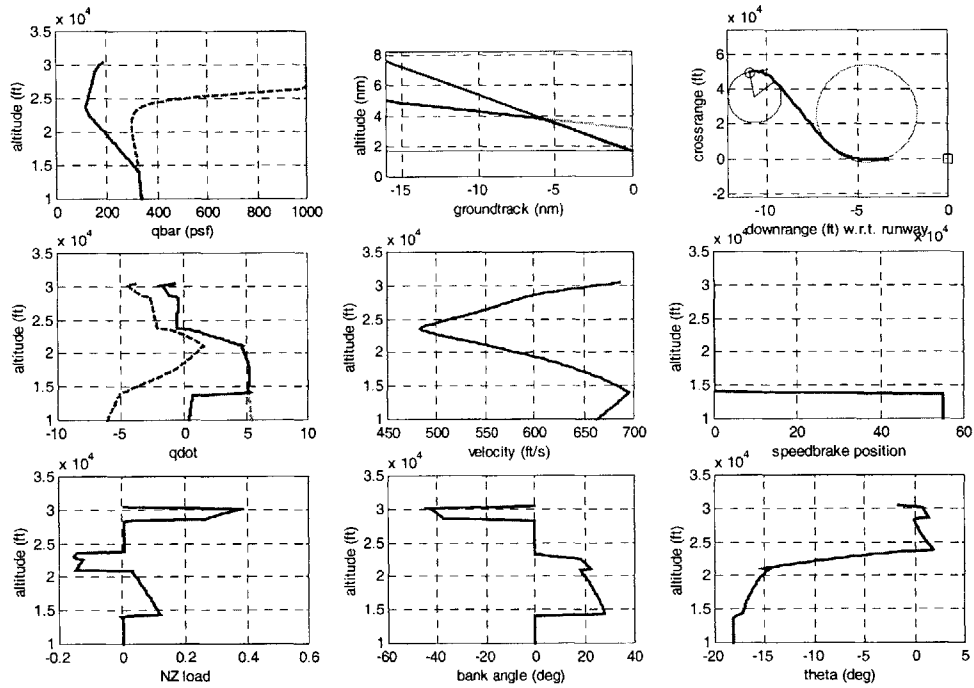
The full advantage of using onboard trajectory generation, from a vehicle performance standpoint, occurs with drastically off-nominal initial conditions. Figures 7.4 and 7.5 showcase the results from the conditions given in Table 7.2.

**Table 7.2:** Delta Initial Conditions for Sample Off-Nominal Case #1

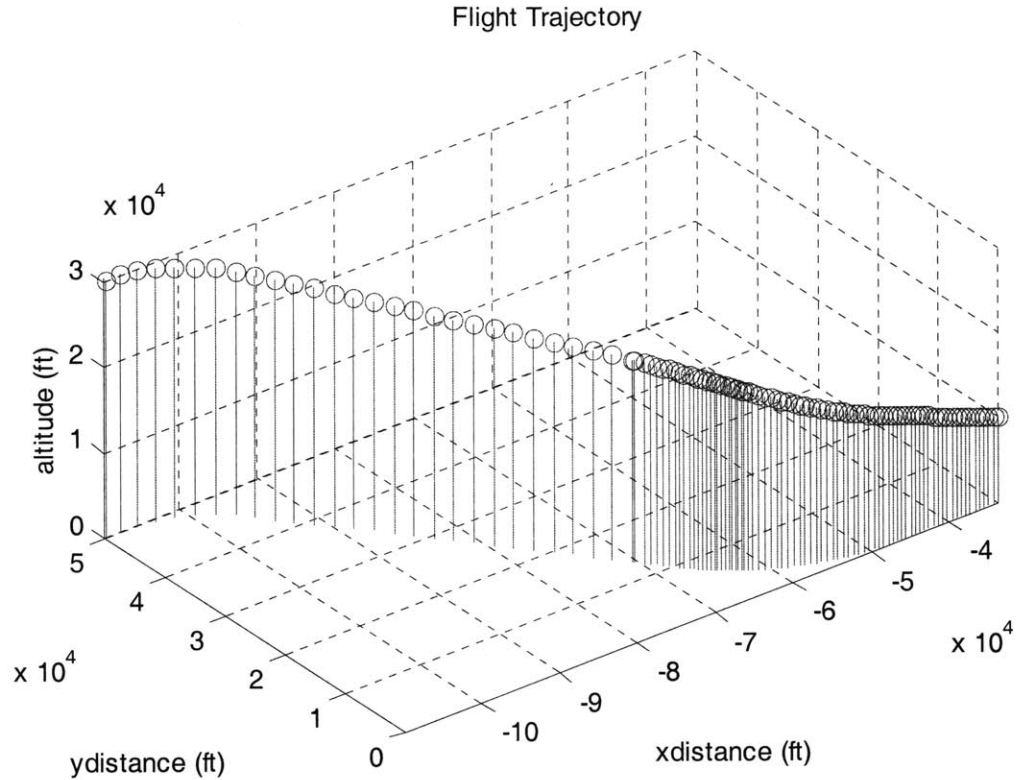
$\Delta$ Altitude	0
$\Delta$ Velocity	0
$\Delta$ Crossrange	+29,574 ft
$\Delta$ Downrange to runway	+20,231 ft
$\Delta$ Heading angle	+39.9375 degrees

While the standard DRM4 Drop case is already considered low energy, the initial conditions of Table 7.2 place the vehicle significantly farther away from the runway, in both crossrange and downrange, with the same energy. Also, the initial heading angle faces inconveniently away from the runway. The lateral design results in a sharp circular acquisition turn that starts beyond 40° (rightward banks are negative, leftward banks are positive) but then fades slightly as the velocity momentarily decreases. After a straight lateral segment, the HAC brings the trajectory into alignment with the runway centerline. Since the starting condition is well below the adaptive energy reference, the speedbrake is initially commanded completely closed. Despite this, the velocity and dynamic pressure decrease due to the shallow angle of the outer glideslope. This behavior introduces an important observation. The desirability criterion used for this run emphasized the importance of reaching the inner glideslope at the earliest altitude, thus maximizing the time along the condition where the  $\dot{q}$  capability corridor is widest, thus providing a trajectory with maximum time at the condition of maximum theoretical robustness. However, the shallow angle of the outer glideslope necessary to achieve this causes a momentary energy loss, causing the capability corridor to shrink to its narrowest point at the minimum velocity, until the anti-flare begins to increase the steepness of the trajectory and the velocity and dynamic pressure start rising again. This provides a clear example of how the particular desirability criterion emphasizes late-trajectory robustness over early-trajectory robustness. More complex desirability criteria can provide a

balanced approach, especially when significant ground track distance remains from an exceptionally low energy starting point, where the vehicle's threatened ability to reach the runway is more critical than any inclination toward robustness. Choosing an outer glideslope at or below the quasi-static equilibrium would prevent energy loss in such a case.



**Figure 7.4:** Program output for Sample off-Nominal Case #1



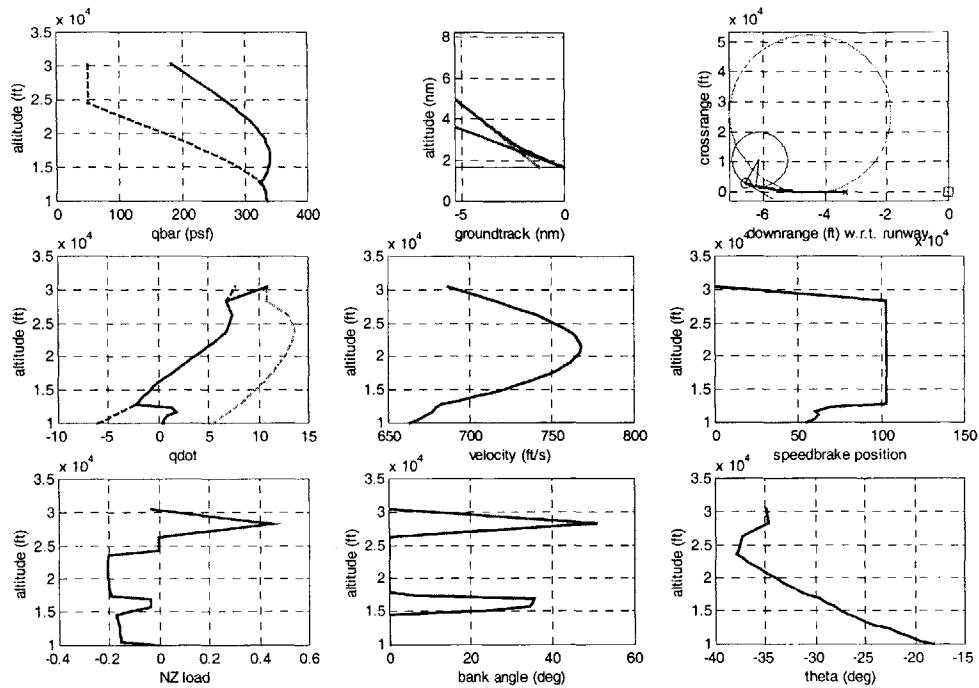
**Figure 7.5:** Three Dimensional Representation of Sample Off-Nominal Case #1

Table 7.3 introduces a second off-nominal case, according to a hypothetical scenario where the X-34 is dropped from the L1011 well past the standard separation point. Figures 7.6 and 7.7 showcase the corresponding autonomous program output. Here we see that the vehicle is dropped well above the inner glideslope with little room for maneuver. A steep outer glideslope and a circular flare allow transition to the inner glideslope just before the ALI. The speedbrake is initially commanded completely open since the starting condition is well in excess of the adaptive energy reference.

**Table 7.3:** Delta Initial Conditions for Sample Off-Nominal Case #2

$\Delta$ Altitude	0
$\Delta$ Velocity	0
$\Delta$ Crossrange	-17,426 ft
$\Delta$ Downrange to runway	-23,518 ft
$\Delta$ Heading angle	0





**Figure 7.6:** Program Output for Sample Off-Nominal Case #2

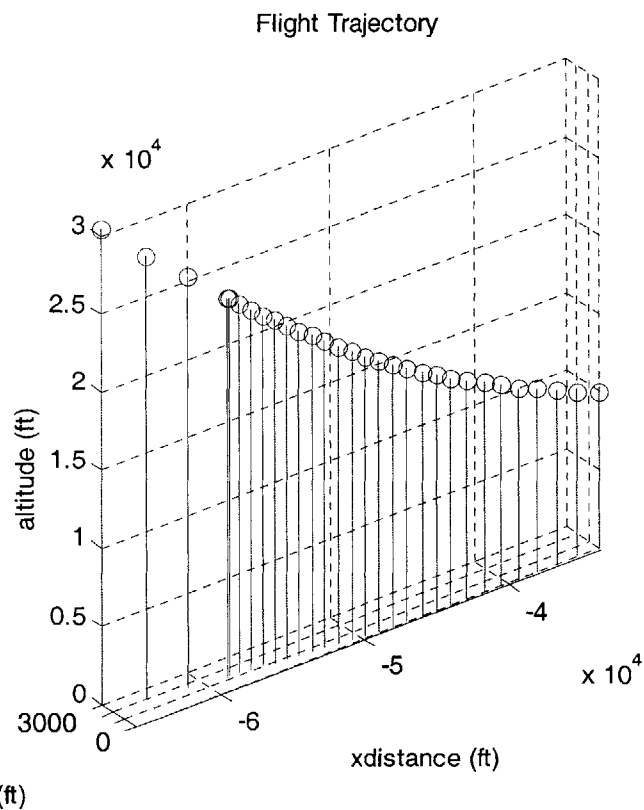


**Figure 7.7:** Three Dimensional Representation of Sample Off-Nominal Case #2

Table 7.4 introduces a third off-nominal case, according to a hypothetical scenario where the X-34 is dropped from the L1011 at a position that proves serendipitous. Figures 7.8 and 7.9 showcase the corresponding autonomous program output. Here we see that the vehicle is dropped very close to the inner glideslope. Its initial energy state is very close to the adaptive reference. Therefore, the trajectory spends almost the entire time flying down the middle of the capability corridor, resulting in an extraordinarily robust plan that does not require the extreme capabilities of maximum or minimum speedbrake deflection.

**Table 7.4:** Delta Initial Conditions for Sample Off-Nominal Case #3

$\Delta$ Altitude	0
$\Delta$ Velocity	0
$\Delta$ Crossrange	-17,426 ft
$\Delta$ Downrange to runway	-4,074 ft
$\Delta$ Heading angle	0

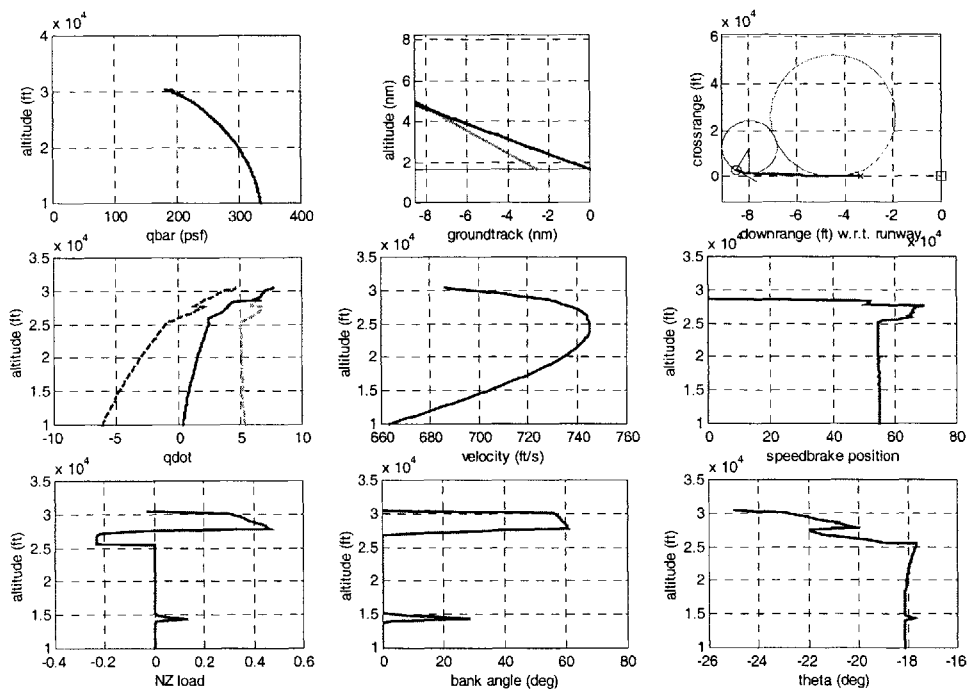


**Figure 7.8:** Program Output for Sample Off-Nominal Case #3

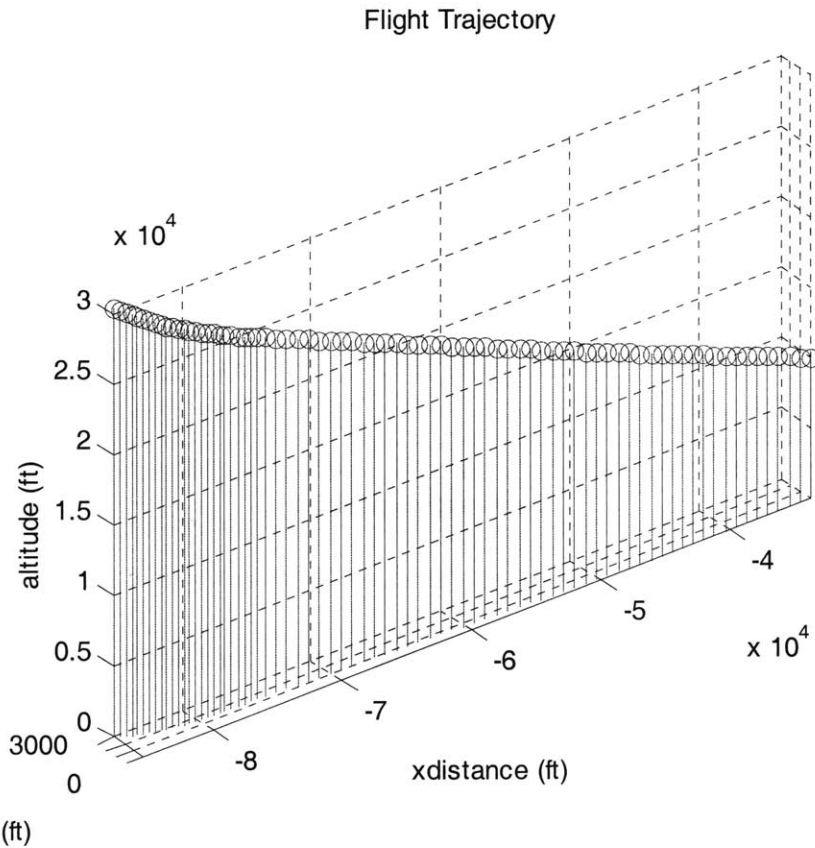


**Figure 7.9:** Three Dimensional Representation of Sample Off-Nominal Case #3

Apart from serving as strictly onboard guidance, the autonomous trajectory generator algorithms can perform sensitivity studies efficiently by varying different initial condition data. One such result is shown in Figure 7.10, where a range of hypothetical heading angles replaced the standard DRM4 Drop heading. Note that the vehicle can handle a  $138^\circ$  spread under the constraint set used.

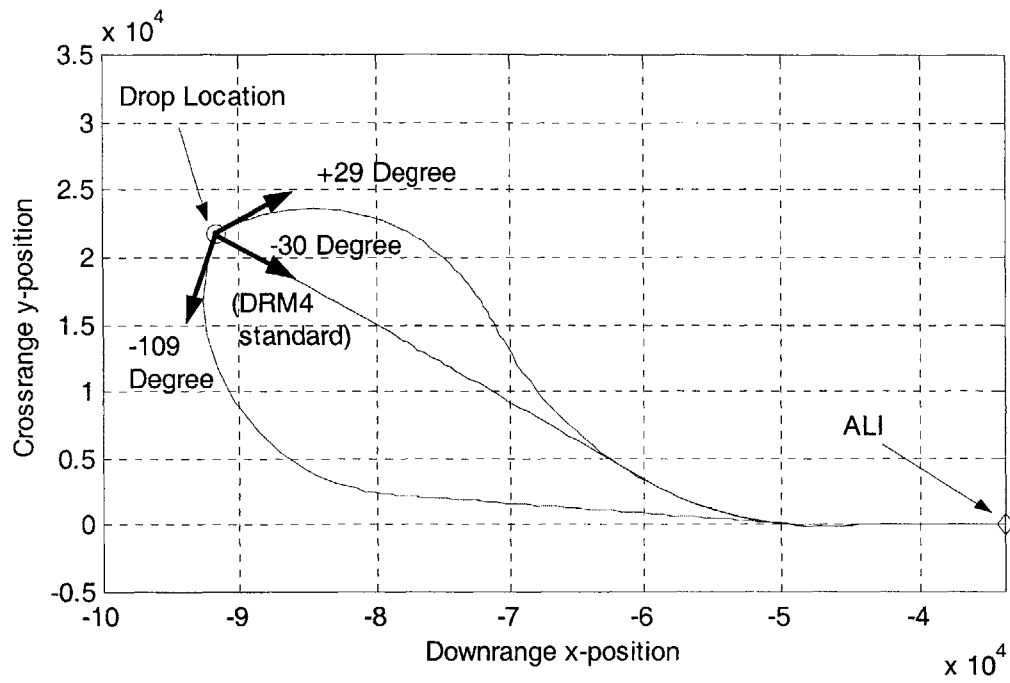


**Figure 7.10:** Recoverable Heading Angle Options for DRM4 Drop Zone

## Chapter 8

# Conclusions and Recommendations for Further Research

### 8.1 Conclusions

Onboard trajectory generation dispenses with the pre-defined trajectories that have been a staple of the RLV community since the early days of the Shuttle era. Such a shift, made possible by a new generation of algorithms harnessing today's increased computational power, can improve performance, add robustness, lower operational cost, and for the first time allow a truly robust abort capability.

This thesis introduced a set of algorithms that enable onboard trajectory generation for low lift over drag gliding RLVs in the subsonic flight regime below an altitude of 40,000 ft., using the NASA/Orbital X-34 vehicle as a representative model. The project successfully demonstrated that autonomous algorithms can design feasible trajectories over a range of initial conditions without human intervention.

In addition to being autonomous, the guidance output of the onboard trajectory generator differs fundamentally from current Shuttle-based approaches. Unlike traditional guidance, whose output commands react to perceived instantaneous vehicle needs, the integrated guidance provides a realistic "future history" in a propagated plan, which can be analyzed for desirability and even optimality. This enables an entirely new approach to RLV guidance, called "Next Generation Guidance" by Draper, that enables an integrated control function to use multivariable techniques to minimize the entire set of trajectory state errors.

To design critical trajectories that become the heart of the advanced guidance, special attention had to be paid to the constraints imposed by autonomy. An efficient design tool approach was selected that employed foreknowledge of key system dynamic tendencies to concentrate on the most important tradeoffs using a minimum of computational

resources. No shooting methods were utilized, and iterative loops were kept to a minimum.

A set of methods was developed to enable onboard trajectory generation, resulting in five key technology components. These emerged as:

- 1) a two point boundary value problem setup
- 2) a constrained trajectory propagation technique
- 3) a fast tradespace scanning method
- 4) the use of an adaptive center-of-capability reference
- 5) an optimized trajectory computation scheme.

The two point boundary value problem captures the required and desired states, while incorporating system constraints. The use of a restricted number of simple geometric segments simplifies the path planning process while allowing sufficient design flexibility. This framework had the additional benign effect of enforcing practical longitudinal paths with desirable monotonic altitude decrease. The lateral channel uses a geometric approach borrowed from the Shuttle guidance, but modified to meet the particular needs of this application.

The constrained trajectory propagation technique exploits the geometric knowledge available from the two point boundary value problem to rapidly generate realistic trajectories with exact control histories. The specified geometry allows a reduction in the order of the dynamic system, enabling faster results than a typical propagator that performs a full integration of the equations of motion. The constrained propagation technique is ubiquitous throughout the onboard planner, being used for velocity data gathering during tradespace definition as well as the final optimized trajectory computation.

The fast tradespace scanning function discovers the allowable range of trajectory shapes, according to a family of constraints. This capability is important for an autonomous system, since knowledge of tradespace borders prevents computation resources from

wasting time pursuing unsatisfactory or infeasible designs. The tradespace is discovered for both the longitudinal and lateral channels, and incorporates a coupling procedure between the two. The predictor-corrector approach used for the coupling was successful enough to suggest the possibility of eliminating the predictor component with further research.

An adaptive center-of-capability reference is discovered that represents ideal vehicle energy conditions along a trajectory. It serves as the enabling ingredient to allow an optimized, not merely satisfactory, trajectory to be calculated onboard. The center-of-capability condition is considered the state of maximum robustness, which is highly prized for its ability to handle unforeseen disturbances.

The optimized trajectory computation process uses the adaptive reference as a speedbrake position logic to provide the best energy performance capable from a set of initial conditions. This is accomplished in a single, straightforward, top-to-bottom calculation, with no requirement for multiple complete trajectory generations or shooting methods. Excellent convergence on speedbrake position was achieved using an adaptive gain. The algorithms currently use the complete capability of the speedbrake to produce desired energy changes in the minimum time possible, although this can be modified if saturated conditions are deemed undesirable. In addition, a rate limiter on the speedbrake might add physical accuracy, but for the altitude step sizes typically used, the lack of one was not a problem.

To assess feasibility, the onboard trajectory generator was benchmarked against the traditional X-34 guidance for a DRM4 drop scenario. The results were encouragingly similar in basic form, with differences showcasing the autonomous algorithms' preference for maximum robustness and the more severe speedbrake profile necessary to achieve it. The true strength of the onboard trajectory generator lies in its ability to handle off-nominal drop conditions, when canned trajectory references may be inadequate. A series of test cases highlighted the ability of the autonomous algorithms to effectively cope with anomalous initial drop conditions, reach the ALI at the desired

states, and provide as much late-trajectory robustness as possible. In addition, the inherent ability of the algorithms to perform mission planning sensitivity studies was introduced.

Complete, flyable, optimized trajectory outputs with the necessary guidance states were typically generated in roughly 60 seconds on a 300 MHz Pentium II computer. While this performance constitutes an incredible advance over the typical week/month trajectory design timeframe of a human engineer, it merits a rating of rapid, rather than truly real-time. The use of a compiled language, like C++, rather than an interpreted language like MATLAB, should bring about another major decrease in computation time. Efficient coding in flight software optimized for quickness of execution would almost surely bring the onboard guidance a real-time classification.

## **8.2 Recommendations for Further Research**

The methods used by the autonomous algorithms for constructing guidance trajectories hold great promise for implementation aboard a RLV like the X-34. This thesis offers a starting point from which further development of its original concepts may proceed. The thrust of likely future efforts will fall into three categories: improving, extending, and demonstrating the capabilities of the onboard trajectory generation.

The autonomous algorithms can benefit from a number of improvements. The lateral channel should be upgraded to allow landing approaches from either side of the runway centerline. This will expand algorithm coverage from a wider array of starting conditions. A method to calculate estimates of max dive and glide limits based on current energy and location information will increase capability. Switching to the use of polynomial functions for aerodynamic calculations instead of the current table lookup arrangement may alleviate program incompatibilities with atypical alpha conditions. In addition, greater emphasis on graceful program termination and restart in the presence of failures will be required for eventual flight software.



A number of extensions will help capitalize on the inherent capability of onboard trajectory generation. First, the inclusion of wind disturbances into the flight dynamics model will allow the capability to design robust trajectories utilizing timely telemetered weather data of downstream conditions. Second, modifications allowing higher initial condition speeds and altitudes may carry the benefits of the approach to supersonic TAEM. The lateral channel could also be used as a deliberate energy controller, allowing greater capability for high energy conditions. These extensions will allow a meaningful exploration of the vehicle performance envelope over varying positions, headings, and atmospheric conditions.

A demonstration of onboard trajectory generation in concert with the other components of next generation entry guidance will showcase the holistic improvements of the novel approach in ways that have a significant impact on its technology adoption by the aerospace industry. Linking the onboard trajectory generation to an abort planner will allow a truly intact abort capability for the first time. Cooperation with an integrated flight controller will maximize the benefit of the new approach. Finally, transformation of the integrated algorithms to flight software on a flight demonstration of the X-34 will herald the beginning of a new era in entry guidance.



# Appendix A

## Examples Highlighting Different AI Capability Levels

Table A.1: AI Capability Level Examples

Capability	Examples		
	Assembly-line Robot Arm	Human Pilot	Entry Guidance
<b>Automatic</b>	Robot arm transfers bolt from tray to moving conveyor belt without human operator intervention.	Nominal flight plan followed. No help requested from supervisor.	Vehicle follows its loaded reference trajectory and minimizes small errors by using its control system.
<b>Autonomous</b>	An earthquake rocks the assembly plant, moving the conveyor belt 6 inches away from its previous position. The robot arm, sensing the altered location, adjusts its movements accordingly.	Engine#2 fails. The pilot follows learned procedures to shut down the faulty engine, activate fire suppression, and retrim the aircraft to operate on the remaining engine.	In a drop test, the vehicle is accidentally dropped earlier than planned, invalidating any loaded trajectory reference. It responds by redesigning a new, appropriate reference trajectory.
<b>Intelligent</b>	Just before closing time, thunderstorms outside the plant threaten to disrupt the continuous power supply needed for operation. Anticipating a power outage, the robot arm increases its speed in an effort to complete its task earlier.	Faced with the loss of a rudder, a pilot uses differential thrust to bring the airplane to a safe landing even though no training ever covered this technique.	Realizing that the vehicle is slightly below the minimum energy needed to reach the only available runway, onboard guidance makes a small course correction to take advantage of the strong thermal updrafts predicted above an upcoming canyon.



## Appendix B

### Method for Calculating Maximum $R_{AC}$

Figure B.1 provides a simplified description of the procedure to calculate the lateral geometric limit. Figure B.2 shows the result for an example case.

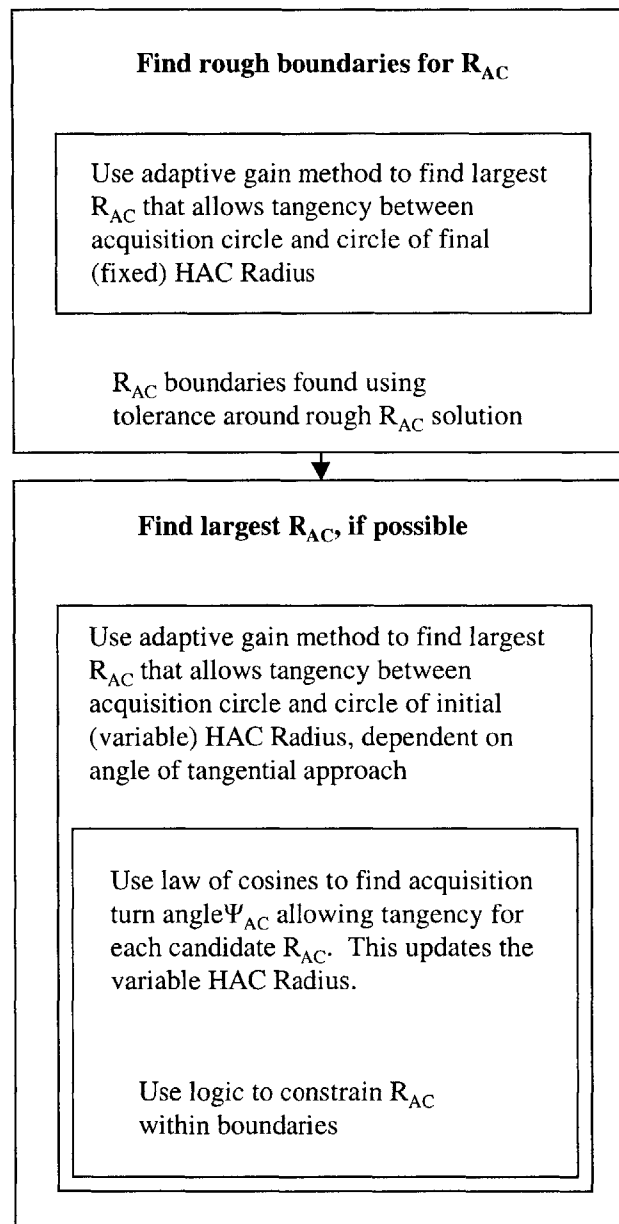


**Figure B.1:** Simplified Procedure to Calculate Lateral Geometric Limit

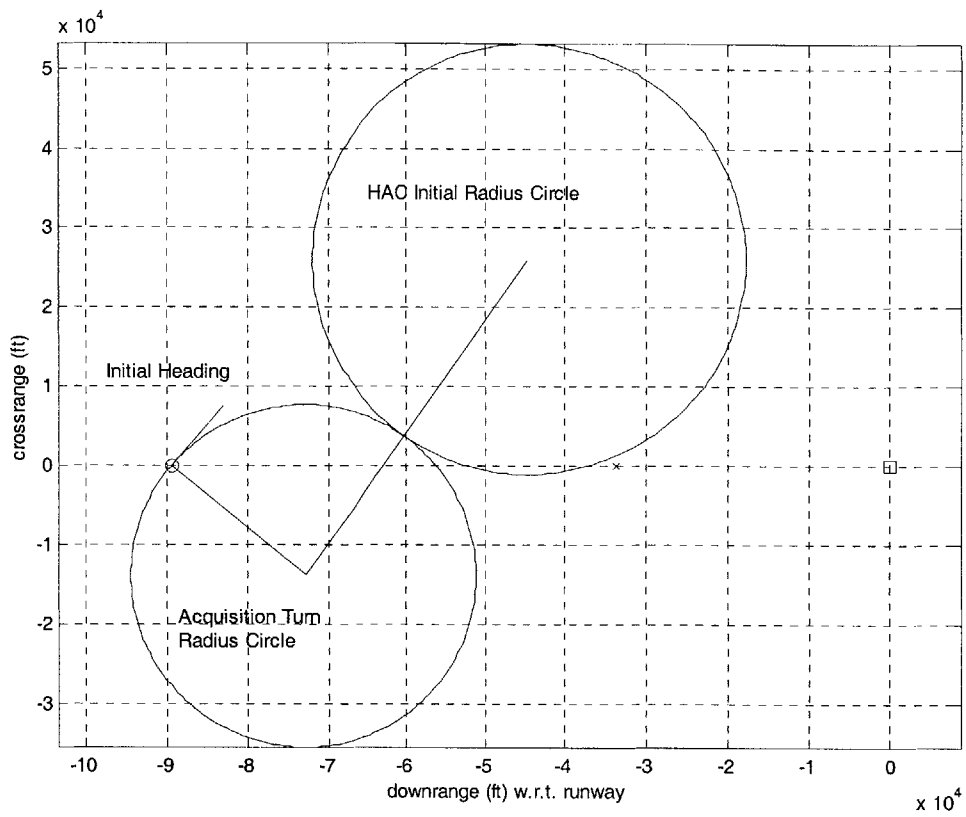


**Figure B.2:** Geometric Limit (Max  $R_{AC}$ ) Result for Example Case

## Appendix C

### Example of Effect of Bank Angle on Maximum and Minimum $dq/dt$

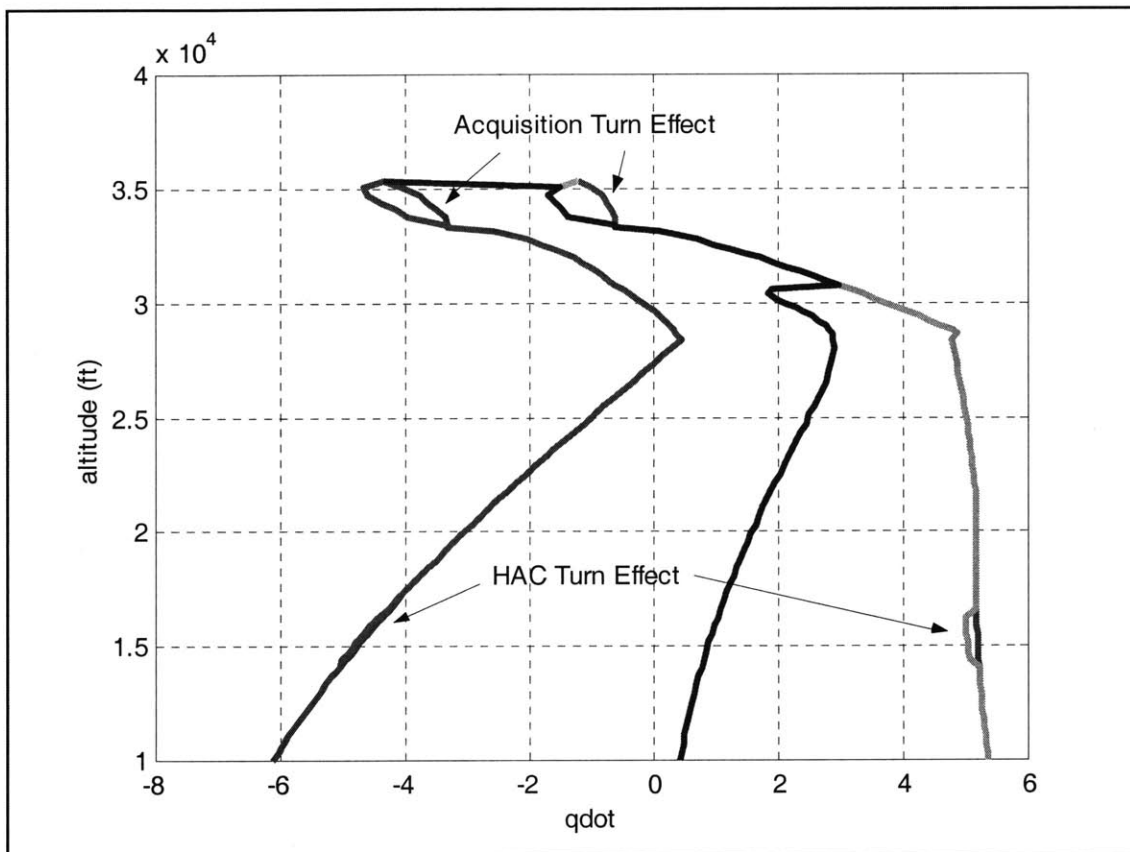
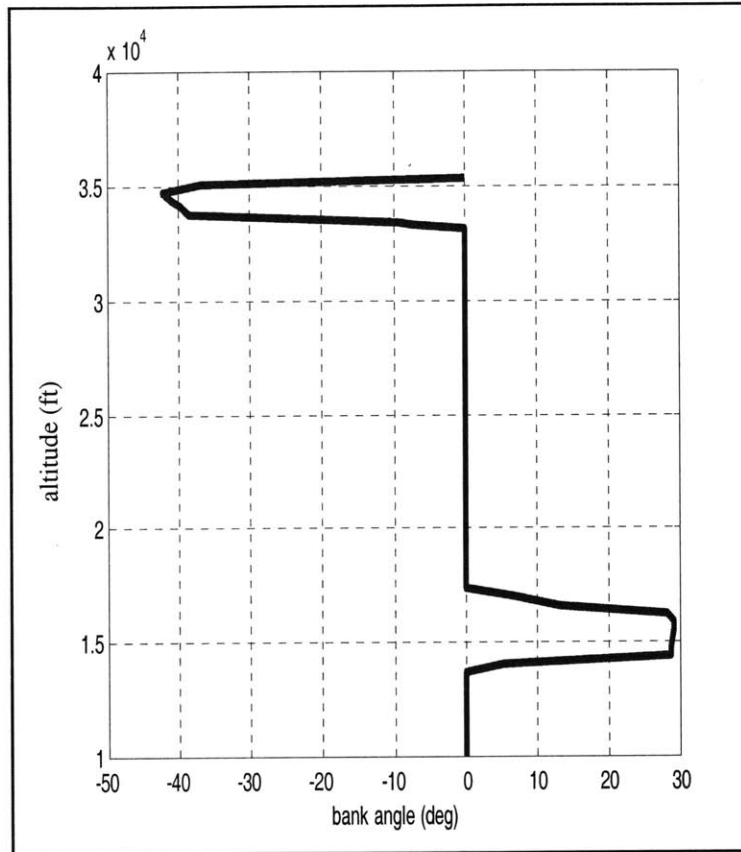
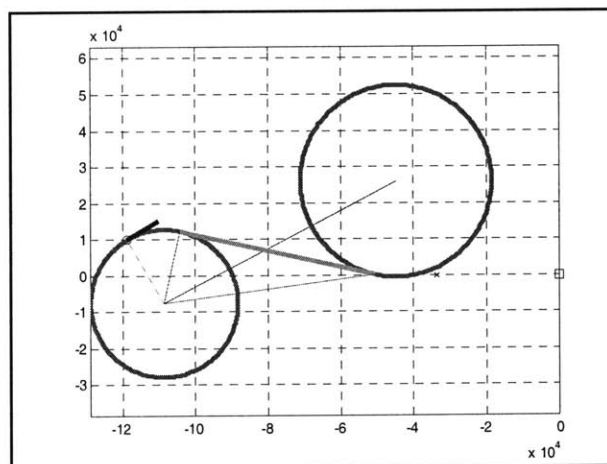


Figure C.1: Effect of Bank Angle on Maximum and Minimum  $dq/dt$



**Figure C.2:** Bank Angle Profile for Figure C.1



**Figure C.3:** Lateral Geometry for Figure C.1



# Appendix D

## Additional Onboard Results From DRM4 Drop Scenario

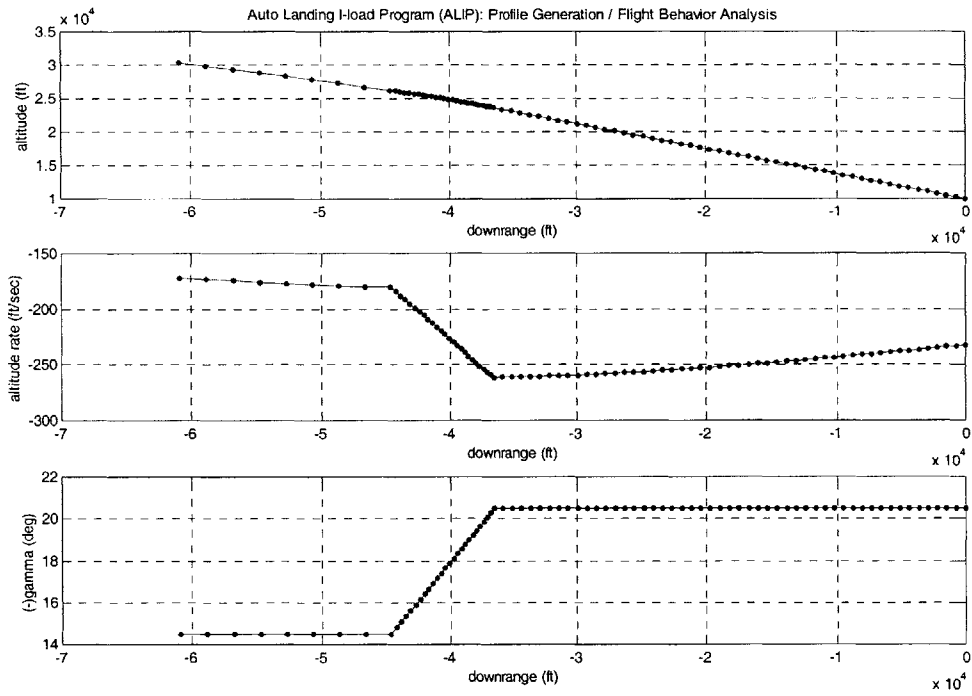
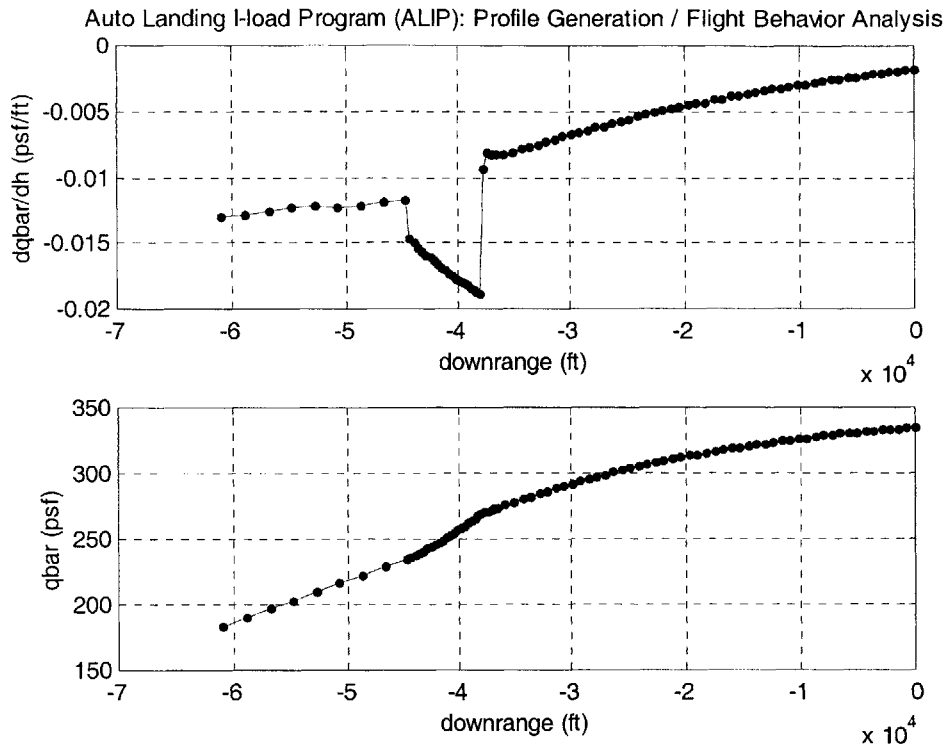
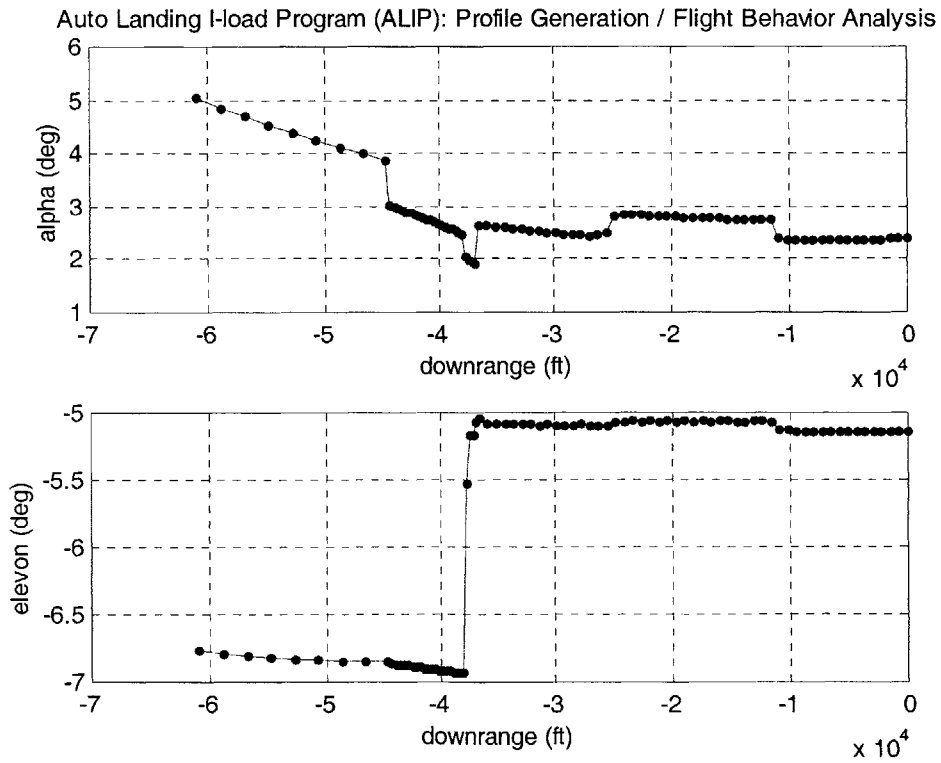


Figure D.1: Gamma, Altitude Rate and Altitude vs. Downrange



**Figure D.2:** Qbar and Dqbar/dh vs Downrange



**Figure D.3:** Elevon and Alpha Positions vs Downrange

Auto Landing I-load Program (ALIP): Profile Generation / Flight Behavior Analysis

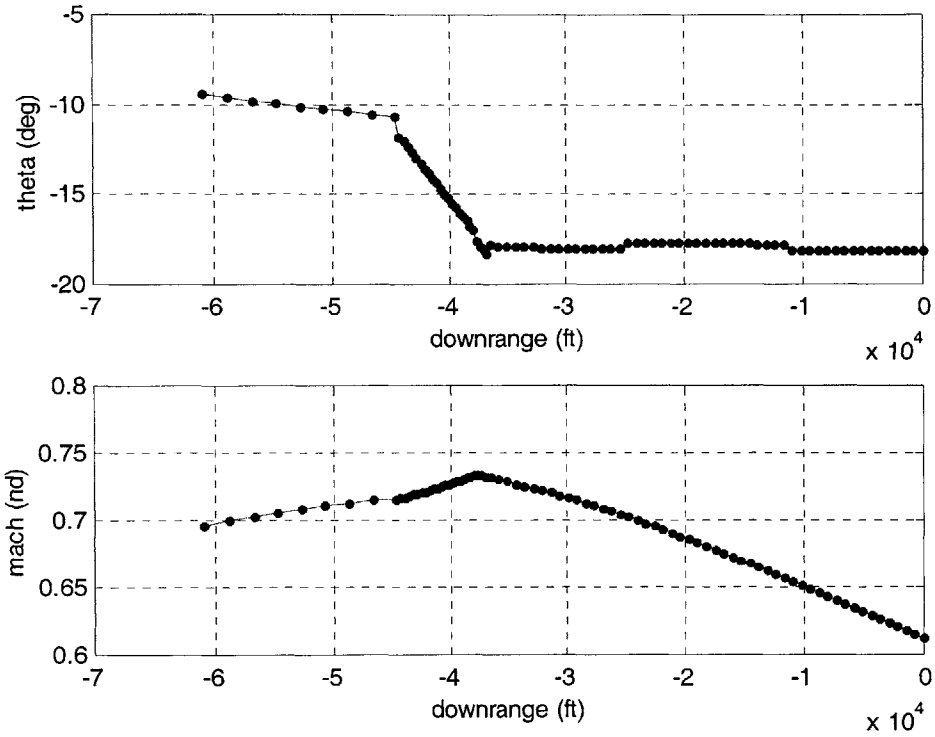


**Figure D.4:** Mach Number and Theta vs. Downrange

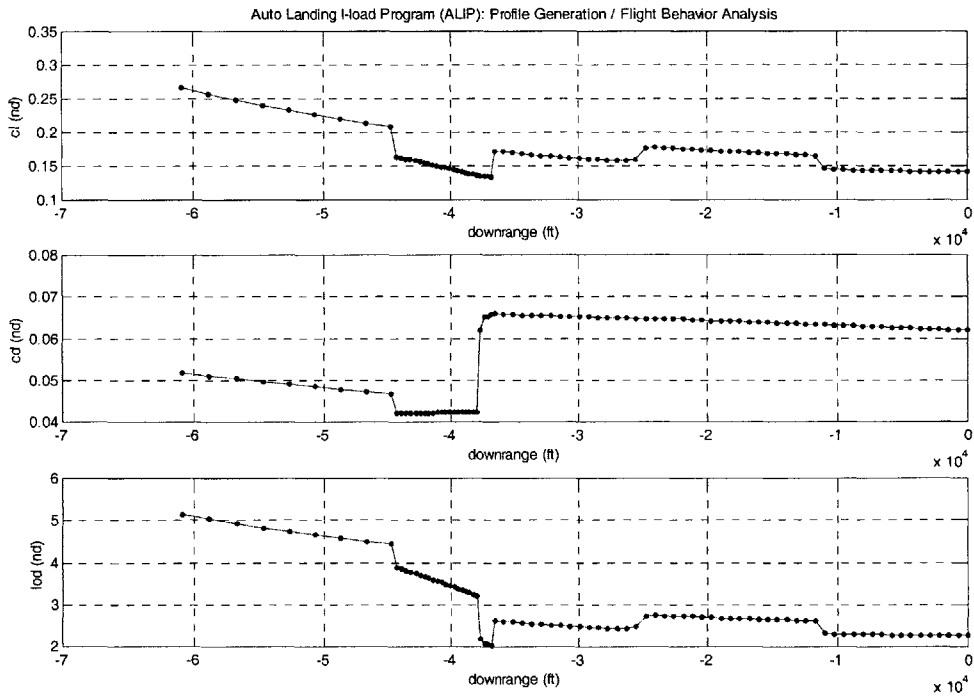


**Figure D.5:**  $L/D$ ,  $C_D$ , and  $C_L$  vs. Downrange

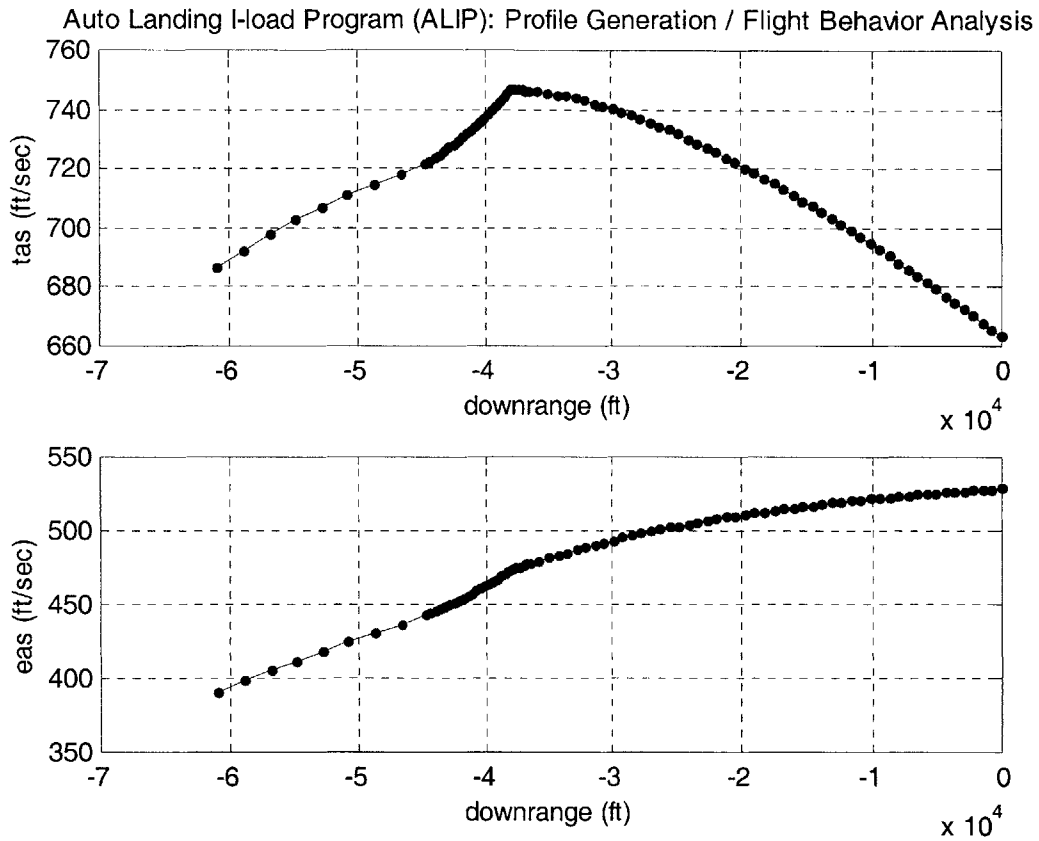


**Figure D.6:** Equivalent Airspeed and True Airspeed vs. Downrange

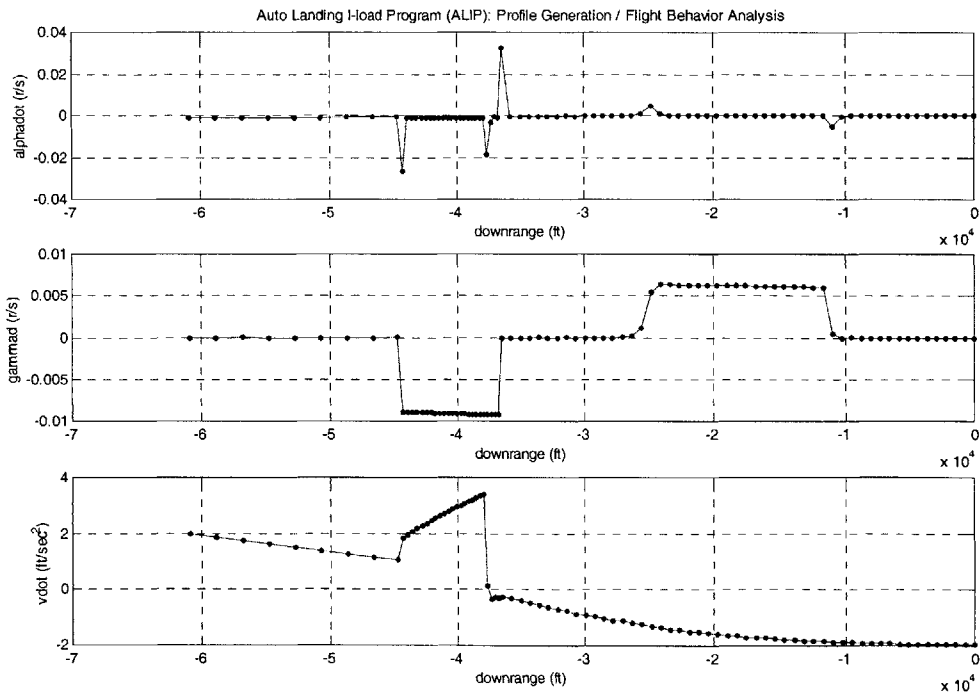


**Figure D.7:** Vdot, Gammadot, and Alphasdot vs. Downrange

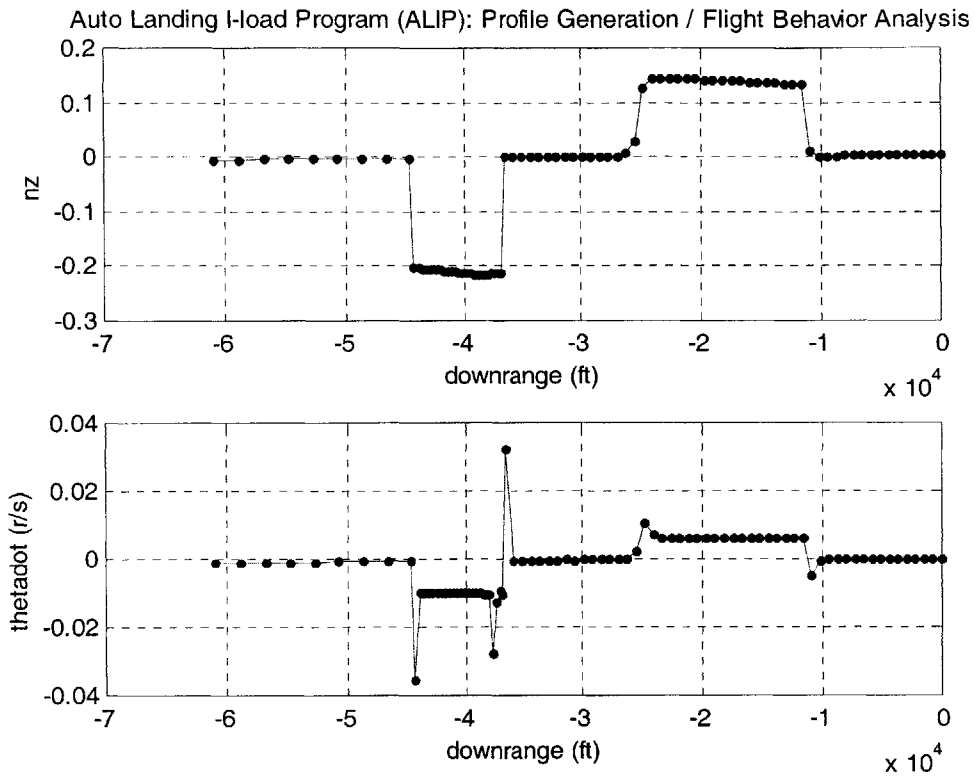


**Figure D.8:** Thetadot and NZ vs. Downrange

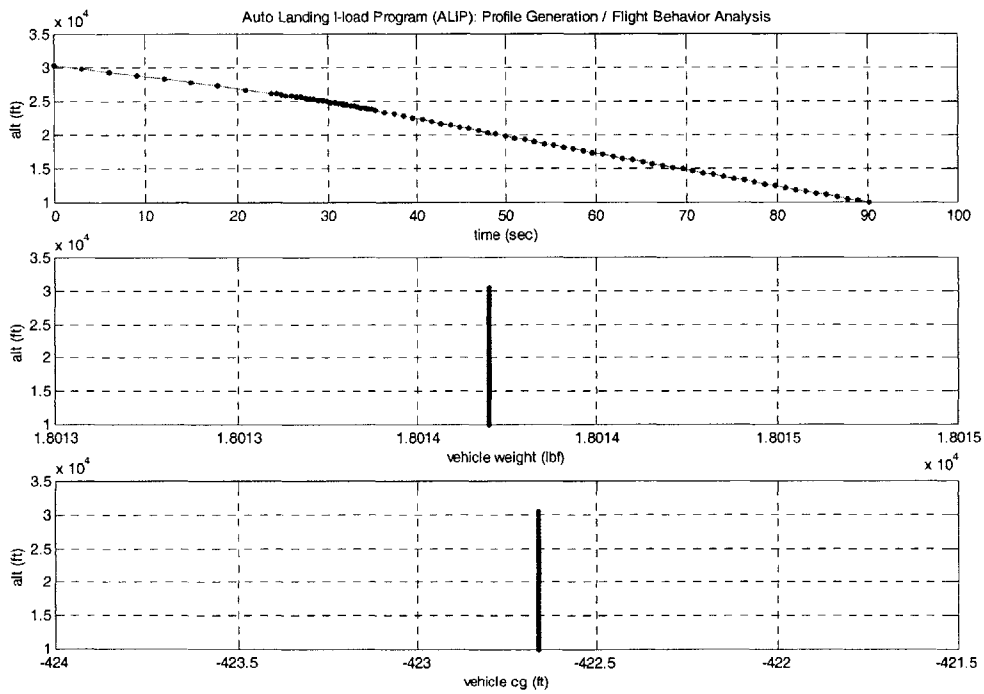


**Figure D.9:** Altitude vs. Time, Vehicle Weight, and Vehicle CG

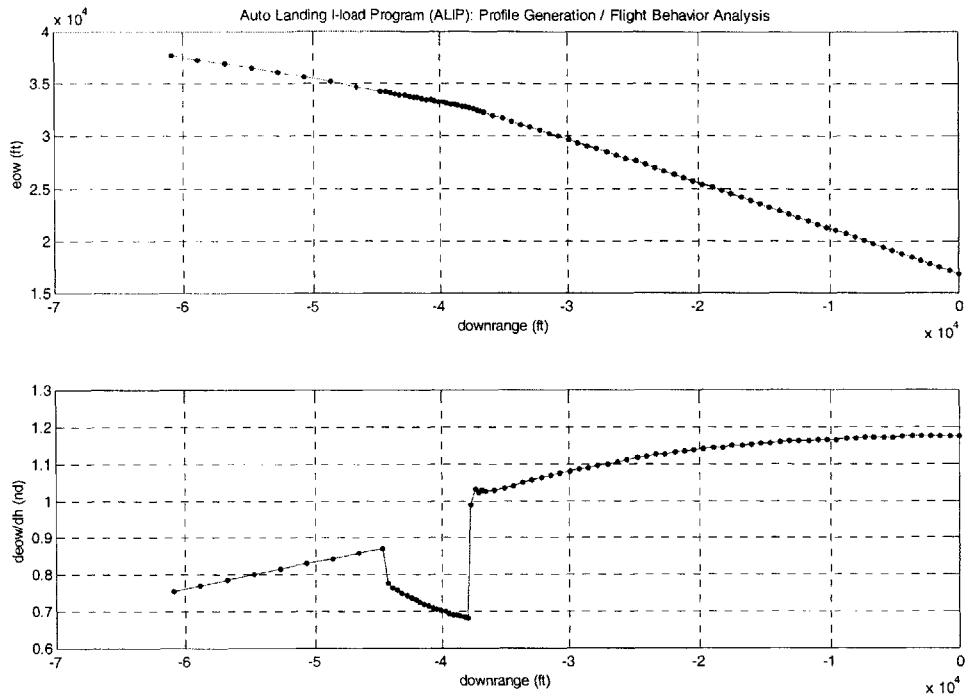


**Figure D.10: Energy Over Weight and Deow/dh vs. Downrange**

## References

- [1] Ishimoto, S., "Guidance Algorithm for Suborbital Flight Experiment of Unmanned Lifting Entry Vehicle," Proceedings of the AIAA Guidance, Navigation, and Control Conference, Baltimore, MD, Aug. 7-10, 1995.
- [2] Dukeman, G., and Gallaher, M., "Guidance and Control Concepts for the X-33 Technology Demonstrator," AAS Paper 98-026, 1998.
- [3] Nguyen, V. et al, "X-40A Guidance and Control & Flight Test Results", AAS Paper 99-015, 1999.
- [4] Scott, W., "X-37 Explores Entry Risks," Aviation Week and Space Technology, August 9, 1999.
- [5] Lu, P., "Entry Guidance and Trajectory Control for Reusable Launch Vehicle," *Journal of Guidance, Control, and Dynamics*. Vol. 20, No. 1, Jan.-Feb. 1997.
- [6] James, J., "Entry Guidance Training Manual," NASA Johnson Space Center, Flight Training Branch, Houston, TX, July 1988.
- [7] Barchers, J., *Entry Guidance for Abort Scenarios*, S.M. Thesis, Department of Aeronautics and Astronautics, MIT, Jun. 1997.
- [8] Chomel, C., *Design of a Robust Integrated Guidance and Control Algorithm for the Landing of an Autonomous Reusable Launch Vehicle*, S.M. Thesis, Department of Aeronautics and Astronautics, MIT, Jun. 1998.
- [9] Tracy, C., *Integrated Guidance and Control for Autonomous Reusable Launch Vehicles*, S.M. Thesis, Department of Aeronautics and Astronautics, MIT, Sept. 1999.
- [10] Tragesser, S., and Barton, G., "Autonomous Intact Abort System for the X-34," AIAA Paper 99-4253, 1999.
- [11] Barton, G., and Tragesser, S., "Autolanding Trajectory Design for the X-34," AIAA Paper 99-4161, 1999.
- [12] Osowski, T., Rovner, D., and Ruth, M., *STEP*, Visual C++ program written at Orbital Sciences Corporation, Feb. 1998.
- [13] Marshal Space Flight Center Fact Sheet "X-34: Demonstrating Reusable Launch Vehicle Technologies," <http://www1.msfc.nasa.gov/NEWSROOM/background/facts/x-34.htm>, Aug. 10, 2000.

- [14] Moore, T., "Space Shuttle Entry Terminal Area Energy Management," NASA Johnson Space Center, NASA Technical Memorandum 104744, Nov. 1991.
- [15] Program to Optimize Simulated Trajectories (POST), <http://www.johnsonrockets.com/rocketweb/post3d.html>, Jan. 11, 2001.
- [16] MATLAB<sup>®</sup> 5.3.1.29215a (R11.1), The MathWorks, Inc., Sept. 28, 1999.

2916-1